



HAL
open science

Pressure-induced disorder in bulk and nanometric SnO₂

Helainne Thomeny Girao

► **To cite this version:**

Helainne Thomeny Girao. Pressure-induced disorder in bulk and nanometric SnO₂. Material chemistry. Université de Lyon, 2018. English. NNT : 2018LYSE1176 . tel-02001972

HAL Id: tel-02001972

<https://theses.hal.science/tel-02001972>

Submitted on 31 Jan 2019

HAL is a multi-disciplinary open access archive for the deposit and dissemination of scientific research documents, whether they are published or not. The documents may come from teaching and research institutions in France or abroad, or from public or private research centers.

L'archive ouverte pluridisciplinaire **HAL**, est destinée au dépôt et à la diffusion de documents scientifiques de niveau recherche, publiés ou non, émanant des établissements d'enseignement et de recherche français ou étrangers, des laboratoires publics ou privés.



N° d'ordre NNT: 2018LYSE1176

THÈSE de DOCTORAT DE L'UNIVERSITÉ DE LYON

Opérée au sein de

L'Université Claude Bernard Lyon 1

École Doctorale de Physique et Astrophysique (EDPHAST52)

Spécialité de doctorat : Physique

Discipline : Physique des Matériaux

Soutenue publiquement le 24/09/2018, par :

Helaine THOMENY GIRÃO

Pressure-induced disorder in bulk and nanometric SnO₂

Devant le jury composé de :

Nom, prénom grade/qualité établissement/entreprise Président.e (à préciser après la soutenance)

PAILLARD Vincent – Professeur – Université de Toulouse – Rapporteur

ROUQUETTE Jérôme – Chargé de Recherche HDR, CNRS – Université de Montpellier – Rapporteur

GOGLIO Graziella – Professeur – Université de Bordeaux – Examinatrice

KAHN Myrtil, Directrice de recherche, CNRS - Laboratoire de Chimie de Coordination, CNRS – Toulouse – Examinatrice

PISCHEDDA Vittoria – Maître de Conférences HDR – Université Claude Bernard Lyon1 – Examinatrice

MELINON Patrice – Directeur de Recherche, CNRS – Université Claude Bernard Lyon1 – Directeur de thèse

MACHON Denis – Maître de Conférences HDR – Université Claude Bernard Lyon1 – Co-directeur de thèse

UNIVERSITE CLAUDE BERNARD - LYON 1

Président de l'Université

Président du Conseil Académique

Vice-président du Conseil d'Administration

Vice-président du Conseil Formation et Vie Universitaire

Vice-président de la Commission Recherche

Directrice Générale des Services

M. le Professeur Frédéric FLEURY

M. le Professeur Hamda BEN HADID

M. le Professeur Didier REVEL

M. le Professeur Philippe CHEVALIER

M. Fabrice VALLÉE

Mme Dominique MARCHAND

COMPOSANTES SANTE

Faculté de Médecine Lyon Est – Claude Bernard

Faculté de Médecine et de Maïeutique Lyon Sud – Charles Mérieux

Faculté d'Odontologie

Institut des Sciences Pharmaceutiques et Biologiques

Institut des Sciences et Techniques de la Réadaptation

Département de formation et Centre de Recherche en Biologie Humaine

Directeur : M. le Professeur G.RODE

Directeur : Mme la Professeure C. BURILLON

Directeur : M. le Professeur D. BOURGEOIS

Directeur : Mme la Professeure C. VINCIGUERRA

Directeur : M. X. PERROT

Directeur : Mme la Professeure A-M. SCHOTT

COMPOSANTES ET DÉPARTEMENTS DE SCIENCES ET TECHNOLOGIE

Faculté des Sciences et Technologies

Département Biologie

Département Chimie Biochimie

Département GEP

Département Informatique

Département Mathématiques

Département Mécanique

Département Physique

UFR Sciences et Techniques des Activités Physiques et Sportives

Observatoire des Sciences de l'Univers de Lyon

Polytech Lyon

Ecole Supérieure de Chimie Physique Electronique

Institut Universitaire de Technologie de Lyon 1

Ecole Supérieure du Professorat et de l'Education

Institut de Science Financière et d'Assurances

Directeur : M. F. DE MARCHI

Directeur : M. le Professeur F. THEVENARD

Directeur : Mme C. FELIX

Directeur : M. Hassan HAMMOURI

Directeur : M. le Professeur S. AKKOUCHE

Directeur : M. le Professeur G. TOMANOV

Directeur : M. le Professeur H. BEN HADID

Directeur : M. le Professeur J-C PLENET

Directeur : M. Y.VANPOULLE

Directeur : M. B. GUIDERDONI

Directeur : M. le Professeur E.PERRIN

Directeur : M. G. PIGNAULT

Directeur : M. le Professeur C. VITON

Directeur : M. le Professeur A. MOUGNIOTTE

Directeur : M. N. LEBOISNE

Title: Pressure-induced disorder in bulk and nanometric SnO₂

Abstract

Nanosized materials have been the focus of an extensive interest research as they present new physical and chemical properties in comparison to their bulk equivalent. When dealing with nanomaterials, the size effect and the surface energy are generally invoked, even though the underlying concepts are not clear. In this thesis, the main question that we want to answer is: what are the main parameters which govern the structural stability at the SnO₂ nanometric under high-pressure in comparison to its bulk counterpart? The combination of high-pressure and particle size is particularly important in order to understand the nanoparticle structure, and the effect of the defects and of the surface energy on phase stability. By maintaining the size of the particle constant, the pressure will allow the energy landscapes of the system to be explored. In addition, pressure and size are two parameters that can be used conjointly in order to stabilize new phases. So, the interest of studying nanoparticles under the high-pressure is at least two-fold: (i) to gain a fundamental understanding of thermodynamics when the interfacial energy reaches the same magnitude as the internal energy, and (ii) to stabilize new structures that may have potential interest as functional materials. In this work, we used Raman spectroscopy as the main characterization method. In the study of SnO₂ bulk samples, we used percolation to explain the “partial” disorder of the oxygen sublattice which appears in the powders when the pressure increases; and for studying SnO₂ nanoparticles, we used *ab initio* simulations to explain the appearance of this kind of disorder, *i.e.* the anionic sublattice disorder in SnO₂ nanoparticle samples. In this way, we propose to obtain a fundamental understanding about the properties of SnO₂ bulk and nanoparticles under pressure.

Keywords:

SnO₂, Nanoparticles, bulks, defects, high-pressure, Raman spectroscopy, phase transition, pressure-induced amorphization (PIA), partial amorphization.

Titre : Désordre induit par la pression dans le SnO₂ massif et nanométrique.

Résumé

Les matériaux nanométriques ont fait l'objet d'un intérêt de recherche important, car ils présentent de nouvelles propriétés physiques et chimiques par rapport aux échantillons massifs. En ce qui concerne les nanomatériaux, l'effet de taille et l'énergie de surface sont généralement invoqués, même si les concepts sous-jacents ne sont pas clairs. Dans cette thèse, la question principale à laquelle nous voulons répondre est : quels sont les principaux paramètres qui régissent la stabilité structurelle du SnO₂ à l'échelle nanométrique sous haute pression comparée aux échantillons de SnO₂ massifs ? La combinaison de la haute pression et de la taille des particules est particulièrement importante pour comprendre la structure de ces nanoparticules et l'effet des défauts et de l'énergie de surface sur leur stabilité de phase, car, en gardant la taille des particules constante, l'augmentation de la pression permettra l'exploration des paysages énergétiques du système. De plus, la pression et la taille sont deux paramètres qui peuvent être utilisés conjointement pour stabiliser les nouvelles phases. L'intérêt de l'étude des nanoparticules sous haute pression est au moins double : (i) acquérir une compréhension fondamentale de la thermodynamique lorsque l'énergie interfaciale devient de la même ampleur que l'énergie interne, et (ii) pour stabiliser de nouvelles structures potentiellement intéressantes en tant que matériaux fonctionnels. Dans ce travail, nous avons utilisé la spectroscopie Raman comme principale méthode de caractérisation. Pour les échantillons de SnO₂ massif, nous avons utilisé la théorie de la percolation pour expliquer le désordre « partiel » du sous-réseau oxygène qu'apparaît lorsque la pression augmente, ce qu'on appelle désordre « partiel » induit par la pression. Et, en étudiant les nanoparticules de SnO₂, nous avons utilisé des simulations *ab initio* pour expliquer l'apparition de ce type de désordre, c'est-à-dire, le désordre du sous-réseau anionique lorsque la pression augmente. De cette façon, nous proposons d'obtenir une compréhension fondamentale des propriétés du SnO₂ massif et nanométrique, sous pression.

Keywords :

SnO₂, nanoparticules, bulks, défauts, haute pression, spectroscopie Raman, transition de phase, amorphisation induite par pression (PIA), amorphisation partielle.

Remerciements

Tout d'abord, je tiens à remercier mes directeurs de thèse Patrice MELINON et Denis MACHON. Sans eux, ce serait impossible de faire cette thèse à l'Institut Lumière Matière et de, surtout, la finir. Merci pour l'accueil, merci pour le soutien, merci de m'avoir supporté (surtout pendant mes crises d'anxiété et d'angoisse). Merci pour tout cela et un peu plus, merci, vous avez joué un rôle fondamental dans ma réussite.

Je remercie également tous les membres du jury d'avoir accepté cette mission, principalement pendant les vacances. Leurs remarques m'ont été super précieuses.

Merci à tous les personnels administratifs: Delphine KERVILLA, Christelle MACHEBOEUF, Françoise CHAMPION, Anne-Marie JURDYC, Sylvie FLORES.

Merci aussi à tous les membres de l'ILM (ou pas) qui m'ont aidé (implicitement ou explicitement) à réussir. En spécial, je remercie Gilles MONTAGNAC et Gérard PANCZER d'avoir fourni quelques morceaux de monocristaux de SnO₂. Stéphane DANIELE de l'IRCELyon pour avoir produit mes nanoparticules et Shashank MISHRA pour m'avoir aidé avec les schémas et pour les échanges hors Université. Ruben VERA, Erwann JEANNEAU et Régis DEBORD, merci pour les mesures de diffraction des rayons X. Je remercie aussi Bruno MASENELLI pour les résultats de photoluminescence, Thibaut CORNIER pour les micrographies de TEM et Sylvie LE FLOCH pour m'aider avec les mesures à l'infrarouge. Je remercie également Patrick HERMET de l'Université de Montpellier pour les simulations *ab-initio* du SnO₂ massif, ainsi comme Ricardo A. CASALI (*in memoriam*) et Maria A. CARAVACA, de l'Universidad Nacional del Nordeste, en Argentina, pour les simulations *ab-initio* du SnO₂ nanométrique.

Je remercie, le « Conselho Nacional de Pesquisa e Desenvolvimento – CNPq » du Brésil pour m'avoir fait confiance et d'avoir financé ces quatre ans d'études.

Je remercie les amis et la famille. Je pourrai m'arrêter là, mais il y a des gens spéciaux qui méritent être mentionnés, un par un.

Je commence par mes copains bureau : Jhiming SHI, Alexia BARBOSA DE LIMA et Shelby TURNER, merci pour les bons moments de « papotage ». Parmi eux, il y a une personne très spéciale, qui m'a beaucoup aidé avec les corrections et de plus, on a développé une amitié que j'espère que ce soit pour toujours. Shelby, je sais que je t'ai déjà remercié plusieurs fois, mais ne sera jamais suffisant. Encore une fois : ma chère Shelby, merci infiniment.

Maintenant, c'est le tour de mes chers amis brésiliens : Thais VIDAL, Tulio CHAVES, Izabel et Edwyn COSTA, Cinthia PETITO. Mes amis, merci pour tous les moments de partage, « papotage », conseils. Merci pour ceci, pour cela, pour tout. Merci à vous tous, vous étiez LA pièce du puzzle.

Merci aussi aux amis français, les cousines Valérie GATTO et Chantal GATTO, ma chère Claire PAQUOT. Merci pour le soutien, les sorties et les bons moments de partage.

Pierre-Yves VAILLY, mon cher kiné. Je ne pourrai jamais oublier de te remercier. Toutes les semaines tu m'as aidé à mieux supporter mes douleurs. Les moments dans le cabinet étaient toujours de joie. Un gros bisou à tous du cabinet et encore merci.

Je remercie également Jacqueline CIAMPI, avec qui je pu partager deux ans de mon séjour en France. Merci Jacqueline pour nos joyeuses dix heures par semaine et pour tous les mots d'encouragement.

Je pense que remercier la famille c'est la partie la plus difficile. Ce sont eux qui ont supporté toutes mes crises, mes angoisses, l'anxiété, les conséquences des nuits blanches. D'abord, je remercie mes enfants : Sarinha, mon cœur, merci pour ta compréhension, pour ton aide, pour ton amour ; Arthur, je m'excuse parce que j'étais distante, absente. Mes enfants, je suis désolée pour les mauvais moments. David, mon amour, je pense que te remercier, cela est le travail le plus dur. Toi qui étais réveillé chaque nuit que j'y étais, toi qui m'as aidé, soutenu. Je n'aurais jamais des mots suffisants pour remercier toute l'aide qui tu m'as donné. Merci de m'avoir fait confiance, pour croire que j'étais capable même quand moi-même, je n'en croyais plus. Merci, ma petite famille, mes amours, je vous aime.

Mãe (maman), merci d'être venue m'aider avec les enfants et après, d'être revenue pour ma soutenance. Pai (papa), merci d'être là pour un jour si important. Merci à vos deux qui, même avec toutes les contraintes, ont pu être ici pour me soutenir, pour que je puisse partager ce moment si important avec vous. Je remercie également mes trois sœurs : Priscila, Karen, Karine, qui, même de loin, m'ont soutenu avec des mots, des conseils. En spécial, je remercie à Priscila, parce qu'elle a pu participer à ma soutenance.

Raimundinha, ma chère belle-mère, merci d'être venue encore une fois, principalement pendant ce moment crucial. Tu n'as pas l'idée de comme ta présence était fondamentale pour que je puisse arriver jusqu'au bout. Merci pour toute l'aide qui tu m'as donné. Je remercie également mes belles-soeurs Klarissa et Kamilla. En spécial, Kamilla, merci de prendre le relais de D. Raimundinha pour qu'elle puisse être là.

Enfin, je tiens à remercier à tous ceux qui étaient acteurs du film que s'appelle : « *Elle a réussi, et moi, j'ai fait partie de son succès* ». Encore une fois : **Merci à tous.**

À mes raisons de vivre, Sara et Arthur.

À mon amour pour toujours, David.

À mes parents, avec beaucoup d'amour.

To my reasons for living: Sara and Arthur.

To my love forever, David.

To my parents, with a lot of love.

Table of Contents

Abstract	iii
Résumé	iv
Remerciements	v
Table of Contents	viii
Table of Figures	ix
Introduction	1
Chapter 1	7
1.1. Synthesis method	8
1.1.1.Sol-gel technique: a chemical route	8
1.2. The defects on the crystals	9
1.2.1.The types of defects in crystalline solids	10
<i>a) Point defects</i>	11
<i>b) Linear defects</i>	14
<i>c) Interfacial or surface defects</i>	15
<i>d) Volume defects</i>	16
1.2.2.The SnO ₂ case.....	17
1.2.3.The impacts of these defects on the SnO ₂ Raman spectra	18
1.3. Pressure generator system	20
1.3.1.The Diamond Anvil Cell (DAC).....	20
1.3.2.Pressure Transmitting Medium – PTM and the conditions for compression	24
1.4. Characterization Techniques	26
1.4.1. X-ray Diffraction (XRD).....	26
1.4.2.Spectroscopy Techniques.....	29
<i>a) Raman Spectroscopy</i>	29
<i>b) Photoluminescence (PL) Spectroscopy</i>	35
Chapter 2	36
2.1. SnO₂ general information	37
2.2. SnO₂ bulk behavior under pressure from literature	39
2.3. SnO₂ nanoparticles	49
2.4. SnO₂ nanometric under pressure from the literature	56
Chapter 3	62
3.1. Introduction	63
3.2. The characterization methods	64

3.2.1.The characterization at ambient pressure	64
a) <i>X-ray Diffraction (XRD)</i>	64
b) <i>Photoluminescence (PL) Spectroscopy</i>	67
c) <i>Raman spectroscopy</i>	69
3.2.2.Characterization at high-pressure	71
a) <i>Raman Spectroscopy</i>	71
b) <i>First-principles calculations</i>	81
3.3. Discussion	84
Chapter 4	90
4.1. Synthesis and characterization methods	91
4.1.1.The Synthesis	91
4.1.2.The characterization at ambient pressure	93
a) <i>Transmission electron microscopy (TEM)</i>	93
b) <i>X-ray Diffraction (XRD)</i>	95
c) <i>Raman spectroscopy</i>	96
4.1.3.The characterization at the high-pressure	99
a) <i>X-ray diffraction</i>	99
b) <i>Raman Spectroscopy</i>	100
c) <i>The ab-initio Simulations</i>	109
4.2. Discussion	110
General Conclusion	115
Perspectives	118
Appendix	119
A.1. Physical principles of Raman spectroscopy	120
A.2. Lamb explanation for the origin of low-frequency vibrations	122
A.3. Published works	125
Bibliography	126

Table of Figures

Figure 1 – Representation of the pressure-induced disorder in a multidimensional plot. The axis “Parameter X” considers the nature and the density of the defects. Adapted from ref.23.	4
Figure 2 – Classification of the different types of defects that can be found in a crystal. Adapted from ⁵⁸	10
Figure 3 - Examples of simple point defects. (a) Vacancy. (b) Self-interstitial atom. (c) A Schottky defect (absence of ions on normally occupied sites; for charge neutrality there must be equal numbers of cation and anion vacancies in a 1:1 compound). (d) A Frenkel defect (it forms when an ion moves to an interstitial site). (e) Substitutional impurity atom (f) Interstitial impurity atom. Adapted from refs. 61,63.....	13
Figure 4 – Dislocations: (a) Edge type. (b) Screw type. Adapted from ref. ⁶⁰	14
Figure 5 – (a) Schematic representation of the arrangement of atoms at a grain boundary in a polycrystalline sample. The grain boundary, an area between two adjacent crystallites, is a defect that corresponds to both a crystalline orientation discontinuity and a zone in which the relative positions of the atoms do not correspond to the equilibrium positions minimizing the 'interaction. (b) Schematic diagram showing small and high-angle grain boundaries and the adjacent atom positions. (c) Schematic diagram showing a twin plane or boundary and the adjacent atom positions (green circles). (d) Stacking fault produced by the absence of a plane C in the sequence ... ABC ABC A ... constituting a compact cubic structure. Adapted from ⁵⁹ and ⁶¹	16
Figure 6 – The four types of semiconductor metal oxides: (a) Oxygen vacancies (n-type), (b) Interstitial metal (n-type), (c) Metal vacancies (p-type), and (d) Interstitial oxygen (type p). Adapted from ref. ⁶⁵	18
Figure 7 – Raman spectra of (a.i) SnO ₂ nanoparticles SnO ₂ , (a.ii) SnO ₂ bulk. (b) Deconvolution fitting plots of the Raman spectra from SnO ₂ . Adapted from ref. 67 .	19
Figure 8 – Carbon phase diagram. Adapted from ref. ⁶⁸	20
Figure 9 – Block diagram of the diamond anvil cell. This consists of three main parts: the piston and the cylinder which form the body of the cell, and the cover containing a metallic membrane.	21
Figure 10 – Schematic section of a diamond anvil cell (DAC) ⁷⁰	21
Figure 11 – Principle of the Diamond Anvil Cell. ⁷⁰	22
Figure 12 – a) Chervin-type DAC membrane used in the Raman spectroscopy experiments at the high-pressure	24

Figure 13 – A schematic reflection of radiation by the lattice planes according to Bragg's law. ⁷⁷	27
Figure 14 – Diagrams of Rayleigh and Raman scattering. Adapted from Ref. ⁸⁹	31
Figure 15 – Molecules scattering the light. Adapted from ref. ⁸⁹	31
Figure 16 – Raman signal information. Adapted from ref. ⁸⁹	32
Figure 17 – LabRAM HR Evolution Raman Spectrometer (Horiba Scientific) – Low frequencies ⁹⁴	34
Figure 18 – (a) Scheme of SnO ₂ unit cell of rutile-type structure: the large (red) circles indicate oxygen atoms and small (gray) circles indicate tin atoms. Adapted from ref. ²¹ . (b) Tin sublattice: tetragonal symmetry. (c) Oxygen sublattice: octahedron (cubic symmetry).....	38
Figure 19 – SnO ₂ Raman active modes. Adapted from ref. ¹¹²	39
Figure 20 – SnO ₂ pyrite-type and fluorite-type structures. Adapted from ref. ²¹	40
Figure 21 – SnO ₂ bulk behavior in the literature using XRD. Adapted from ref ¹²⁴ . ..	41
Figure 22 – (a)(Down) Raman spectrum at 14.2 GPa in the rutile-type structure. (Up) Raman spectrum at 15.6 GPa in the CaCl ₂ -type structure. (b) Pressure dependence of Raman frequencies through the rutile-to-CaCl ₂ -type transition. Legend: (x): single crystal data on increasing (decreasing) pressure; (□): powder data on increasing (decreasing) pressure. (*): soft mode frequencies from single-crystal samples, not temperature annealed. ²¹ Adapted from ref. 10	46
Figure 23 – Phonons dispersion curves and phonon density of states of SnO ₂ (a) in rutile phase at ambient pressure. (b) in rutile phase at transition pressure (12GPa).48	
Figure 24 – Raman spectra of nano-SnO ₂ , specimens heat-treated at different temperatures and of a coarse-grained specimen. ¹³⁹	51
Figure 25 – Raman spectra for five powder samples recorded at 25 °C as presented by Abello et al. The components representative of volume modes (nine bands – F to B samples and Band 10 on A sample) were defined from the single-crystal data and from spectra of a natural cassiterite sample with a large concentration of defects. ¹³⁸	52
Figure 26 – Raman spectra of the powders calcined up to 1000 °C for 8 h. The spectra have been divided into: (a) the low-frequency region and (b) the high-frequency region. The spectra in the high-frequency region correspond, from bottom to top, to the uncalcined powder and the powders calcined at 250, 330, 400, 430, 450, 800, and 1000°C for 8 h. Additional features were not observed outside these regions. ¹¹⁶	54
Figure 27 – Fitting of the bands appearing in the high-frequency region of the Raman spectrum of SnO ₂ powder of very small grain size. The bands peaking at 634, 568,	

486, and 706 cm^{-1} correspond to A_{1g} mode and bands S1, S2 and S3, respectively. Modes B_{2g} , peaking at $\sim 776 \text{ cm}^{-1}$, and E_g , peaking at 480 cm^{-1} , are also included in the fitting. ¹¹⁶	55
Figure 28 – SnO_2 nanoparticles behavior under pressure. Adapted from ref. ¹³⁷	56
Figure 29 – Room temperature synchrotron radiation energy-dispersive X-ray diffraction patterns recorded at various pressures for bulk, 14 nm, 8 nm, and 3 nm SnO_2 samples. The appearance of the peak of the cubic phase is marked with an arrow. The vertical lines in the XRD patterns for the 3 nm SnO_2 sample mark the possible positions for the peak of the cubic phase. ¹²⁷	58
Figure 30 – Schema for Garg’s study of SnO_2 nanoparticles ($\sim 5\text{nm}$) transition phase	59
Figure 31 – Bruker D8 Advance Diffractometer ¹⁶²	65
Figure 32 – Bruker D8 Advance diffractometer diagram operating in Bragg Brentano configuration. A copper anticathode produces the radiation. ¹⁶²	65
Figure 33 – X-ray diffraction patterns for (a) Merck powder sample; and (b) Aldrich powder sample. Both are indexed in the rutile-type (cassiterite) structure with no additional phase. The red bars are related to the recognition of the phases which were carried out on the data basis of PDF -4+ (ICDD).	66
Figure 34 – Normalized photoluminescence spectra of the different SnO_2 samples, excited at 266nm.	68
Figure 35 – Raman spectra of the different powders and single crystal under ambient conditions.	70
Figure 36 –Raman spectrum simulated of the rutile phase (frequencies and corresponding intensities).....	71
Figure 37 – (a)Raman spectra of SnO_2 powder (Aldrich) with increasing pressure (No pressure-transmitting medium). (b) Raman spectra of SnO_2 powder (Merck) with increasing pressure (No pressure-transmitting medium).	73
Figure 38 – Raman spectra of SnO_2 powder (Merck) with increasing pressure using a 4:1 methanol-ethanol mixture as the pressure transmitting medium PTM.	76
Figure 39 –Raman spectra of a non-oriented SnO_2 single crystal under pressure using paraffin oil as PTM.....	78
Figure 40 – Peak position as a function of the pressure.	79
Figure 41 – Comparison of the spectra at high-pressure ($P > 20 \text{ GPa}$) for each experiment.....	80

Figure 42 – Comparison of the spectra after pressure cycle for each experiment....	81
Figure 43 – (a) Comparison of the Raman spectrum of SnO ₂ powder with a calculated phonon density of states of the rutile structure at ~3.8 GPa. (b) Simulated vDOS at different pressures in rutile (red) and CaCl ₂ -type (blue) structures. The black lines follow the peak evolution under pressure	83
Figure 44 – Representation of oxygen sublattice disorder by an invasive percolation system with an increase of pressure. Adapted from ref. ¹⁸⁸	86
Figure 45 – Sol-gel synopsis to produce our SnO ₂ nanoparticles. All the rights reserved to S. MISHRA.	92
Figure 46 – Microscope JEOL 2010F FEG ¹⁹⁸	93
Figure 47 – (a) Transmission Electron Micrographs (TEM) of the as-prepared SnO ₂ sample. (b) Zoom of image (a). Excellent crystallinity may be assumed from these images.	94
Figure 48 – (Left) Oxford Xcalibur Mova Spectrometer. (Right) DAC Almax's type on a support that allows it to arrange the DAC on the four circles of the diffractometer's goniometer. ¹⁹⁹	95
Figure 49 – X-ray diffraction pattern of the as-prepared SnO ₂ sample. The peak positions and relative intensities of the rutile structure are plotted. The diffraction pattern may be indexed in this structure with usual cell parameters: a ~ 4.74 Å and c ~ 3.19 Å.	96
Figure 50 - (a) Raman spectrum of the SnO ₂ nanoparticles used in this study compared to such one of a bulk sample. Ticks show the position of the Raman peaks in a bulk sample. (b) Size distribution of the particles deduced from the low-frequency peak. 98	
Figure 51 – (a) XRD diffraction patterns with increasing pressure. The asterisk shows the diffraction signal coming from the stainless-steel gasket. (b) The relative volume as a function of pressure (points) along with a second order Birch-Murnaghan equation of state (line) using B ₀ = 252 GPa.	100
Figure 52 – (a) Pressure-induced evolution of the low-frequency range. (b) Low-frequency peak position (P1) as a function of pressure along with the calculated variation (black line) using B ₀ and B _{0'} values reported by He et al. ¹³⁶	103
Figure 53 – Raman spectra of SnO ₂ nanoparticles with increasing pressure.	104
Figure 54 – Pressure-induced evolution of the centers of the Gaussian functions used to fit the Raman spectra.	105
Figure 55 – Raman spectra upon decompression showing the reversibility of the pressure-induced transformations.	107

Figure 56 – (a) Raman spectra before and after the pressure cycle. (b) Distribution of the particle size using the low-frequency region of the Raman spectra before and after the pressure cycle.	108
Figure 57 – Snapshots obtained by ab initio simulations of a particle with a diameter of 2.8 nm (984 atoms) at different P = 0, 9 and 19 GPa.	112
Figure 58 – The internal order of the particle can be studied by means of the Radial Pair Distribution Function (g(r)), for the two-atomic species Sn and O.	113

Introduction

The context of this study

How do the oxides behave under pressure?

Metal dioxides MO_2 – where M represents the cations from groups 4 and 14 in the periodic table, such as Si, Ge, Sn, Pb, Ti, Zr, and Hf – have received special attention due to the fact that they are the main ingredients in traditional ceramics,¹ and due to their applications in several areas such as optoelectronic,² and geology studies.³ These materials also present a rich polymorphism, being the target of a great number of scientific investigations which try to understand their phase transitions under high-pressure.^{3–6} Their structural transformations are usually described in terms of changes in the polyhedral packing. In addition to the standard polymorphic phase transformation, we can also consider a phase transition from a crystalline to an amorphous phase, for example, as revealed in studies on SiO_2 and GeO_2 .^{6,7} This phenomenon was largely studied in recent years, and it was verified that several parameters were found to play a role such as defects, hydrostaticity, size, shape, and/or the form of the sample (nanoparticle, powder, or single crystal).^{8,9} Despite all of these works, the mechanism that can completely explain the total structural transformation of these oxides remains elusive. One of the usual ways to investigate the pressure-induced amorphization (PIA) and comprehend the role played by each structural parameter has been, for instance, through the study of isostructural or isochemical series of compounds.

Even after the amount of work, inclusive a special one which used optical spectroscopies (Brillouin and Raman),¹⁰ there is no sign of amorphization or disorder in SnO_2 under pressure. In this way, we will assume another perspective to understand if the reasons that SnO_2 does not show PIA (even considering that Sn belongs to the same column of the periodic table as Si and Ge) is related to atomistic or structural behavior.

Here is a very peculiar example of metal oxide...

The SnO₂ (stannic oxide or tin dioxide) has attracted a lot of attention due to its vast technological application^{11–13} (gas sensor, solid-state chemical sensors, solar cells, catalytic support materials, and as high-capacity lithium-storage), and is considered a very important oxide and semiconductor. Its properties (particle size, crystallinity, electrical, morphological, structural) are closely dependent on the synthesis route and, principally in the presence of impurities. Under ambient conditions, SnO₂ adopts the rutile-type structure in both bulk and nanopowder forms. However, due to the effect of dimensionality and the surface effect^{*},¹⁴ nanoparticles can present a lot of different physical behaviors compared to their bulk equivalent.^{15–17} Chemical (surface reactivity, catalysis, *etc.*) and physical properties will be linked to their particle size and, specifically, in a bulk crystal these properties will depend especially on the stoichiometry.¹⁸

Under pressure, the behavior of the different SnO₂ forms will be different. While in bulk, the sequence of phase transition, determined by X-ray diffraction technique,^{9,19} will be: the rutile-type undergoes to CaCl₂-type[†] at about 12 GPa, and it transforms into a PdF₂-type at about 20 GPa. As a nanopowder, it is not clear whether the CaCl₂-type is present under pressure, however, the cubic-phase will always be present.²¹

What exists in the literature related to the nanomaterials behavior under pressure?

Additionally, in nanomaterials, there exists dependency on the particle size: the smaller the size of the particle, the greater the quantum confinement and the surface effects domination. We cannot neglect the fact that particle size decreases the number of surface atoms in relation to the total number of atoms of the particle^{16,22} *i.e.* the atoms on the surface of the nanomaterials have fewer neighbors than the atoms in the bulk. Consequently, the interfacial interactions are more important at the nanoscale than at the macroscopic level, where most of the material is protected from the surface.^{16,23} In pioneer works, Tolbert *et Alivisatos*^{24–28} studied structural phase transformations in Si, CdSe, and CdS nanocrystals and they showed that since the particle size decreases the phase transition pressure will be higher. In addition, the

* When the size of a material decreases going towards nanometric scale, the proportion of atoms on the surface related to its volume cannot be neglected. While a 100 nm particle in diameter will present ~ 3% of its atoms on the surface, a grain of 10 nm will present 30% of it. Then, we can attribute this representation to the surface effect.

† Through a ferroelastic transition driven by the softening of the B_{1g} mode, which corresponds to a collective displacement of oxygen atoms.^{9,10,20}

existence of an expected $1/R$ dependence* with the transition pressure (R: particle size) was found experimentally. They explained this behavior in terms of the differences in the surface energy between the phases involved. Furthermore, they also found a similar behavior when considering the melting temperature, *i.e.* the melting point decreases with the inverse of the particle size ($T \sim 1/R$). Such results confirmed previous studies,^{24,27,29} proving that, depending on the nature of the material(s) involved, the phase stability of nanocrystals is three times higher than the bulk.

Machon *et al.*,^{30,31} using different models going from the Gibbs approach to the Landau theory of phase transition, theoretically demonstrated the dependence between the transition pressure and the particle size ($1/R$). However, such a situation is not as simple as it seems, and there are a lot of experimental discrepancies because some delicate physics factors are implicitly involved. Posteriorly, the same group^{14,31–33} studied pressure-induced amorphization (PIA)[†] and linked the chemical effects impact – *i.e.* the originated adsorption of the particles surface as a result of the use of different chemical synthesis methods^{35,36} – to the defects which appeared at the surface of nanoparticles. Furthermore, Piot *et al.*,¹⁴ working with two sample-set of Y_2O_3 – the first batch was stored in the air, and the second one was kept within an argon atmosphere – reported a significant difference between these batches. They related the preexisting conditions (chemi- and physisorption) concluding that different conditions of storage have a fundamental role in the phase transformation.

* The universal relationship is given by the relation $\frac{\phi(R)}{\phi_\infty} = \left(1 - \frac{\alpha(R)}{R}\right)^{1/2S}$. Where ϕ is a physical parameter (such as cohesive energy, melting temperature...); S is a parameter which depends on the statistics, and for a Fermionic system $S = 1/2$; ∞ is related to the bulk phase; and $\alpha(R)$ is a parameter which is dependent on the particle size.

† The sudden transformation from a crystalline material to an amorphous solid, caused by the application of pressure at temperatures relatively below the melting point or the glass transition range, is called pressure-induced amorphization (PIA). Such kinds of transitions will cause significant changes in the physical properties of the solids.³⁴

Size is important, but...

With the objective of finding other parameters to relate to the pressure transition, Machon *et al.*³⁷ worked with four different types of ZnO samples with identical particle sizes which were prepared by different chemical and physical routes. These samples presented more or fewer defects due to different kinetics and thermodynamic pathways, presenting transition pressure and high-pressure phase dependents on the sample source. More recently, Li *et al.*³⁸ studied TiO₂ nanoparticles and confirmed Machon *et al.*'s³² propositions which suggested that the high-pressure phase transitions depend not only on the nano-size, but also on the morphology, the interface energy, and the nanostructure.

All these works reinforce the idea that particle size is not a sufficient parameter when dealing with nanoparticles. A lot of authors considered only the effect of the pressure under the particle size, and we are going to show that an important parameter has never been considered: the defects. Since the particle size decreases the density of defects increases, and we must consider the strong influence of the defects in the phase stability of nanomaterials. So, a bi-dimensional plot is not sufficient to represent the phase stability. The ideal plot should be a multidimensional one (Figure 1) and it should be one that considers the defects as being part of the third axis, following the same way which was proposed by Carencio *et al.*,³⁹ *i.e.* when dealing with the nanoscale phase diagram, they considered the surface contribution to total energy as the third axis. Piot *et al.*²³ reinforced this model when studying ZnO, *i.e.* they considered the defects as being part of the third axis of the multidimensional plot. Following the same train of thought, we found another interesting system to apply these propositions: SnO₂.

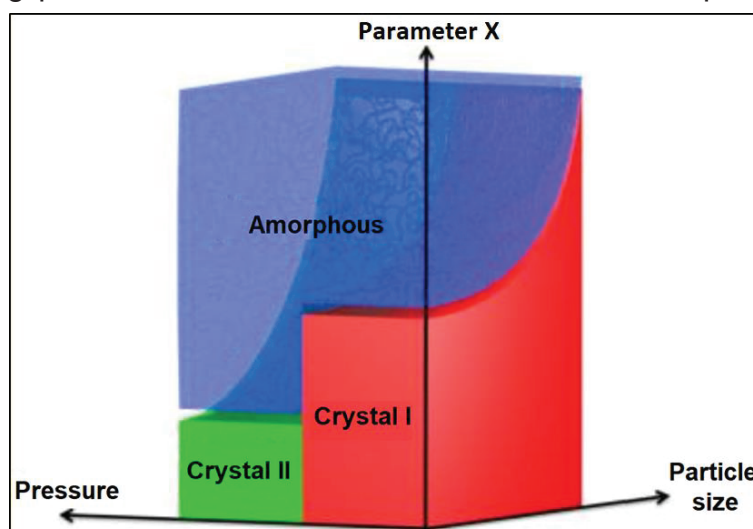


Figure 1 – Representation of the pressure-induced disorder in a multidimensional plot. The axis “Parameter X” considers the nature and the density of the defects. Adapted from ref.23.

The objectives of this work

Why SnO₂?

The choice of SnO₂ as our material was especially motivated by the strong influence of the defects in its properties. Its particle size, crystallinity, electrical properties, morphology, and structure are dependent on the synthesis route,⁴⁰ in the presence of impurities, and on the stoichiometry related to the oxygen.⁴¹ We will show that the defects will influence its properties in both bulk and nanoparticles forms, making it a very adaptable system to test such influence under pressure.

Why Raman as the main technique?

We present here a study of the pressure-induced disorder in SnO₂, going from the bulk (in all its forms: powder and single-crystal) to the nanoparticles, mainly using Raman spectroscopy. The use of this technique had the purpose of complementing and to clarifying the existing X-ray diffraction data (and also the divergences reported in the literature) on phase transitions of SnO₂ bulk and nanoparticles.

In our case, Raman spectroscopy was found to be the best technique due to its sensibility related to the oxygen sublattice.

So what? Why is this model innovative?

If previous high-pressure studies seemed to give a correct model to explain the mechanism of the SnO₂ phase transition, we will show that when decreasing the particle size (powder and nanoparticle) we must use an original framework to describe its structural phase transitions: the decoupling of sublattices during the pressure-induced transformations.

It is important to know that the model which will be described in this study **IS NOT** exclusive to SnO₂. It can be applied to other oxides (compounds) which have peculiar behavior under pressure.

Manuscript organization

This manuscript is divided basically into two parts: the pressure-induced disorder in SnO₂ bulk study– powder versus crystal, and the pressure-induced disorder in SnO₂ nanocrystalline study. In the first chapter, we will present the synthesis method used to produce our nanoparticles and a review of all experimental techniques used here accompanied by their features. In the second chapter, a review of the earlier works, which presents significative results on SnO₂ bulk and nanometric, will be presented. In the third one, we will show, discuss, and share the results obtained in our experiments obtained for SnO₂ bulk – single-crystal versus powder. The fourth chapter is dedicated to the SnO₂ nanometric study, and we will show and discuss all our results here obtained. We wil also find a general conclusion

Chapter 1

Synthesis Methods and Experimental Techniques

Table of contents

Chapter 1	7
1.1. Synthesis method	8
1.1.1. Sol-gel technique: a chemical route.....	8
1.2. The defects on the crystals	9
1.2.1. The types of defects in crystalline solids.....	10
a) <i>Point defects</i>	11
b) <i>Linear defects</i>	14
c) <i>Interfacial or surface defects</i>	15
d) <i>Volume defects</i>	16
1.2.2. The SnO ₂ case.....	17
1.2.3. The impacts of these defects on the SnO ₂ Raman spectra.....	18
1.3. Pressure generator system	20
1.3.1. The Diamond Anvil Cell (DAC).....	20
1.3.2. Pressure Transmitting Medium – PTM and the conditions for compression	24
1.4. Characterization Techniques	26
1.4.1. X-ray Diffraction (XRD).....	26
1.4.2. Spectroscopy Techniques.....	29
a) <i>Raman Spectroscopy</i>	29
b) <i>Photoluminescence (PL) Spectroscopy</i>	35

In this chapter, we will begin by explaining the synthesis method used to prepare our nanoparticles: sol-gel technique (chemical route). Then, we will explain the different ex-situ and in situ characterization techniques used in this study, at ambient pressure, and under high-pressure: X-ray diffraction, Infrared Spectroscopy, Raman Spectroscopy and Photoluminescence Spectroscopy. We will present a brief review of each one of these techniques with their own specific vocabulary, physical principles, and features. And finally, we will discuss the devices used to generate the high-pressure during our experiments.

1.1. Synthesis method

1.1.1. Sol-gel technique: a chemical route

Sol-gel is a wet chemical technique widely employed in the fields of materials science and ceramic engineering. It is utilized primarily for the fabrication of materials (typically a metal oxide) starting from a chemical solution which acts as the precursor for an integrated network (or gel) of either discrete particles or network polymers. It usually consists of four steps: *(i)* the dispersion of colloidal particles into a liquid, to form a sol – this is the dispersion of the solid particles ($\sim 0.1 - 1 \mu\text{m}$) in a liquid where the particles are suspended by the Brownian motions; *(ii)* the deposition of sol-solution produces the coatings on the substrates by spraying, dipping or spinning; *(iii)* the polymerization of the particles of sol through the removal of the stabilizing components and produce a gel – it is a state where both, liquid and solid, are dispersed in each other, which presents a solid network containing liquid components – in a state of continuous network; and finally *(iv)* the pyrolysis with heat treatments of the remaining organic or inorganic components and formation of amorphous or crystalline coatings.^{42–45}

Many advantages of the sol-gel process can be listed such as *(i)* better homogeneity from raw materials; *(ii)* production of high-quality products – as the organo-metallic precursor of the desired ceramic oxides can be mixed, dissolved in a specified solvent, hydrolyzed into a sol, and subsequently into a gel – with a composition which can be highly controllable; *(iii)* lower temperature of preparation, usually between 200°C and 600°C ; *(iv)* it can produce thin bond coating to provide excellent adhesion between the metallic substrate and the top; *(v)* good mixing for multi-component systems; *(vi)* can easily shape materials into complex geometries in a gel state; *(vii)* can provide a simple, economical and effective method to produce high quality coatings, etc.

In the production of nanoparticles, this technique presents some limitations⁴⁶ such as *(i)* the presence of ligands at the surface; *(ii)* high cost of raw materials; *(iii)* it is very substrate-dependent; *(iv)* it has a long processing time (\sim two days); *(v)* the thermal expansion mismatch limits the wide application of this technique, etc.

1.2. The defects on the crystals

The perfect crystal, with zero defects, is never found in nature. At any temperature above 0 K, all crystalline solids will contain vacancies and extra atoms, and will exhibit deviations from the ideal structure.^{47,48} The presence and the number of defects depends on: the temperature; the purity of the crystal; the type of chemical bond; the method of preparation; as well as the thermal and / or mechanical treatments undergone. Defects are naturally present in the material and they play a crucial role in the optical, electrical and mechanical properties of crystals. They appear principally during the formation process of the material, however, and as they influence the material properties, they can be purposefully created. For example, in metal oxide crystals, the defects can be introduced by doping^{49,50} or by varying the oxygen stoichiometry,⁵¹ which leads to the modification in the electronic band structure of the material.⁵² The most important characteristics of the microstructure of an engineering material appear when the crystalline defects are inserted to control its behavior and properties. For example, in order to control the type and the concentration of charge carriers,⁵³ point defects are intentionally added to semiconductors.

The coloring of precious stones is an emblematic example of the influence of defects on the physical properties of materials. The great variety of color observed is related to the existence of point defects⁵⁴ (vacancies, substitutional impurities) or association of point defects (inclusions of molecular ions). Generally, the pure and defect-free crystals are transparent. In the case of SnO₂, the reason for the coexistence between electrical conductivity and optical transparency⁵⁵ is still unclear, however, for a material to be transparent, the band gap must be greater than the highest frequency of visible light, *i.e.*, it must be greater than 3.1 eV.^{56,57}

Point defects may affect the conductivity in both metals and semiconductors. A modification in the electronic band structure of the material is expected when defects are introduced in metal oxide crystals, by doping or by varying the oxygen stoichiometry.⁵² The metals have free charge carriers at all temperatures, so, the resistivity is then governed by the mobility of these carriers. In this case, the impurities increase the resistivity by disturbing the path of the electrons. In the of the semiconductors the conduction is provided by a small number of electrons that relocate as the temperature increases. In the case of the SnO₂, for example, the oxygen

deficiency may be caused either by oxygen vacancies or tin interstitials, with reduction of some Sn (IV) ions to Sn (II), as a possible charge compensation mechanism. So, the electronic conductivity could then occur due to the mobility of electrons from Sn (II) to Sn (IV) sites.⁵⁷

Dislocations play a fundamental role during plastic deformation. In addition, the interaction of dislocations with other types of defects influences the hardness of the material.

In this section, we review the different types of defects that we can find on the crystals and, to finalize, we will discuss the case of our material, the SnO₂.

1.2.1. The types of defects in crystalline solids

In a perfect crystal, there are microscopic region in which an atom is surrounded by close neighbors, in specific positions. When these positions are different from those expected, *i.e.*, when there is a break in the periodicity regularity of the spatial configuration of atoms, we have the *defects*. Traditionally, a lot of kind of defects can be distinguished, and based on their “dimensionality”. They can be divided into four categories: point (0D), linear (1D), planar (2D), and volume (3D) defects. In Figure 2 below, you can see a scheme that resumes these defects. Even if we will be more interested on point defects, I will make a succinct review of the others.

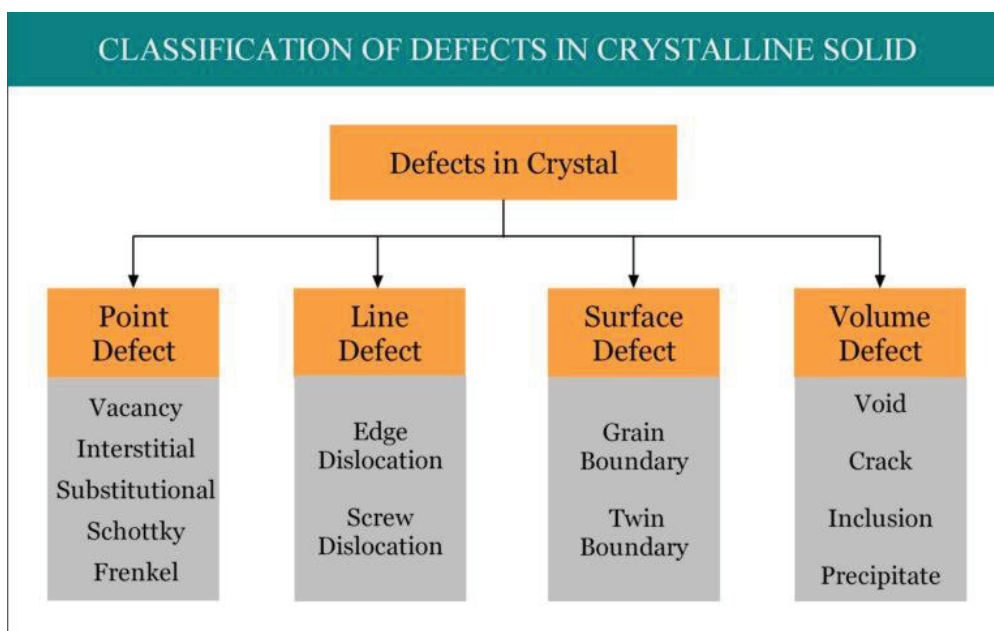


Figure 2 – Classification of the different types of defects that can be found in a crystal. Adapted from ⁵⁸

a) Point defects

When the volume of the disturbed region of the crystal is of the magnitude order of the volume of a single atom or of a few atoms, we have point defects.^{59–61} It results in a disturbance of the crystalline order on dimensions limited to a crystallographic mesh. It can be intrinsic or extrinsic defects.

(i) ***Intrinsic defects:*** is formed when an atom is missing from a position that ought to be filled in the crystal, creating a *vacancy*, or when an atom occupies an interstitial site where no atom would ordinarily appear, causing an *interstitialcy*. In ionic compounds, two types of defect structures involving point defects have been found to be important in stoichiometric metal oxides: *Schottky* and *Frenkel* defects.

- A vacancy corresponds to a void left in the structure on a site normally occupied by an atom (Figure 3a).
- An interstitialcy happens when extra atoms in a structure or impurities placed on normally empty sites (Figure 3b).

The point defects in stoichiometric metal oxides (MO): If a charged point defect is formed in such a crystal, a complementary point defect with opposite effective charge must be formed to conserve the electroneutrality of the stoichiometric crystal.

- A Schottky defect^{62,63} is a vacancy in an otherwise perfect arrangement of atoms or ions in a structure, *i.e.*, it is a point defect in which an atom or ion is missing from its normal site in the structure. (Figure 3c). The overall stoichiometry of a solid is not affected by the presence of Schottky defects because, to ensure charge balance, the defects occur in pairs in a compound of stoichiometry MO and there are equal numbers of vacancies at cation and anion sites. In solids of different composition, for example MO₂, the defects must occur with balanced charges, so two anion vacancies must be created for each cation lost.

- A Frenkel defect^{63,64} is a point defect in which an atom or ion has been displaced onto an interstitial site (Figure 3d). The stoichiometry of the compound is unchanged when a Frenkel defect forms and it is possible to have Frenkel defects involving either one (M or X displaced) or both (some M and some X interstitials) of the ion types in a binary compound, MX. A useful generalization is that Frenkel defects are most often encountered in structures such as wurtzite and sphalerite in which coordination numbers are low (6 or less) and the more open structure provides sites that can accommodate the interstitial atoms.

(ii) Extrinsic defects: are foreign atoms, which are called *solutes* if they are intentionally added to the material and are called *impurities* if they are not.

- Impurity – these point defects are found in solid solutions, of which there are two types:

Substitutional impurity atom: On this type of defect, an atom occupies a site normally occupied by a different chemical atom (Figure 3e).

Interstitial impurity atom: For interstitial solid solutions, impurity atoms fill the voids or interstices among the host atoms (Figure 3f).

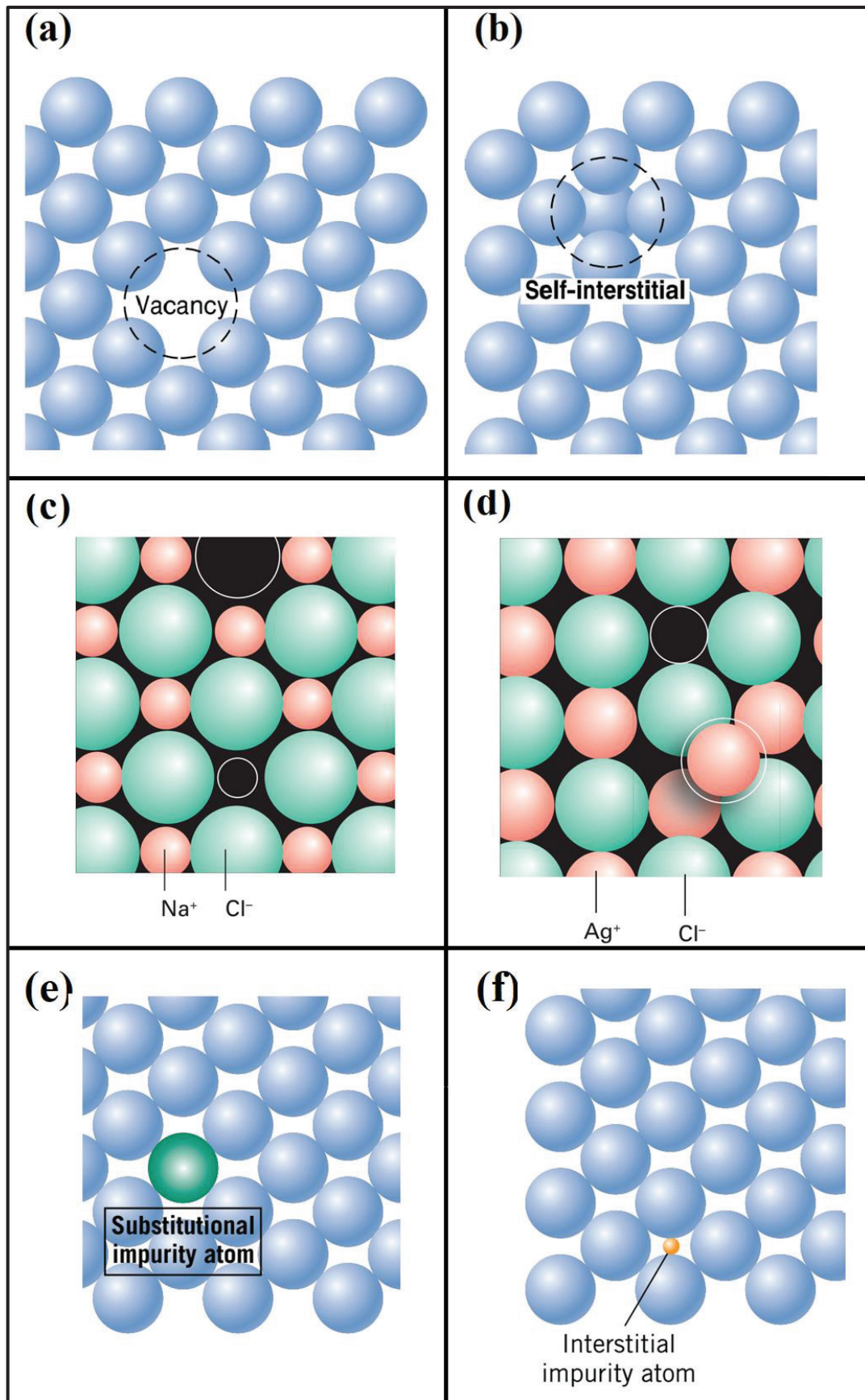


Figure 3 - Examples of simple point defects. (a) Vacancy. (b) Self-interstitial atom. (c) A Schottky defect (absence of ions on normally occupied sites; for charge neutrality there must be equal numbers of cation and anion vacancies in a 1:1 compound). (d) A Frenkel defect (it forms when an ion moves to an interstitial site). (e) Substitutional impurity atom (f) Interstitial impurity atom. Adapted from refs. 61,63

b) Linear defects

The linear defects^{59,61,60} observed in the crystals are called dislocations. Dislocations are obtained by sliding a portion of the crystal along a plane. The line of dislocation proper corresponds to the line of the sliding plane separating the part of the crystal which has slipped from that which has remained motionless. There are two kinds of dislocations:

- (i) **Edge dislocation**: the lower half of the crystal has an additional half-atomic plane. The upper edge of this half-plane constitutes the dislocation line. The atoms on this line do not have the same number of neighboring prime atoms as the other atoms in the crystal. The dislocation also induces an important field of displacement of the atoms in its close environment (Figure 4a).
- (ii) **Screw dislocation**: The portion of the crystal which is in the right side of the sliding plane and above the dislocation line (OP) undergoes a sliding with respect to the crystal below (Figure 4b).

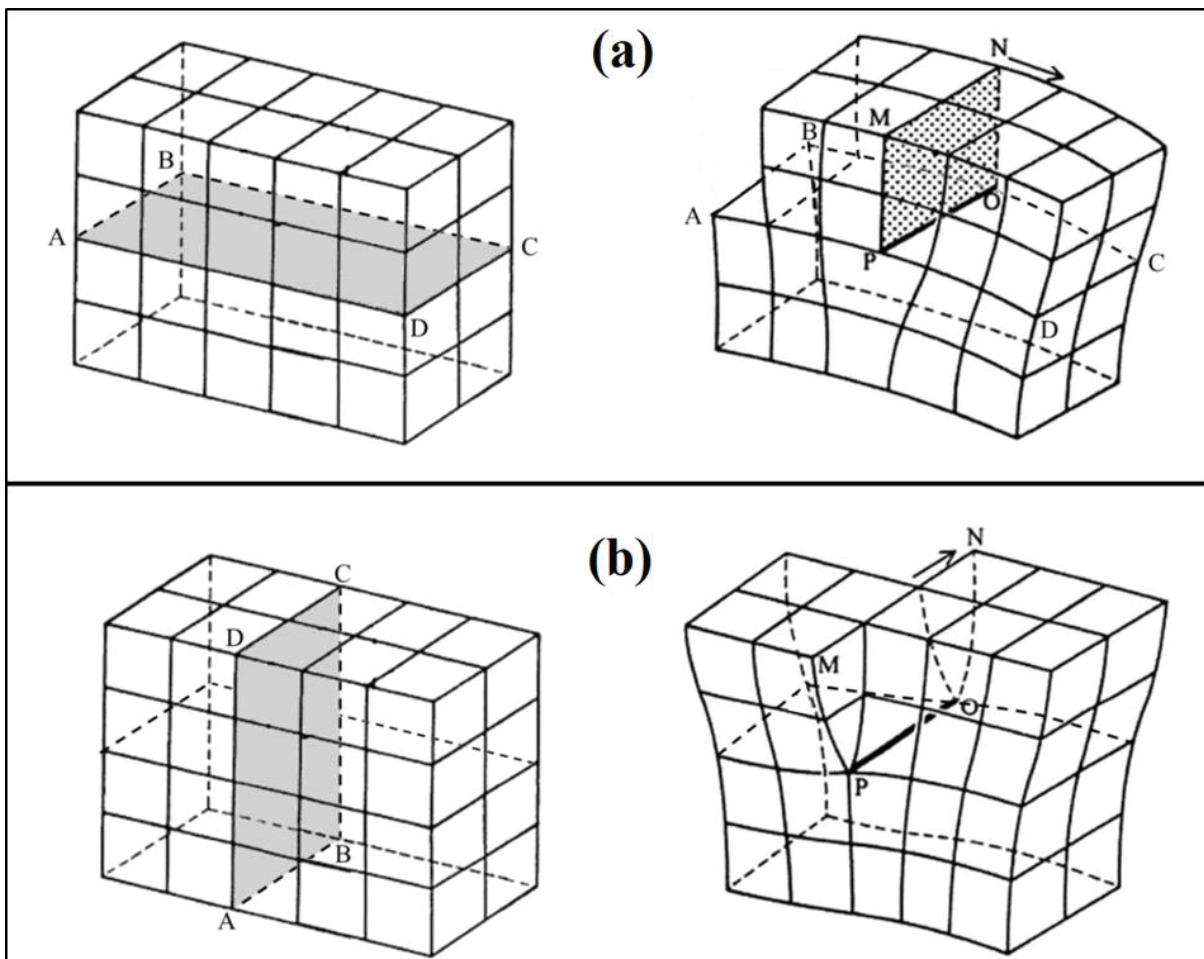


Figure 4 – Dislocations: (a) Edge type. (b) Screw type. Adapted from ref. ⁶⁰

c) Interfacial or surface defects

Interfacial defects,⁶¹ or surface defects, are boundaries that have two dimensions and normally separate regions of the materials that have different crystal structures and/or crystallographic orientations. These imperfections include:

- (i) External surfaces: This kind of imperfection is one of the most obvious, along which the crystal structure terminates. Considering that the surface atoms are not bonded to the maximum number of nearest neighbors, they will be in a higher energy state compared to the atoms at interior positions. The bonds of these surface atoms that are not assured will generate a surface energy.
- (ii) Grain boundaries: Such kind of defect happens when the boundary separating two small grains or crystals have different crystallographic orientations in polycrystalline materials (Figure 5a and Figure 5b).
- (iii) The phase boundaries exist in multiphase materials, wherein a different phase exists on each side of the boundary; furthermore, each of the constituent phases has its own distinctive physical and/or chemical characteristics.
- (iv) Twin boundaries are a special type of grain boundary across which there is a specific mirror lattice symmetry; that is, atoms on one side of the boundary are located in mirror-image positions of the atoms on the other side. (Figure 5c)
- (v) Stacking faults: Stacking defects are also common in compact structures formed by metals (Figure 5d).

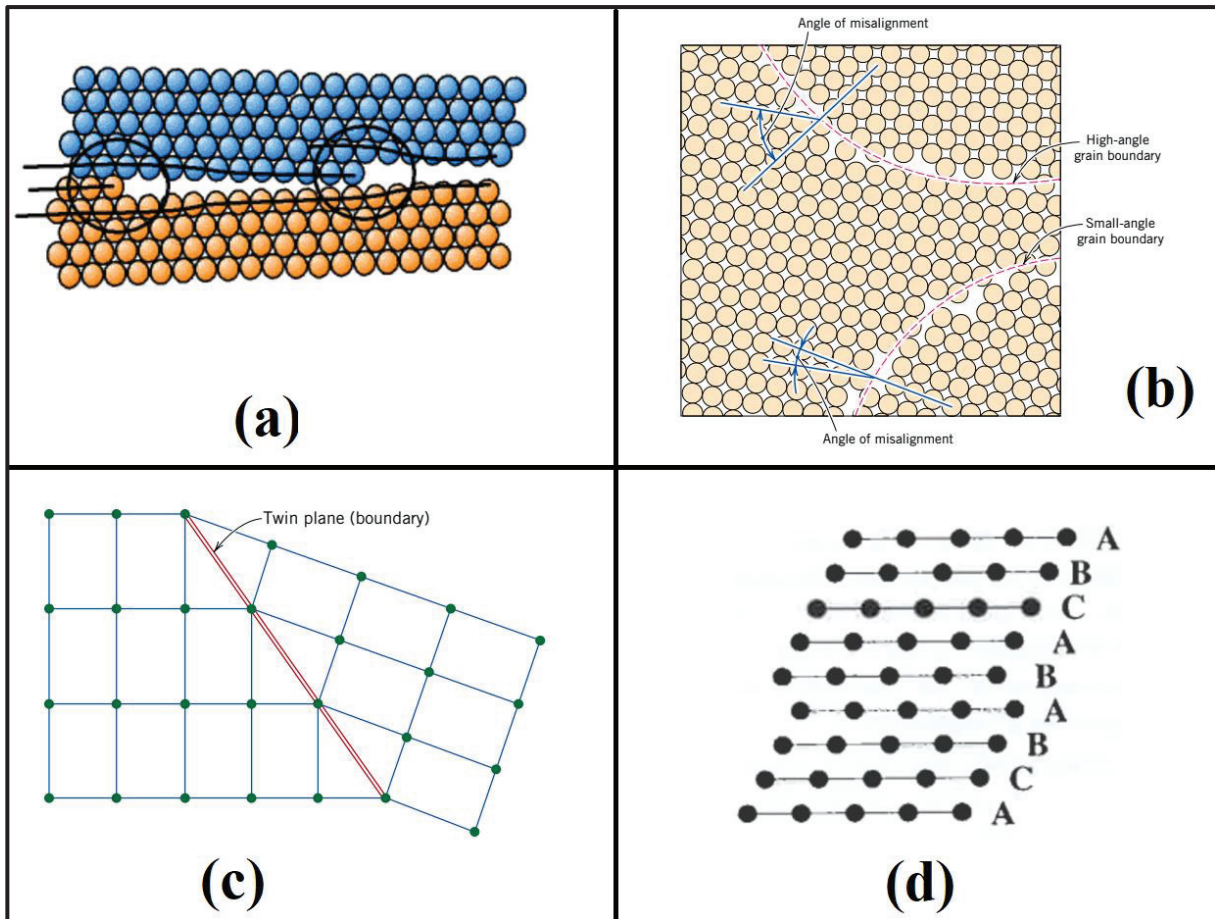


Figure 5– (a) Schematic representation of the arrangement of atoms at a grain boundary in a polycrystalline sample. The grain boundary, an area between two adjacent crystallites, is a defect that corresponds to both a crystalline orientation discontinuity and a zone in which the relative positions of the atoms do not correspond to the equilibrium positions minimizing the 'interaction'. (b) Schematic diagram showing small and high-angle grain boundaries and the adjacent atom positions. (c) Schematic diagram showing a twin plane or boundary and the adjacent atom positions (green circles). (d) Stacking fault produced by the absence of a plane C in the sequence ... ABC ABC A ... constituting a compact cubic structure. Adapted from ⁵⁹ and ⁶¹.

d) Volume defects

Other defects exist in all solid materials that are much larger than those heretofore discussed. These include pores, cracks, foreign inclusions, and other phases. They are normally introduced during processing and fabrication steps.

1.2.2. The SnO₂ case

Oxides in equilibrium with their surroundings are thus generally *nonstoichiometric*, except under specific conditions of temperature and activities of the components.⁶¹ The metal oxides systems, of general formula MO, present predominantly point defects *i. e.*, defect associated to one lattice point,⁶⁴ such as cation or oxygen ion vacancy. The semiconducting nature of these oxides comes from such ability to be under or on stoichiometry. These differences are the result of the presence of more or less ionized point defects in the crystal lattices of these oxides. These may be anionic vacancies or interstitial cations that release electrons and render the *n*-type semiconductor material, or cationic vacancies or interstitial anions that release electron holes and render the semiconductor material of type *p*.

According to the nature of the predominant defects in the solid, we can find the four forms of oxides: MO_{1+x}, M_{1+x}O, MO_{1-x}, M_{1-x}O (M = metal, O = oxygen, x = deviation from stoichiometry). The four types of solids are shown in Figure 6. The oxides of the Figures 6a and 6b are *n*-type and the two others (Figures 6c and 6d) are *p*-type.

The SnO₂, for example, it tends to be sub-stoichiometric in oxygen (SnO_{2-x}). Empirically, it is known that intrinsic defects in SnO₂ give rise to oxygen mesh sub-stoichiometry and *n*-type conductivity; however, the atomistic nature of the defects is unclear.⁵⁷ As a result of the laws on point defects, the oxygen vacancies cause the presence of free electrons in the crystal lattice of the oxide, consequently an increase in the free carrier concentration, which confers the character *n* of such semiconductor.

Due to the sub-stoichiometry in oxygen, the SnO₂ can be applied as a sensor⁶⁵ for detection of reducing gases. Adsorption of oxygen on the surface of doped tin oxide leads to trapping of charge in ionic species such as O₂⁻, O₂⁻² or O⁻². The reaction between the reducing gas and the surface-adsorbed oxygen releases carriers into the bulk and there is an associated increase in conductivity which forms the basis for the sensor devices.

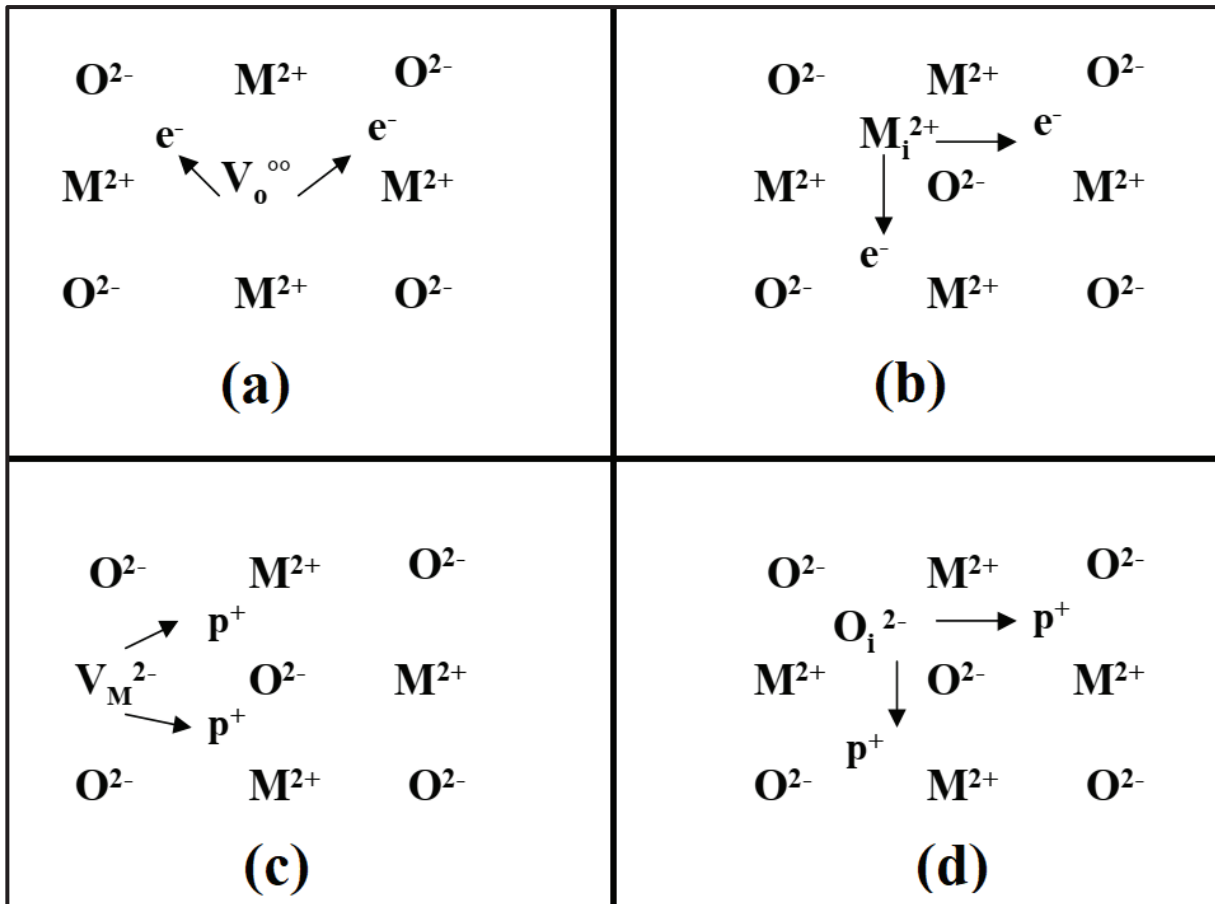


Figure 6 – The four types of semiconductor metal oxides: (a) Oxygen vacancies (n-type), (b) Interstitial metal (n-type), (c) Metal vacancies (p-type), and (d) Interstitial oxygen (type p). Adapted from ref. ⁶⁵

1.2.3. The impacts of these defects on the SnO₂ Raman spectra

When defects are introduced in a material (purposely or not), one of its consequence is the broadening of Raman lines. Such broadening is generally taken as an evidence of the disorder which tends to break the momentum conservation ($k = 0$) selection rule and permit phonons from other parts of the Brillouin zone to contribute to the Raman scattering.⁶⁶

As an example, we have the Figure 7 below. Comparing bulk and nanoparticle, we can see that there is a band at 575 cm⁻¹. Such band may be assigned to surface defects of the SnO₂ nanocrystals. The same kind of behavior is expected on our samples.

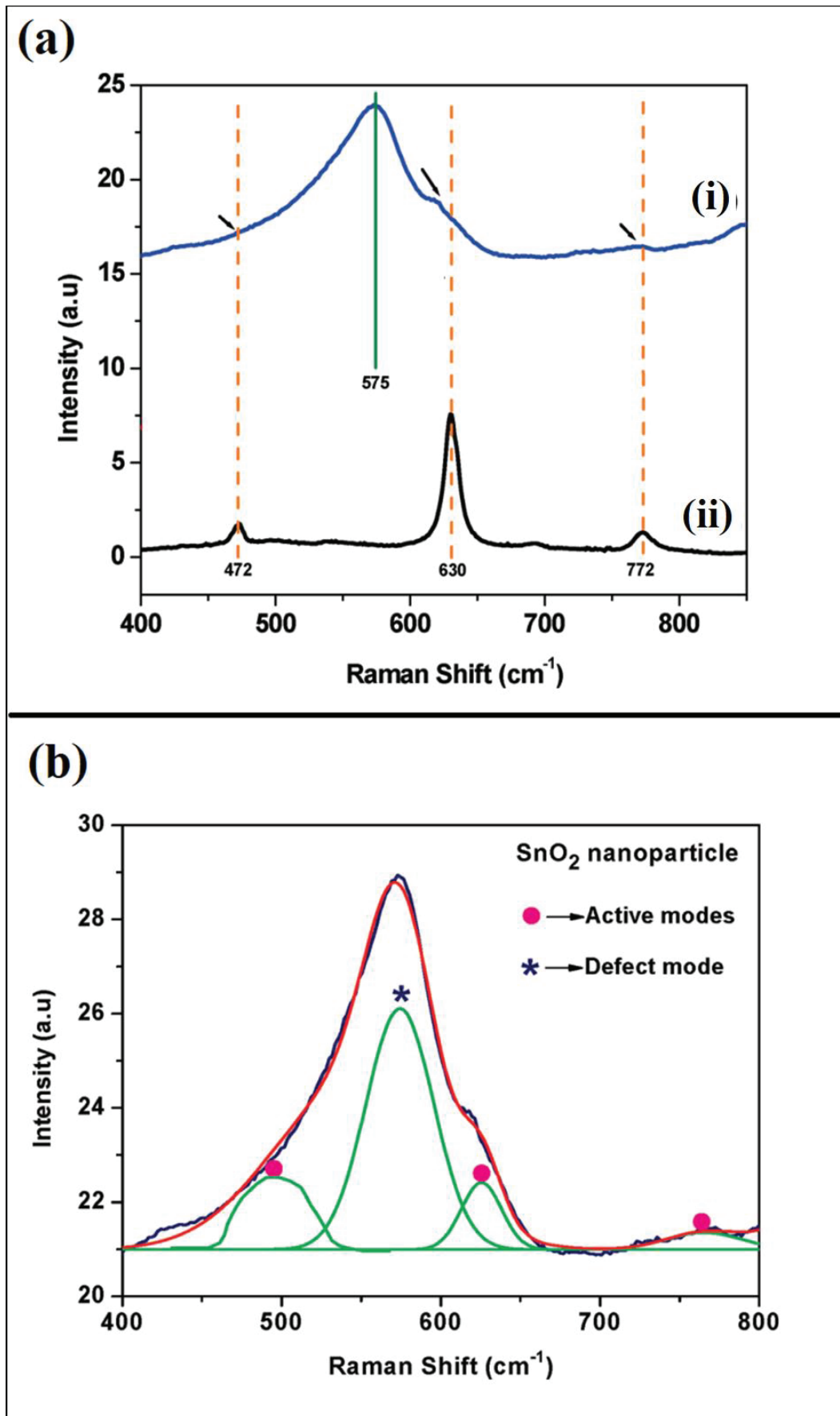


Figure 7 – Raman spectra of (a.i) SnO₂ nanoparticles SnO₂, (a.ii) SnO₂ bulk. (b) Deconvolution fitting plots of the Raman spectra from SnO₂. Adapted from ref. 67

1.3. Pressure generator system

1.3.1. The Diamond Anvil Cell (DAC)

In the 1950s, the diamond anvil cell (DAC) was first developed in the United States, then in France. The DAC can be used to perform high-pressure, the high temperature in Raman spectroscopy experiments and it is also used in electrical resistance and compressibility measurements. Diamonds are used in it because of their optical properties – they are transparent to visible light, they have low luminescence and the light can pass throughout it easily

Diamond is the hardest substance known to man, is chemically inert and it exhibits a phase transition – to a carbon liquid phase – at a very high temperature vs. high-pressure ($\sim 4200\text{K}$ vs. 10GPa). These values (combined) are out of our working range, as can be seen in Figure 8. In addition, as their transparency is over a wide band of wavelengths, from infrared to X-rays and gamma, it is possible to measure *in situ* the properties of materials at high-pressure and variable temperature.

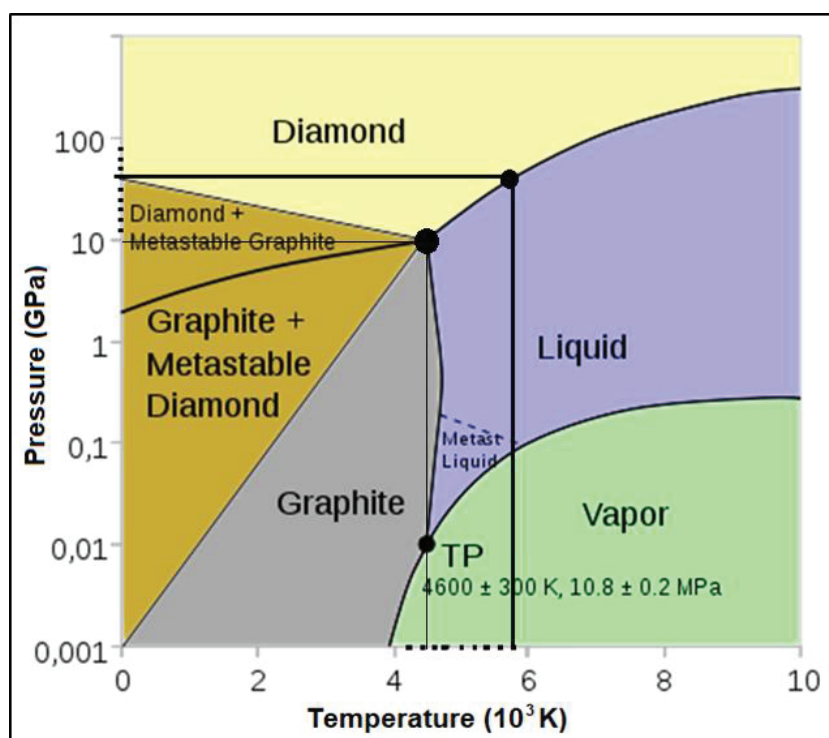


Figure 8 – Carbon phase diagram. Adapted from ref.⁶⁸

A diamond anvil cell (Figure 9) consists of three main parts: a fixed cylinder onto which a diamond is set, a movable piston with a diamond also fixed and a screw cap provided with a metallic membrane. Between the diamonds, there is an indented gasket in which, the sample, the ruby, and the pressure medium transmitter (PTM) are put inside the hole.

Piermarini *et al.*⁶⁹ demonstrated that a small chip or sphere of a ruby doped with Cr^{3+} ions ($\text{Al}_2\text{O}_3:\text{Cr}^{3+}$), placed in the compression chamber (Figure 10), could serve as a continuous pressure sensor within the DAC by utilizing its laser-induced fluorescence. The pressure in the diamond cell can be calibrated by the fluorescence emitted by the rubies when they are illuminated by a laser beam.⁷⁰ This information is then analyzed by a spectrometer. When pressure is applied, the energy displacement is measured by the position of the displacement of luminescence lines. The inset in Figure 10 shows the shift of the fluorescence lines with the pressure, which is then used to calibrate the pressure.



Figure 9 – Block diagram of the diamond anvil cell. This consists of three main parts: the piston and the cylinder which form the body of the cell, and the cover containing a metallic membrane.

Figure 10 – Schematic section of a diamond anvil cell (DAC)⁷⁰

The principles

The device for generating high-pressures is based on a simple physical principle:

$$p = \frac{F}{A} \quad (1)$$

Where p is the pressure, F is the applied force and A is the area. So, to reach high-pressures it is necessary to apply a strong force on a little surface, one which is as small as possible. However, this is a complex and costly realization.

Usually, there are two options to increase the pressure: (1) increase the force, and (2) decrease the area. Option 1 presents problems related to material resistance, and user safety whenever one wishes to reach very high-pressures. Therefore, option 2 remains the only viable option to achieve these "extreme" conditions. The major restriction will be to work with very small sample volumes. Seeing Figure 11, we can better understand the DAC principle.

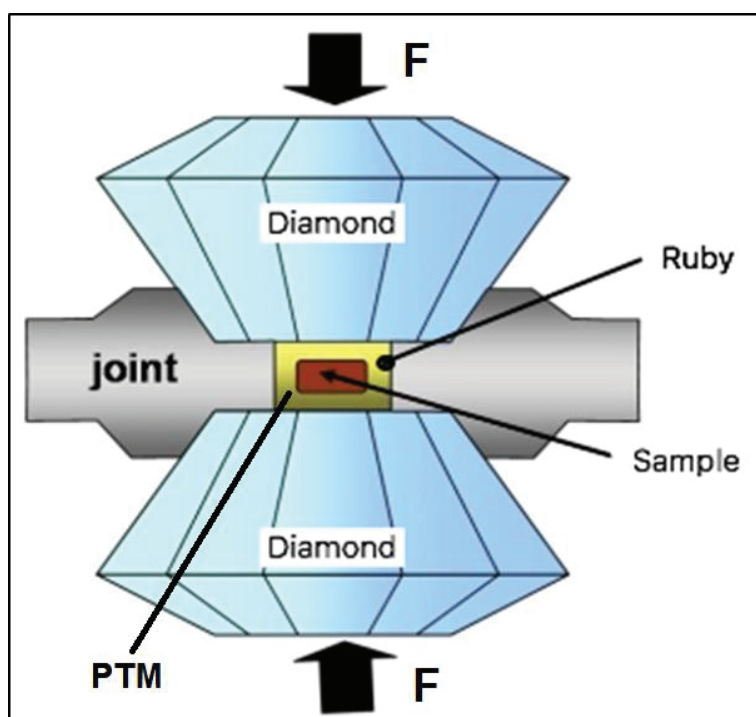


Figure 11 – Principle of the Diamond Anvil Cell.⁷⁰

The Equipment and the Experiment

As previously shown in Figure 9, a DAC is composed of a fixed cylinder onto which a diamond is set, a movable piston with a diamond also fixed, and a screw cap provided with a metallic membrane. The force is transmitted from the membrane to the diamonds. Since the surface which is in contact with the sample is very small, the pressure generated is high. The metal seal prevents the diamonds from touching one another and allows the sample to be confined.

The principle of its use is simple. Firstly, a gasket (metal foil of about 30-50 μm) is placed in the cylinder diamond; the piston is put in place, and the cover is screwed onto the diaphragm. The first function of the gasket is to avoid contact between the diamonds, otherwise one risks the fracturing of the latter, and the second function is to serve as support for the samples. Secondly, a gas pressure (helium) is injected into the membrane, deforming it. Next, the force is transmitted to the piston, which moves a few tens of microns and deforms the joint. After this, the membrane is deflated, the cell is opened, and the metal joint is recovered. Thereafter, a cylindrical hole is made by electro-erosion in the center of the impression left by the diamonds. This will constitute the compression chamber into which the sample will be inserted. Thereon, we relocate the metal seal but taking care to place it correctly with respect to the diamonds. After this, with the help of an optical microscope, the sample, a ruby, and a pressure transmitter medium (usually a liquid to ensure hydrostatic pressure) are placed in the compression chamber. Since the sample is confined, it will not be extruded during the pressure build-up.

The experiment starts: the cell (piston and membrane) is closed and helium gas is injected into the membrane, which applies pressure to the sample. The measurements are performed by making pressure intervals. When maximum pressure is achieved, the pressure is released slowly until again reaching ambient pressure, but without forgetting to do the measurements on release.

In our Raman experiments, the high-pressure (HP) was generated using a Chervin-type DAC membrane (see Figure 12a) with low-fluorescence diamonds and with a culet diameter of 400 μm (micrometers). Hardened stainless steel gaskets pre-indented to a thickness of 50 μm served as the high-pressure chamber. As the micro-powders as the nanoparticles were put into a chamber which was drilled in a pre-

indented stainless-steel gasket with a needle of 125 μm in diameter, and pressure up to $\sim 28\text{GPa}$ was achieved using this configuration. For the single crystal, the hole was 150 μm in diameter, and pressure up to $\sim 23\text{GPa}$ was achieved. The pressure was probed by the shift of the R1 fluorescence line of the small ruby sphere.

In our X-ray experiments with nanoparticles, the high-pressure (HP) was generated using an Almax-type DAC membrane (see Figure 12b). The SnO_2 nanoparticles were placed into a 250 μm chamber drilled in an indented stainless-steel gasket, along with a ruby acting as a pressure gauge. We could achieve a pressure up to $\sim 13\text{GPa}$ with such DAC.

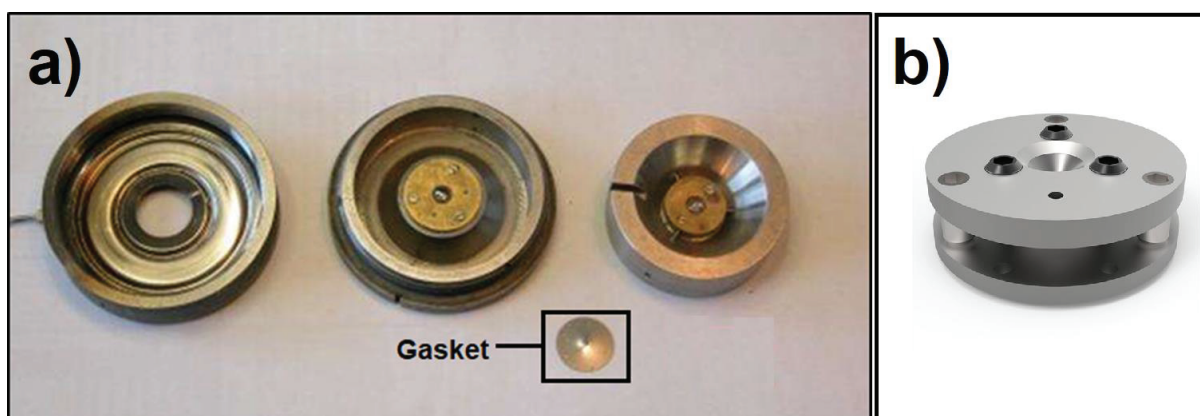


Figure 12 – a) Chervin-type DAC membrane used in the Raman spectroscopy experiments at the high-pressure . b) Almax-type DAC membrane used in X-ray experiments at the high-pressure.

1.3.2. Pressure Transmitting Medium – PTM and the conditions for compression

It is common to use pressure transmitting medium to limit purely uniaxial stress and to ensure hydrostatic compression on the sample. Hydrostatic pressure is preferred for high-pressure experiments because the variation in the strain throughout the sample can conduct to distorted observations of different behaviors. In order for the pressure to be as hydrostatic as possible (*i.e.* it has the same value at all points in the medium) the ideal situation is to use a liquid or a soft solid as they are not very “compressible”, contrary to gases.

The choice of a transmitting medium for filling the gasket hole in pressure studies is a crucial problem.⁷¹ It is necessary that no disturbance from the medium exists. Such disturbance could cause interference of the signal of the sample (presence of fluorescence, superposition of the signal with peaks of interest, etc.). Moreover, one of the most important aspects is the absence of reactivity between the transmitting medium and the sample.

The pressure values corresponding to the hydrostatic limits of several different fluids were determined^{72,73} by using the ruby line broadening, or by measuring the pressure homogeneity with several ruby chips distributed randomly over the area of the gasket aperture.

The requirements for a good pressure transmitter medium are chemical inertness, being easy to load, having a zero-shear stress, and a low cost. The most frequently used media are: (i) mixture of alcohols – methanol: ethanol: (water) – that turns into solids at pressures of a few GPa; (ii) ionic solids as NaCl, KCl or KBr – they are easy to load, and they might also serve as a thermal insulator. Even if such ionic solids are transformed into compressible solid at low pressures (a few GPa), they can provide very hydrostatic pressure conditions up to several hundred GPa. And (iii) rare gases such as: Argon – cryogenic loading, gas loading, and thermal annealing possible; Neon – gas loading and high-pressures can be achieved; or Helium – gas loading, very high-pressures can be achieved but with no high temperatures. Rare gases do not produce detectable shear stress even in their solid phase.

When dealing with highly reactive nanoparticles, the reactivity of the transmitting medium is extremely problematic and the influence of the environment on nano-systems, like adsorption, intercalation, etc., can cause significant changes in pressure behavior.^{74,14,23,75} When we work with a hydrostatic medium, it is reasonable to estimate that the stress distribution is homogeneous around the nanoparticles. Although the surface of the nanoparticles is subjected to high micro-stresses, the compression conditions transmitted to the core of the nanoparticles can be estimated as quasi-hydrostatic. Except when using ultra-fluid media such as helium, it is reasonable to wonder whether the other transmitting media (ethanol/methanol, paraffin, etc.) individually cover each nanoparticle or whether they enclose a cluster of nanoparticles directly in contact with one another. The last case amounts to considering isostatic compression equivalent to that obtained in the absence of transmitting media.

1.4. Characterization Techniques

1.4.1. X-ray Diffraction (XRD)

The Principles

The X-ray diffraction is one of the most used *in situ* methods to characterize the structure and symmetry of materials under high-pressure in order to study their crystal structure. This probe ability is due to the X-rays wavelengths, which are of the same order of magnitude as the interatomic distances ($\sim\text{\AA}$) in the crystals.

The physical principle consists: when an X-ray beam hits a crystal, the waves are scattered in all directions throughout the crystal structure. In some directions, the scattered waves undergo a destructive interference resulting in a minimum of intensity while, in other directions, the interference is constructive, resulting in a maximum of intensity.

The constructive interference of the scattered waves is based on Bragg law⁷⁶ (see Figure 13). This law measures the angle at which the intensity is at a maximum and this varies with the interatomic distances of the material. This can be seen in the equation below:

$$n \cdot \lambda = 2d_{(hkl)} \sin \theta \quad (2)$$

Where θ is the angle between the incident beam and the planes (hkl); $d_{(hkl)}$ is the distance between two crystalline planes with Miller's indices (hkl); λ is the wavelength of X-rays; and n is the interference order.

Figure 13 describes the diffraction condition by considering the phase difference of the wave between two consecutive lattice planes. These planes act as mirrors when X-rays irradiate the material.

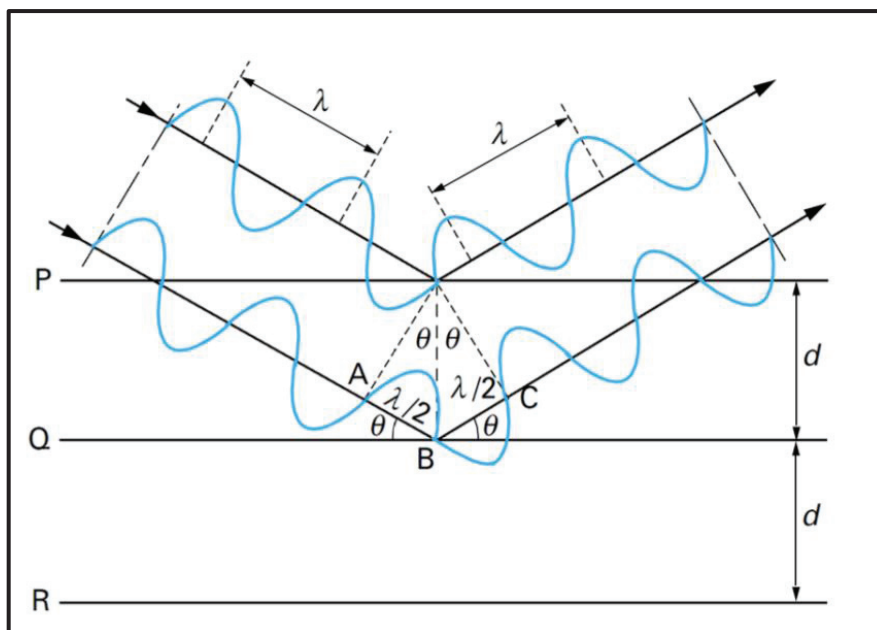


Figure 13 – A schematic reflection of radiation by the lattice planes according to Bragg's law.⁷⁷

The use of XRD is based on the differentiated absorption of their photons by different elements of the material: the beam that passes through more absorbent elements has less intensity than the one that crosses through less absorptive ones.⁷⁸ So, higher atomic number elements – such as calcium ($Z = 20$), barium ($Z = 56$), tin ($Z=50$) and iodine ($Z = 53$) – are better X-ray absorbers than lower atomic number elements – such as hydrogen ($Z = 1$), carbon ($Z = 6$) and oxygen ($Z = 8$). In other words, the scattering of X-rays by atoms is dependent on the atomic number Z .⁷⁹

Different crystal structural characteristics of the material could be accessed their diffraction patterns are analyzed. Lattice elementary symmetry, size, shape, and residual strain can be accessed by the measurements of Bragg angle θ , by the intensity I of each hkl reflection, and by the FWHM values. The phase can be identified by the number of reflections, the peak position, and the peak splitting. The crystalline structure is determined by the position, the intensity of the peaks, and as well as by the calculation of its lattice parameters averaged over the whole volume of the sample illuminated by the beam. The phases can thus be identified by comparing the experimental diagram with reference diagrams (databases ICDD, JCPDS, ...) or by simulating the diffractograms of structures expected for a given material. In these experiments, the recognition of the phases was routine when carried out on the data basis of PDF – 4+ (ICDD) via DIFFRAC.EVA program, distributed by Bruker AXS.

The X-ray data can also be used to estimate the particle size of the particles, from the diffraction line broadening. In fact, it estimates the length of the coherence domains *i.e* where the domains crystallize. Such broadening results from the finite size of the coherently diffracting domains inside the grains. However, specifically for nanocrystallites cases, an enlargement of the diffraction patterns can be observed because the lattice can no longer be approximated infinitely. Such broadening is frequently used as a first approximation to determine the crystallites size D using the Scherrer method, as can be seen in the equation below:

$$D = \frac{k\lambda}{\beta \cos\theta} \quad (3)$$

where β is the half-height width of the considered peak at an angle θ and k is a constant equal to 0.9 (when the width is taken at mid-height). The local variation of the lattice parameters tends to create micro-deformations, which generates the dispersion of the inter-reticular distances around an average value.⁸⁰ The effect of these micro-deformations is thus manifested by an additional contribution to the widening of the diffraction peaks showing a disorder.

X-ray Diffraction Limitations

X-ray technique is based on the presence of a crystalline lattice or on the periodicity of the atomic arrangement. So, amorphous solid materials such as glass, polymers or liquids cannot be analyzed by DRX.⁸¹

Another limitation of this technique is the size.⁸² It is much more accurate when measuring large crystalline structures rather than small ones. Small structures that are present only in trace amounts will often go undetected by XRD readings, which can result in skewed results. So, when dealing with nanoparticles, the broadening of the peaks is understandable as decreasing size leads to an increase in the disorder.

1.4.2. Spectroscopy Techniques

The study of the interaction between matter and electromagnetic radiation is called spectroscopy.^{83,84} Spectroscopy was originally studied by measuring the scattering of visible light through a prism according to its wavelengths. Afterward, the idea has been broadly expanded to include any interaction with radiating energy as a function of its wavelength or frequency. Spectroscopic data are commonly represented by an emission spectrum and, in response, a graph is plotted as a function of wavelengths or frequency.

There are a lot of spectroscopy techniques.⁸⁵ However, because of our needs, *i.e.* to study the SnO₂ sublattices behavior, only two of them were used in this work: Raman and photoluminescence. Even though all of these two processes pertain to the interaction between matter and radiation, each of them is based on a different physical phenomenon. On the one hand, Raman spectroscopy is governed by the scattering of light by matter. On the other hand, a lot of materials can emit visible luminescence when subjected to some form of excitation such as UV light, and this phenomenon is called photoluminescence. These two specific spectroscopy techniques will be better explained in the next subsections.

a) *Raman Spectroscopy*

Raman radiation was first documented by Raman and Krishnan⁸⁶ in 1928. This technique is based on the process of scattering light through matter⁸⁷, *i.e.*, an inelastic interaction between the electromagnetic wave and the material, and it is one of the non-destructive optical techniques most widely used. Samples of any size or shape can be used and no sample preparation is needed. Furthermore, samples can be analyzed directly in bottles, bags, or blisters.

Raman spectroscopy is also one of the most important methods used to obtain information on vibrational states. Moreover, it is an advantageous method used to evaluate microcrystal samples because the Raman scattering of the microcrystal is sensitively influenced by the condition of the surface (the presence of disordered interfacial regions and the presence of stress on the microcrystal's surface, etc.). Such technique is also sensitive to crystalline defects. It can be used to characterize the disorder in materials, detect the presence of crystalline defects, and determine the size

of the crystallites. Through the characterization of bonds and crystal symmetry, Raman spectroscopy can be applied to the study of phase transitions in materials and, for that reason, it is generally coupled at the variation of thermodynamic variables (pressure, temperature).

The use of this type of optical characterization is especially important in high-pressure studies^{77*}. In this category of experiments, the use of diamonds is particularly well suited to such characterization technique, principally because the laser and the scattering light can cross the diamond anvil cell (DAC) without difficulties.

When a substance is irradiated with monochromatic light, most of the scattered energy is comprised of the radiation of the incident frequency (Rayleigh scattering). However, a small amount of scattering is an inelastic process, thus the scattered light has a different energy from incident light. This inelastic scattering is called Raman scattering (Raman effect) and it can be classified in two ways: the fraction of photons scattered with less energy, called Stokes scattering⁸⁸ and, on the other hand, the fraction scattered with higher energy, called anti-Stokes scattering. Rayleigh scattering is the dominant process and is extremely weak (only one in every $10^6 - 10^8$ photons scatter). Figure 14 and Figure 15 shows the energy diagram of Rayleigh and Raman scattering. The incident light interacts with the molecule and distorts the cloud of electrons to form a "virtual state." This state is not stable, and the photon is immediately re-radiated as scattered light. The Raman spectrum is expressed as intensity of scattered light versus wavenumbers (which is the reciprocal of the wavelength), and this is called Raman shift (cm^{-1}).

* The use of rubies to probe the interne pressure of a diamond anvil cell will be explained in the section 1.3.1.

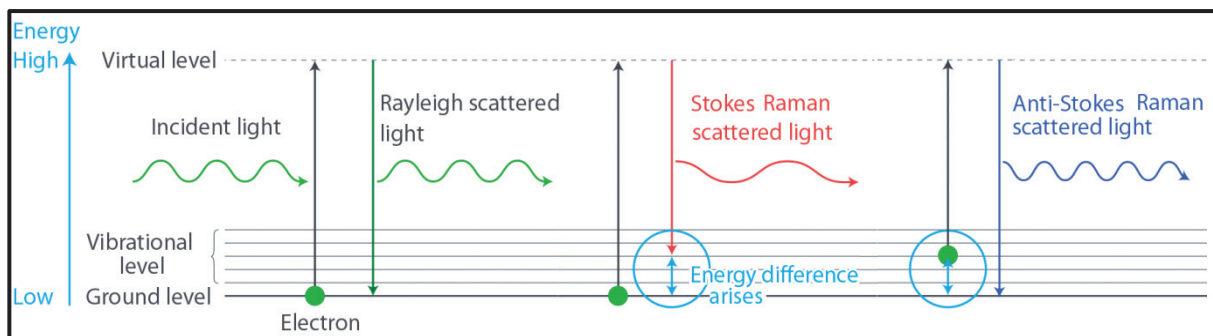


Figure 14 – Diagrams of Rayleigh and Raman scattering. Adapted from Ref.⁸⁹

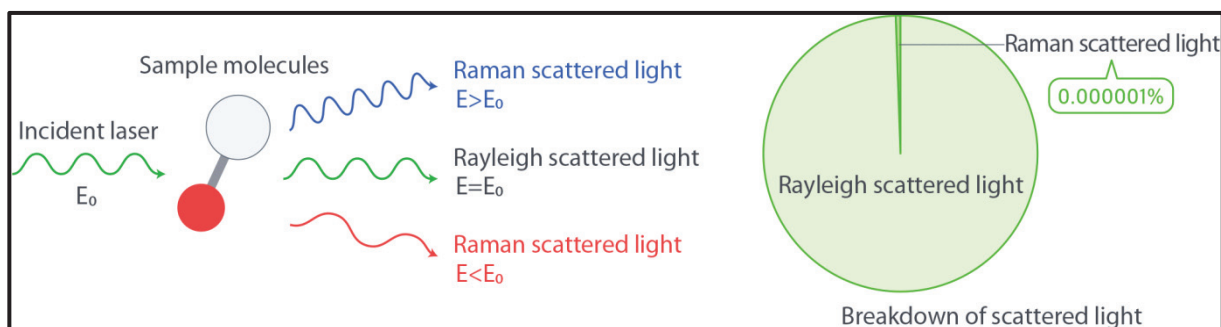


Figure 15 – Molecules scattering the light. Adapted from ref.⁸⁹

When an electromagnetic wave strikes a material, its oscillation electric field corresponds to displacements in the constituent ions, which generates moments of oscillating dipoles, which influences the electric susceptibility and, consequently, the molecular vibrations, causing a change in the polarizability. The harmonic modulation of polarization is the origin of the emission of electromagnetic radiation, just as in the case of an antenna. A more detailed explanation of the physical principles of polarization can be found in Appendix A.1.

The change in polarization that appears on Raman scattering means that intense Raman scattering occurs from symmetric vibrations, which then induces a large distortion of the electron cloud around the molecule. A peak that appears in the Raman spectrum is derived from a specific molecular vibration or lattice vibration. Peak position shows the specific vibrational mode of each molecular functional group included in the material. The same vibrational modes for each functional group present a shift in peak position due to the nearby environment surrounding the functional group, thus it is said that the Raman spectrum reflects the "molecular fingerprint" of the target.

In the crystalline structure of a material, the vibrations of the atomic lattice around their equilibrium position are distributed between the acoustic modes, the optical modes, and their combination. Raman spectroscopy particularly concerns the optical vibration modes because photons cannot transfer $\hbar k$ due to the zero mass, meaning that Raman see only optical modes at the center of Brillouin zone (Γ). These modes are easily excited by light waves due to the conservation of the pulse in the absorption process. The interaction between an electromagnetic wave crossing the crystal lattice and the vibrational or phonon modes can be analyzed both by a quantum or classical approach. These two approaches are complemented by their qualitative and quantitative descriptions of the resulting bands.

A lot of information about a material can be obtained from the Raman spectrum. As can be seen in Figure 16, not only the position but also the shape of the Raman peak is important. The width of the peak can define the level of crystallinity in the material or the particle size.

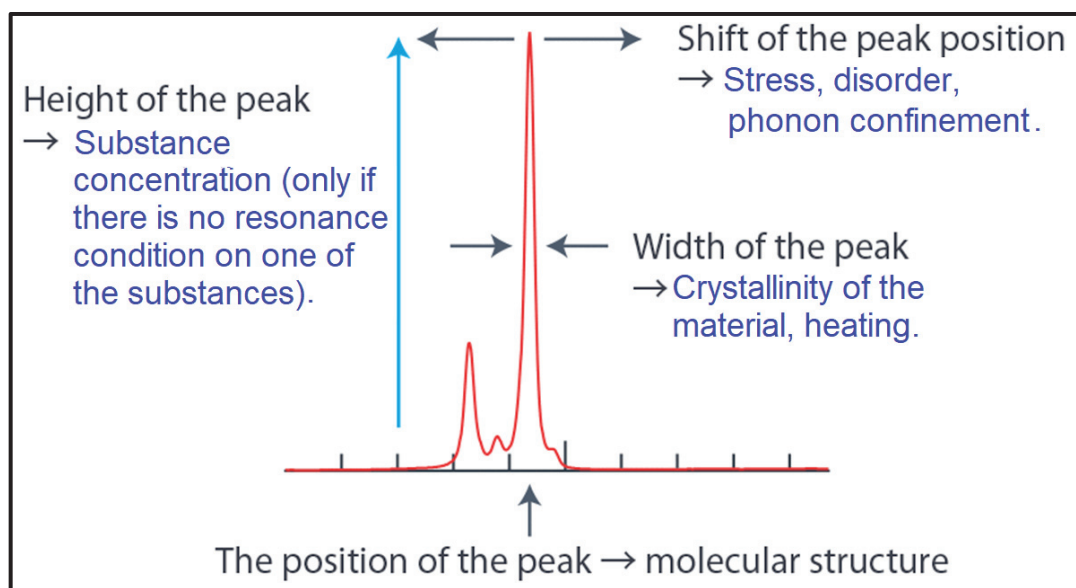


Figure 16 – Raman signal information. Adapted from ref. ⁸⁹

As an example, crystal polymorphs can be identified from subtle differences in position and by the intensity ratios of some particular peaks between them. The crystal structure of the sample becomes distorted when pressure or stress is added, allowing us to analyze the magnitude of residual stress. Using the full width at half-maximum (FWHM) of the sample peak, it is possible to track a change in the crystallinity of the sample caused by heating, stress, or pressure.

Judging from the full width half maximum (FWHM) of R-line of ruby fluorescence and the splitting between the ruby R1 and R2 fluorescence lines, it is possible to track the hydrostaticity limit of the PTM,^{90,91} *i.e.*, while the widening of R-lines and increase of R1 – R2 peak separation from high-pressure loads indicate a significant degradation of hydrostaticity.

Raman signal gives us a direct measure of the energies of the normal modes of oscillation of a medium, which in turn depend intrinsically on the interactions between the constituent atoms. Thus, the vibrational spectrum of a given material will be significantly modified when in the presence of compositional and structural changes such as atomic interference, stress effects, and quantum confinements – facts that allow Raman spectroscopy to be used to study these properties. Any residual stress inside the crystal can also be evaluated from the direction and amount of any shift of the Raman peak. So, in the case of this work, a disorder may be noticed because of the width of the peaks became larger. This characterizes a new phase or an amorphization state and the shift of the peak characterizes the stress (high-pressure) that the sample was submitted to. It is important to remark that, in the amorphous state, all the selection rules are broken,⁹² and all the phonon modes are observable. Raman is the fingerprint of the phonon DOS, in this case.

In modern assemblies, Raman spectrometers that are equipped with optical microscopes are often used to both focus an incident laser beam on the sample and collect the Raman radiation.

The Equipment and the Experiment

Our Raman spectra were obtained using a LabRAM HR Evolution Raman Spectrometer – Horiba Scientific (see Figure 17). Thanks to its ultra-low-frequency module (ULF)* it is possible to perform measurements at frequencies starting from 5 cm⁻¹ with a single monochromator stage. This specificity is very important to our

* The ultra-low frequency (ULF) module allows Raman spectroscopic information to be obtained in the sub-100cm⁻¹ region, in just a few seconds or minutes, with measurements below <10cm⁻¹ routinely available. Moreover, Stokes and anti-Stokes spectral features can be simultaneously measured, providing additional information to the user. This equipment provides important information on a range of sample types, as: pharmaceutical polymorphs; LA modes of polymer; semiconductor lattices; material phase/structure; metal halides; gases; carbon nanotubes; micro-crystallites. The low frequency modes can give detail on conformational changes, subtle changes in lattice structure and even gaseous phase bond length – parameters not easily accessible on traditional benchtop equipment.⁹³

research taking into account that the breathing modes of the nanoparticles – also called as Lamb modes (we will explain this in the next chapter) – appear only at a very low-frequency region. Low-frequency Raman scattering is actually very effective in measuring the clusters size under high-pressure. The explanation of the appearance of these modes is one of the objectives of this work.



Figure 17 – LabRAM HR Evolution Raman Spectrometer (Horiba Scientific) – Low frequencies⁹⁴

Raman limitations

There are, however, some difficulties^{95–97} inherent in Raman spectroscopy which can limit its use. Here are some of them: (i) The intensity weakness of the Raman scattering peaks with respect to the elastic scattering peak (Rayleigh) leads to technical difficulties: (a) obtaining the Raman signal at low frequency ($<100\text{ cm}^{-1}$) and (b) the low sensitivity makes it difficult to measure low concentrations of a substance. We avoided the low-frequency problem by using a spectrometer which has an ultra-low-frequency module (ULF) that allows measurements at frequencies starting from 5 cm^{-1} ; (ii) some compounds fluoresce when irradiated by the laser beam. Raman spectrum can be hidden by the fluorescence of the sample itself or of impurities; (iii) the intense laser radiation can destroy the sample by heating or can mask the Raman spectrum. Moreover, we must adjust the laser power carefully in such a way that the sample obtains maximum freedom from the fluorescence which may occur. We paid attention to their exposure time under the laser power because it can cause a modification or a deterioration.

b) Photoluminescence (PL) Spectroscopy

Photoluminescence^{87,98–100} (abbreviated as PL) is a nondestructive, non-contact method of probing the electronic structure of materials. The PL studies give important information about defects, impurities, and structure, in a material. It has been shown that when the particle size increases its efficiency also increases.⁴¹

A process called photo-excitation may happen by the following: light is shone on a sample, it is absorbed, and it generates an excess of energy generating empty (excited) levels in the material. Photo-excitation induces the electrons of the material to undergo transitions to excited states with higher energies than the states of equilibrium generating filled levels. When these electrons return to their states of equilibrium, the excess of energy is expelled from the material. The emission of light or luminescence through this process is the photoluminescence. In summary, PL is the signature of the electron transitions (excited (empty) levels and filled levels) present in a material,^{87,98} and in our case, that implies a bandgap.

Molecules, semiconductors, or insulation materials can be characterized by its optical and electronic properties such as band energy, alloy material composition, radiative surface defects such as acceptors and donors, and impurities that have internal transitions. Basically, an analysis of a material through its photoluminescence consists of the collection and analyzing of the radiation that is re-emitted by it.¹⁰¹

PL can arise from defects, but the main process is due to the exciton, at least in direct gap semiconductors. The levels of impurity and the detection of defects can be analyzed in semiconductors by their radiative transitions. Specific defects can be identified using the photoluminescence energy associated with their levels, and the amount of photoluminescence can be used to determine their concentration. In the case of our work, PL was used with the objective of detecting the level of defects of each sample:

{ None or low luminescence \Rightarrow low presence of defects
{ High luminescence \Rightarrow large number of defects* and exciton recombination in direct gap semiconductor.

* PL wavelength studies the type of the defect,^{102,103} and its position can be calculated by *ab initio* methods.

Chapter 2

Studies of SnO₂ under high-pressure – The state-of-the-art

Table of contents

Chapter 2.....	36
2.1. SnO ₂ general information.....	37
2.2. SnO ₂ bulk behavior under pressure from literature.....	39
2.3. SnO ₂ nanoparticles.....	49
2.4. SnO ₂ nanometric under pressure from the literature.....	56

In this chapter, we will talk about the physical and chemical characteristics of the SnO₂ in all its forms (single crystal, bulk, and nanoparticles) found in the literature as well as its behavior under pressure. Previous works on SnO₂ (bulk and nanoparticles) behavior under pressure (especially those in which Raman and X-ray diffraction were used) will be detailed with the objective being to support our study (which will be shown in the next chapter).

For the bulk samples, some topics of discussion will be (i) the influence of changing the pressure transmitting medium on the hydrostaticity in the experiments under pressure (ii) the effects of high-pressure on SnO₂ bulk phase transitions, and (iii) the study of the phase stability at high-pressure characterized by Brillouin and Raman spectroscopy.

For nanoparticles, the attention will be centered on the understanding of the features associated with the nanosize effect, like its behavior under pressure, the appearance of new peaks on the spectra, and the presence of low-frequency bands and extra bands when decreasing the particle size.

2.1. SnO₂ general information

The stannic oxide or tin dioxide (SnO₂) in its stoichiometric form, the SnO₂ acts as an insulator. In its pure form*, due to its oxygen-deficient form, behaves as an n-type semiconductor with a large band gap ($E_g = 3.62$ eV, at 25°C).^{57,104} Although, the conductivity is thought to be due to intrinsic defect formation, and the exact mechanism is not well understood.⁵⁷

Due to the particular electronic structure of O²⁻ (giant electron affinity of O²⁻), metal oxides are generally sub-stoichiometric in oxygen.⁴¹ Besides, SnO₂ is a good candidate for exhibiting transformations because some of its properties are strongly influenced by defects. Its properties such as particle size, crystallinity, electrical behavior, morphology, and structural behavior are intrinsically dependent on the synthesis route.⁴⁰

SnO₂ and nanostructured SnO₂ devices have always been an attractive area of study for researchers^{12,105,106} because they have a lot of optoelectronic applications and electronic properties. They can be applied in the characterization of gas sensing performances,^{105,12} transistors, catalysts,¹⁰⁷ electrode materials, electrochromic devices^{12,108} and can be used as anode material for lithium-ion.^{106,109}

As a bulk sample, the most important form of naturally occurring SnO₂ is cassiterite, which is a polymorph of SnO₂ with a tetragonal rutile structure,¹¹⁰ and it comes from the space group (SG) N°136 – P₄/mnm – D_{4h}^{14} ¹¹¹ at ambient conditions. Each unit cell contains two tin atoms and four oxygen atoms which form two sublattices. Each tin atom is at the center of six oxygen atoms located at the corners of a regular octahedron. Three tin atoms surround every oxygen atom, which is approximately at the corners of an equilateral triangle, as illustrated in Figure 18a. The two titanium ions occupy positions (0,0,0) and $(\frac{1}{2}, \frac{1}{2}, \frac{1}{2})$, and the four oxygen ions occupy positions $(u, u, 0)$, $(1-u, 1-u, 0)$ and $(\frac{1}{2} \pm u, \frac{1}{2} \mp u, \frac{1}{2})$.¹¹² The lattice parameters¹¹³ found in the literature were $a = b \cong 4,737$ Å and $c \cong 3,185$ Å. The ionic radii for O²⁻ and Sn⁴⁺ are respectively 1.40 and 0.71 Å.¹¹¹ It can be seen in Figure 18b that the oxygen sublattice has an octahedral (cubic) symmetry and, in Figure 17c, that the tin sublattice has a tetragonal symmetry. It is important to remember that a cubic symmetry is higher than a tetrahedral one, and it is easier to break a higher symmetry (cubic one) than a lower

* SnO₂ in its pure form is an intrinsic semiconductor, however its pure form is never observed naturally. Defects in oxides are generally an n-type.

one. In the case of SnO₂, when the cubic symmetry is broken, it can become a tetrahedral or an orthorhombic one.

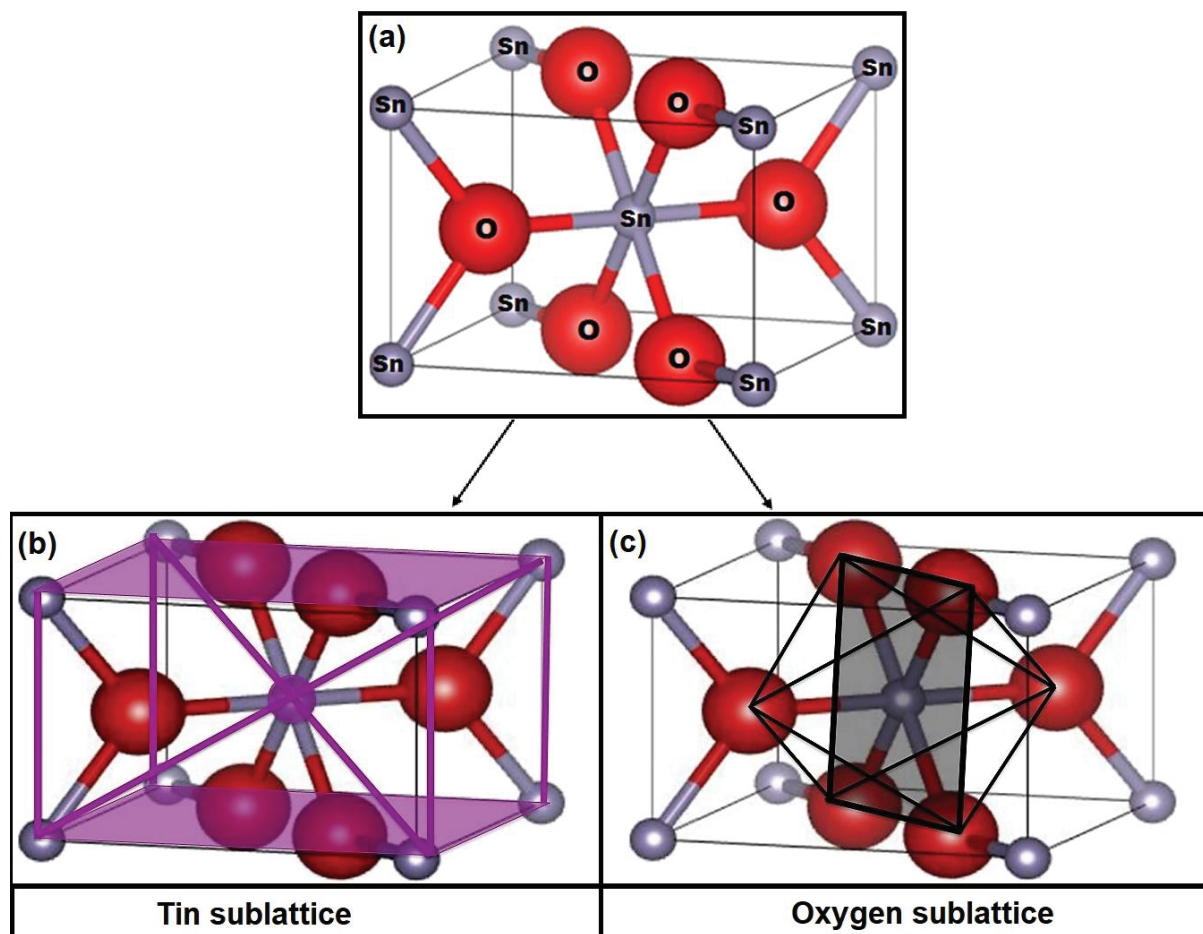


Figure 18 – (a) Scheme of SnO₂ unit cell of rutile-type structure: the large (red) circles indicate oxygen atoms and small (gray) circles indicate tin atoms. Adapted from ref.21. (b) Tin sublattice: tetragonal symmetry. (c) Oxygen sublattice: octahedron (cubic symmetry).

The vibrational representation of the normal vibration modes at the center of the Brillouin zone is given by the equation below ^{112,114,115}

$$\Gamma = A_{1g} + A_{2g} + B_{1g} + B_{2g} + E_g + A_{2u} + 2 B_{1u} + 3 E_u \quad (4)$$

Four of those modes are infrared active (A_{2u} and E_u), four modes are Raman-active (A_{1g} , B_{1g} , B_{2g} , E_g) and two are silent (A_{2g} and B_{1u}). In all Raman-active modes, the oxygen atoms vibrate while Sn atoms are at rest*. The modes A_{1g} , B_{1g} , and B_{2g} correspond to vibrations in the plane perpendicular to the c axis, while the doubly degenerated E_g mode corresponds to vibrations in the direction of the c axis. B_{1g} is a

* Raman spectroscopy sensibility is explained by the fact that only oxygen atoms vibrate in the Raman active-modes while Sn atoms are at rest.

vibrational mode related to oxygen atoms rotating around the *c* axis, with all six atoms participating in the vibration.¹¹⁶

Raman spectroscopy probes oxygen displacements, being more sensitive to this sublattice. The SnO₂ Raman-active modes¹¹² can be seen in Figure 19.

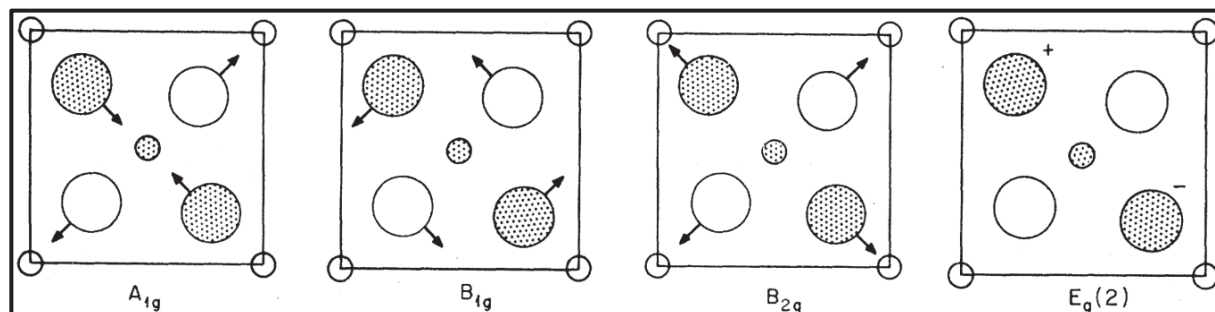


Figure 19 – SnO₂ Raman active modes. Adapted from ref.¹¹²

Raman spectra of single crystals have been reported by Katiyar¹¹⁰, Beatie *et al.*,¹¹⁷ Zuo *et al.*¹¹⁸ and Diéguez *et al.*¹¹⁹, and the positions of three of the four peaks are well characterized: $\omega(E_g) = 472 \text{ cm}^{-1}$, $\omega(A_{1g}) = 632 \text{ cm}^{-1}$, $\omega(B_{2g}) = 773 \text{ cm}^{-1}$. However, the B_{1g} mode shows surprising features. It is difficult to observe it and it is absent in several spectra reported in the literature (e.g. Ref. ¹¹⁰ and Ref. ¹¹⁷). Its position has also been a matter of discussion: Peercy¹¹⁵ reported its position at $\omega(B_{1g}) = 123 \text{ cm}^{-1}$ but other authors^{10,120} located it lying between 87 and 184 cm^{-1} .

2.2. SnO₂ bulk behavior under pressure from literature

High-pressure (HP) studies of SnO₂ have shown a transition from the rutile-to CaCl₂-type structure (SG N°58 - *Pnmm*) starting around 12 GPa.^{9,10,19} The symmetry of the CaCl₂-type structure is orthorhombic with space group *Pnmm*, which is a direct subgroup of *P4₂/mnm*. This direct group-subgroup relationship indicates a possible second-order ferroelastic phase transition driven by the softening of the B_{1g} phonon mode.^{10,20,121,122} According to Haines *et al.*,¹²¹ depending on the degree of hydrostaticity, a small amount of α -PbO₂-type (SG N°60 – *Pbcn*) phase might appear. At pressure above 21 GPa, a cubic phase has been reported and two different structures were proposed to describe this phase: (i) a pyrite type (SG N°205 – *Pa $\bar{3}$*) or

(ii) a fluorite-type (SG N°225 – Fm $\bar{3}$ m).^{121,123}

It is important to highlight that a lot of experimental constraints and nature of phase transition will influence the experimental phase transition pressure in this group of compounds. So, a complementary *ab-initio* DFT calculation is quite significant.

It is also important to know that exists a difference between pyrite-type (Pa $\bar{3}$) and fluorite-type (Fm $\bar{3}$ m) phases, as can be seen in Figure 20. Such a difference arises from a modification of the oxygen positions and, in both structures, the cations form an “fcc” sublattice. The oxygen atoms in the fluorite structure lie on Wyckoff sites 8c (u, u, u) with $u = 0.25$, whereas in Pa $\bar{3}$ structure $u \approx 0.345$.⁸ This difference in anion position results in the coordination polyhedron being a rhombohedral rather than a cube as in the fluorite structure.

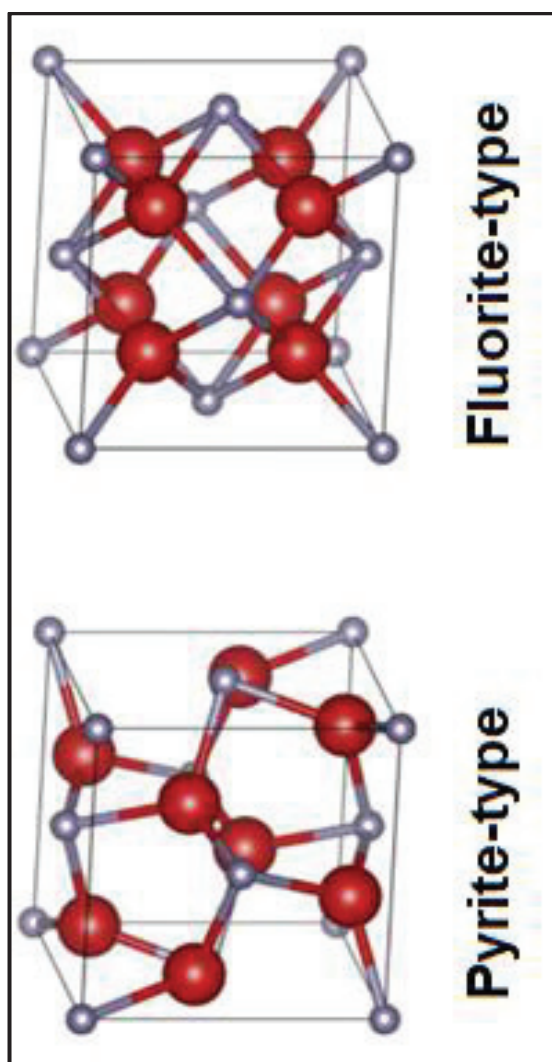


Figure 20 – SnO₂ pyrite-type and fluorite-type structures. Adapted from ref.21.

The behavior of SnO₂ bulk using XRD under pressure^{19,121,124} can be synthesized by the schema see in Figure 21.

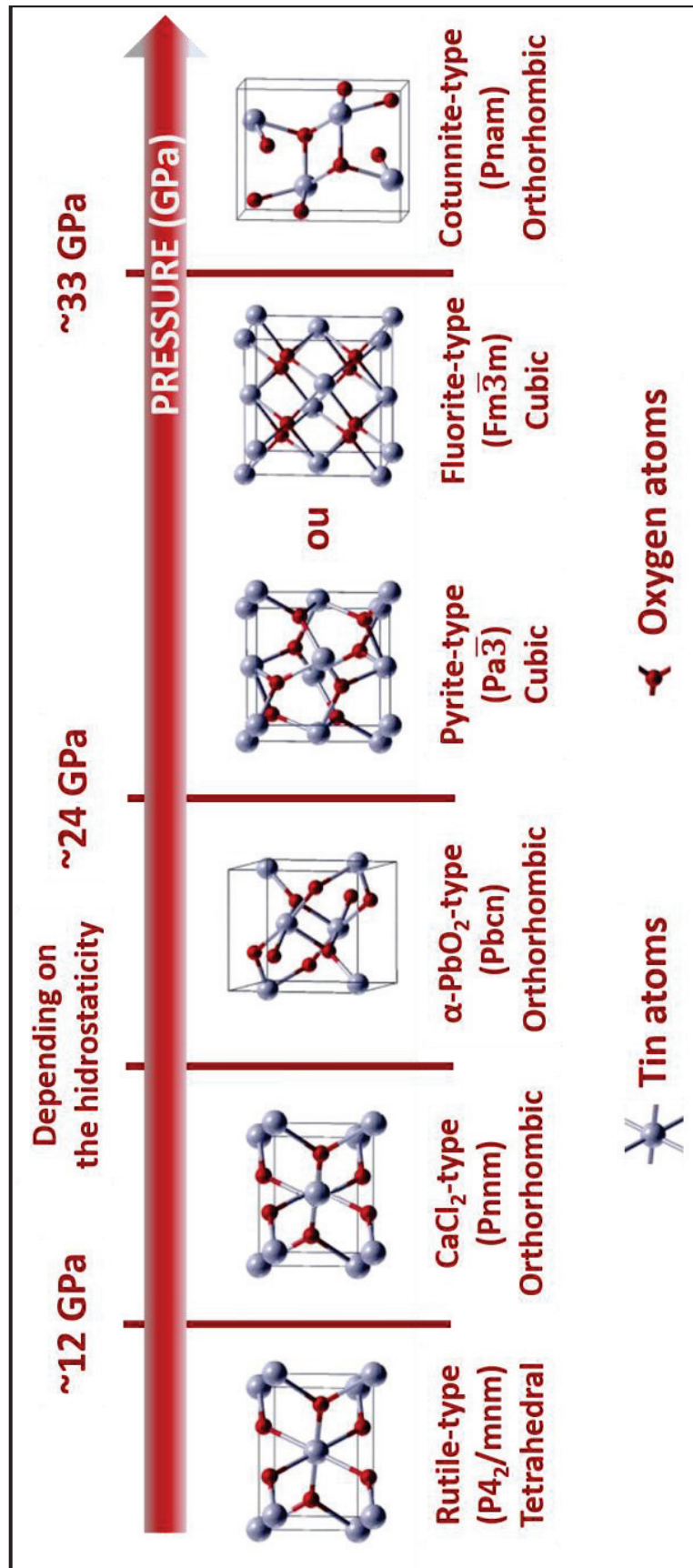
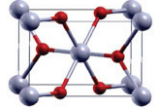
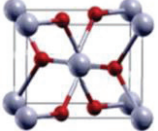
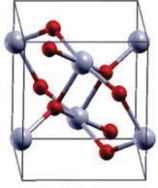
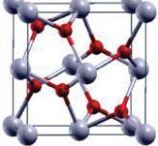
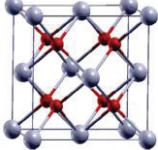
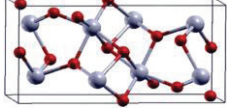
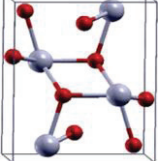


Figure 21 – SnO₂ bulk behavior in the literature using XRD. Adapted from ref¹²⁴.

For the following, SnO₂ polymorphs will be labeled according to the corresponding names given in Table 1.

Table 1 – Structural information about SnO₂ polymorphs.

Phase	Space group number	Structure type	Space group	Lattice system	Point group (Schönflies Notation)	Scheme of the structures by the ref. ¹²⁴
Phase I	136	Rutile-type	P4 ₂ /mnm	Tetragonal	D_{4h}^{14}	
Phase II	58	CaCl ₂ -type	Pnm	Orthorhombic	D_{2h}^{12}	
Phase III	60	α-PbO ₂ -type	Pbcn	Orthorhombic	D_{2h}^{14}	
Phase IV	205	Pyrite-type (modified fluorite)	Pa $\bar{3}$	Cubic	T_h^6	
Phase V	225	Fluorite-type	Fm $\bar{3}$ m	Cubic	O_h^5	
Phase VI	61	ZrO ₂ -type	Pbca	Orthorhombic	D_{2h}^{15}	
Phase VII	62	Cotunnite-type	Pnam / Pnma	Orthorhombic	D_{2h}^{16}	

Haines and Léger⁹ investigated SnO₂ pressures up to 49 GPa by angle-dispersive X-ray diffraction using an imaging plate. They started the experiment using silicone grease as a pressure transmitting medium (PTM) however in this run the refinement using P4₂/mnm structure was no longer satisfactory at 5.0 GPa. Thus, the effect of stress on this phase transition was investigated with a second run performed using 16:3:1 methanol: ethanol: water as the PTM. The transition of rutile-type (phase I) to CaCl₂-type (phase II) was detected at 12.6 GPa on compression, but the extrapolation of the high-pressure gives a transition pressure of 11.8 GPa. The

extrapolation of the spontaneous strain data obtained using the silicone grease medium yields a transition pressure of 4.7 GPa, suggesting that this ferroelastic transition is very sensitive to non-hydrostatic stress.

Two new reflections in the experiment were observed starting at 12.6 GPa using silicone grease. At 12.6 GPa, based on the intensities of the new reflections, approximately 1% of the sample had transformed to another phase, α -PbO₂-type (phase III). The proportion of this phase increased very gradually with subsequent increases in pressure, arriving at a maximum of 15% at 19 GPa in the compression run.

Both phases II and III began to transform into Pa $\bar{3}$ -type* (phase IV), above 21 GPa at ambient temperature. The kinetics of the II \rightarrow IV transitions are very slow at room temperature and with the intention of obtaining the maximum conversion to phase IV, the sample was heated for several hours at many different pressures between 24 and 48 GPa. At pressure above 42 GPa, 75% of the sample is composed by Pa $\bar{3}$ phase. This percentage increased to 84% at 48 GPa and the residual material was in phase II.

Upon decompression at ambient conditions, retransformation has been observed, and the sample recovered. It consisted of a mixture of the rutile-type and α -PbO₂-type phases. At 11.5 GPa, the percentage of phase II increased to 19%, and 9.2 GPa, the percentage of phase II had further increased to 28%. In addition, 18% of the sample had transformed to phase III. The proportions of these two phases continued to increase at the expense of phase IV with further decreases in pressure. The sample recovered at ambient conditions, and it consisted of a phase I and phase III, with almost the same quantities. The absence of preferred orientation was observed in either phase.

It is important to emphasize that Haines and Léger assumed in their studies that for ethanol: methanol: water mixture as the PTM, the conditions are hydrostatic up to 15.5 GPa. However, current studies^{73,128} show that for such PTM the hydrostaticity conditions only go up to 10.5 GPa. It is also important to clarify that they use silicon grease as the PTM for the experiment on non-hydrostatic conditions because their coefficient of hydrostaticity is very low, only going up to 0.9 GPa. The nominal

* There is a discussion concerned to such phase. Liu¹²⁵ and Endo *et al.*¹²⁶ assumed that such cubic phase was a fluorite-structured. Posteriorly, He *et al.*¹²⁷ had the same interpretation.

'hydrostatic limit' of PTM was defined as being the pressure at which a back extrapolation of the peak widths achieves the value observed in the hydrostatic regime.

Shieh *et al.*¹⁹ used X-ray diffraction to study the high-pressure and temperature influences on SnO₂ bulk. Argon was used as the PTM and as thermal insulation, and the existence of four phase transitions up to 117 GPa were shown. They observed the sequence of phases for SnO₂: rutile-type (phase I) → CaCl₂-type (phase II) → pyrite-type (phase IV) → ZrO₂ orthorhombic phase I (phase VI) → cotunnite-type (Phase VII). The pressure in the sample was gradually increased to 74 GPa at room temperature. In the compression, three phase transitions were detected by X-ray diffraction: Phase I → Phase II → Phase IV.

Using the Le Bail Method to do the refinements, they could identify the rutile phase at 9.9 GPa, but it could not exclude the possibility of the appearance of a minor amount of CaCl₂-type phase due to the broadening of the (211) peak. However, they only confirmed the existence of the CaCl₂-type modification at 13.6 GPa. The peaks from the phase II continued up to 50 GPa during room-temperature compression. With additional compression up to 28.8 GPa, they observed changes in the diffraction pattern, and Le Bail method of refinement indicated that such a pattern consisted of CaCl₂-type and pyrite-type phase coexistence. No sign of phase III was detected in such a study. At 50 GPa, they saw that some peaks of the pyrite-type phase were divided, indicating the appearance of another phase an orthorhombic I phase (*Pbca*) of ZrO₂ (phase VI). At 74 GPa, the sample was heated at 1200–1500 K for 8 min while X-ray data was collected, and after cooling, there was a change in the diffraction pattern which matched as being a cotunnite-type structure (phase VII). At the highest pressure, the experiment ended abruptly because the diamond broke during the heating process. A vestigial peak vanished when the pressure was augmented above 80 GPa. This was the first time that ZrO₂-type and cotunnite-type phase were reported at pressures greater than 50 GPa.

Hellwig *et al.*¹⁰, in order to clarify the structural mechanism of the rutile-to-CaCl₂ transition and to obtain more insights into the stability of the phases at higher pressures, performed, Brillouin and Raman spectroscopy on SnO₂ up to 13 and 30 GPa at ambient temperature, respectively. The transition from the rutile-type to the CaCl₂-type structure was observed starting at 14.8 GPa, and the transformation seemed complete at 15.3 GPa. The powder samples started to transform to phase III

at about 30 GPa. This phase was retained upon decreasing the pressure.

Figure 22(a) shows the Raman spectra at 14.2 GPa in the rutile-type structure and at 15.6 GPa in the CaCl₂-type structure. Figure 22(b) presents the dependence of Raman frequencies through pressure for the rutile-to-CaCl₂-type transition. The fitted peaks also display the data points. They are, within experimental errors, in good concordance comparing researches conducted below 0.4 GPa and with researches at higher pressures but without detecting the soft mode.³ The dashed line marks the phase transition and the solid lines, for the soft mode above the transition, mark the fit to the powder data.

It is important to remark that Hellwig *et al.*¹⁰ estimated that the phase transition from rutile-to-CaCl₂-type structure happened at 14.8 GPa. However, the previous works^{9,19,129} assumed that such kind of transformation happened at ~12 GPa, so it is questionable if at 14.8 GPa the phase transition (phase I → phase II) has not yet occurred.

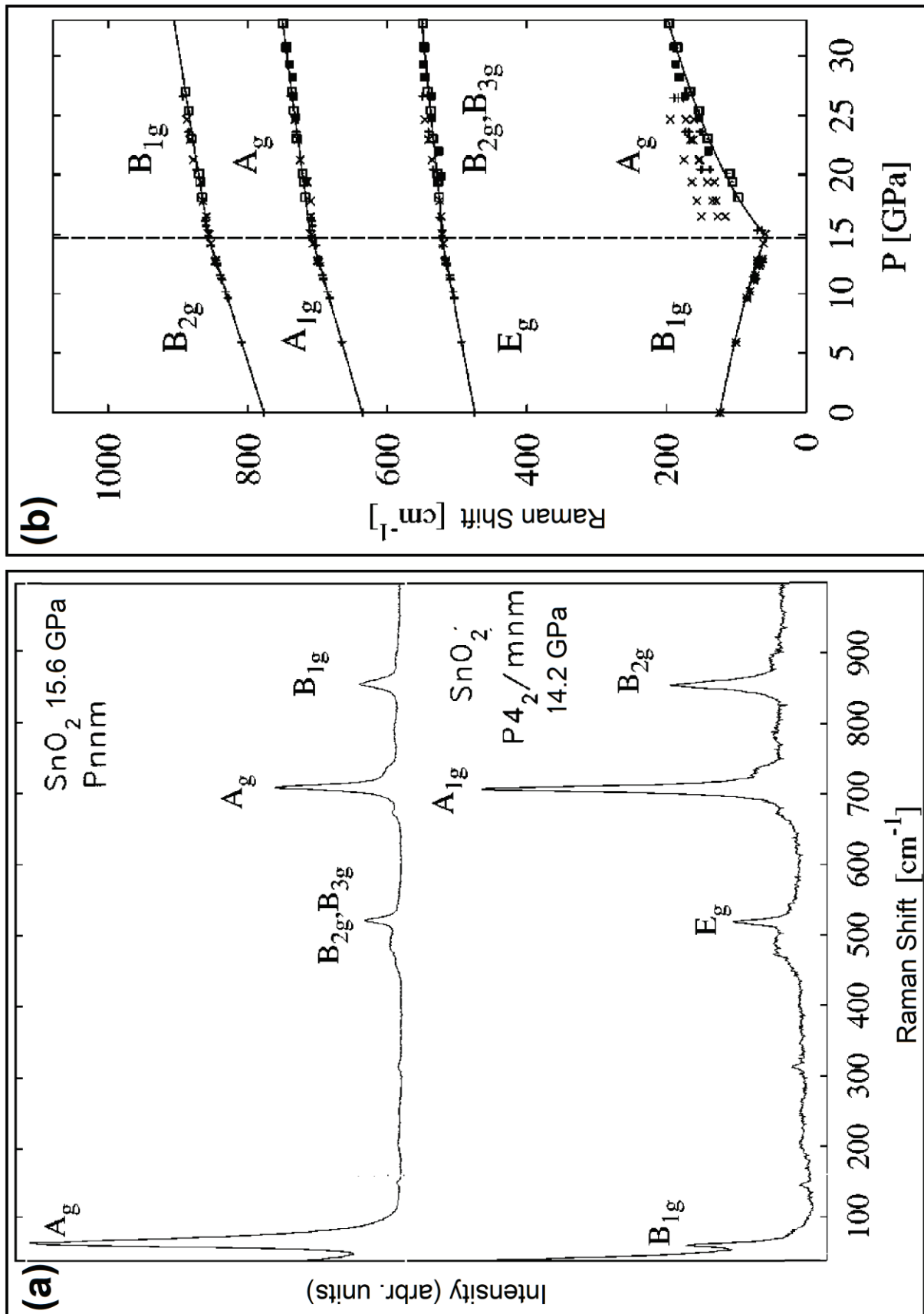


Figure 22 – (a)(Down) Raman spectrum at 14.2 GPa in the rutile-type structure. (Up) Raman spectrum at 15.6 GPa in the CaCl₂-type structure. (b) Pressure dependence of Raman frequencies through the rutile-to-CaCl₂-type transition. Legend: (x): single crystal data on increasing (decreasing) pressure; (□): powder data on increasing (decreasing) pressure. (*): soft mode frequencies from single-crystal samples, not temperature annealed.²¹ Adapted from ref. 10

Gupta *et al.*,¹²⁹ in order to study the effects of the pressure on SnO₂ lattice dynamical properties, used density functional perturbation theory (DFT) to perform a first principle calculation of the lattice dynamical properties of rutile SnO₂ using, at ambient and high-pressure conditions. Their goal was to better understand the pressure-induced phase transition from the calculation, at high pressure, of the full-phonon dispersion curves (PDC) and phonon density of states (p-DOS) compared to Raman intensities. In order to understand the changes that occurred in the phonon spectrum of rutile SnO₂ at high pressure and using first principles calculations within density functional theoretical formulations, they could calculate the full PDC along with the total p-DOS at several pressures, up to 20 GPa. It is important to know that, contrary to the conventional behavior seen for other Raman-active phonon modes (in the case of rutile dioxides), the frequency of Raman active mode B_{1g} (the lowest optical branch) will decrease, since the pressure increases. The softening of such Raman mode indicates a structural instability, which is the precursor of phase transition. Figure 23(a) and 23(b) allow us to illustrate the p-DOS and DFT calculations.

With such study, they confirmed the ferroelastic transition from the rutile to the CaCl₂-type structure. Additionally, they showed that such first transition appears from the strong coupling between elastic constants and softening of Raman active B_{1g} mode.

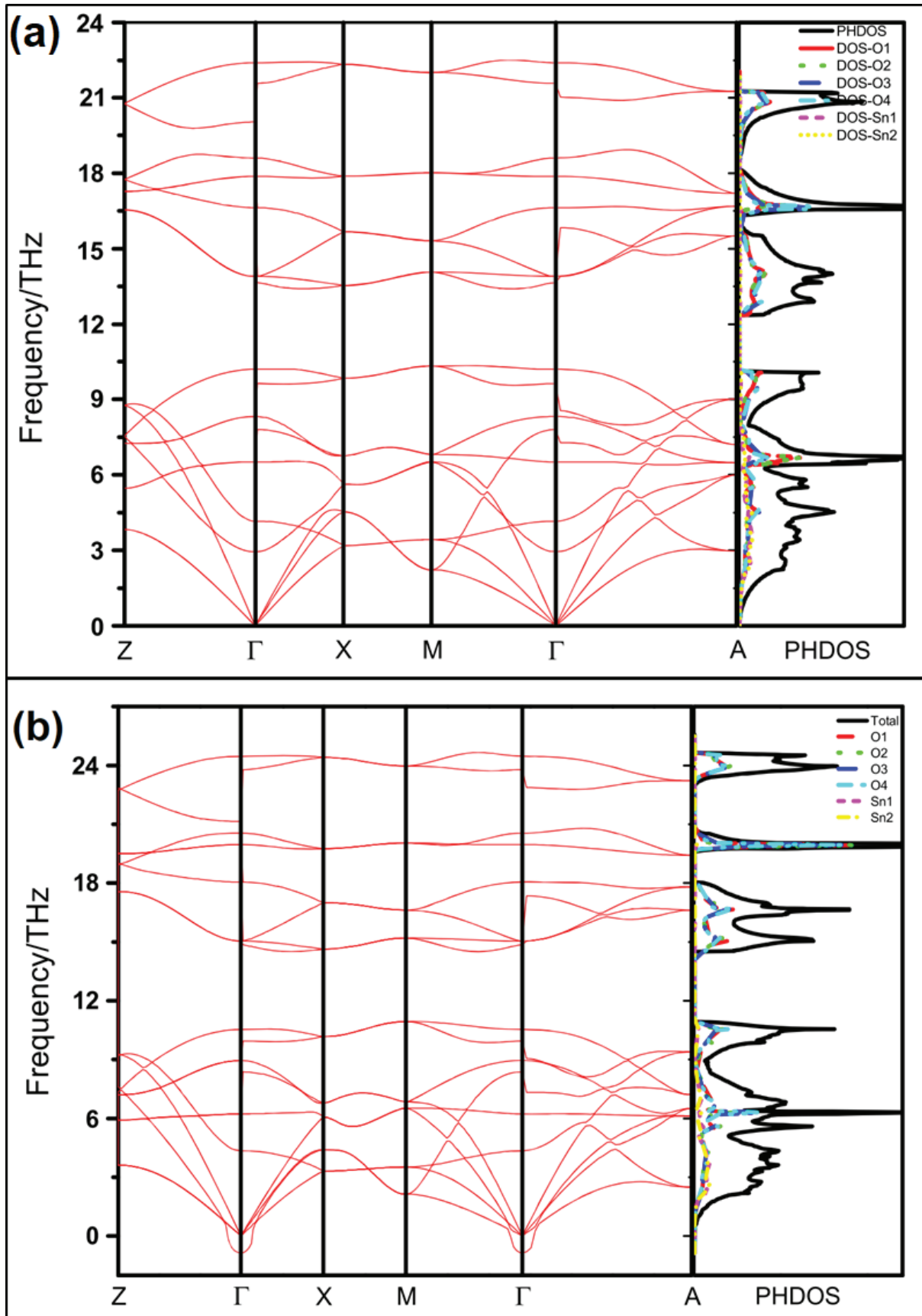


Figure 23 – Phonons dispersion curves and phonon density of states of SnO₂ (a) in rutile phase at ambient pressure. (b) in rutile phase at transition pressure (12GPa).

2.3. SnO₂ nanoparticles

Semiconductor nanoparticles have been widely studied for their phase stability against pressure due to their technological importance. SnO₂ is one example of rare materials in which optical transparency and conductivity coexist⁵⁵ in bulks¹³⁰ and in nanoparticles.^{131–133} Thus, one example of such property is that SnO₂ nanoparticles are used in dye-sensitized solar cells as a photoanode.¹³ Electro-catalytic and photocatalytic characteristics are important for organic oxidation process, self-cleaning surfaces, and anti-microbial systems.^{134,135}

In SnO₂ nanocrystals, the initial structure is also a rutile-type. However, it is not clear if, under high-pressure, the CaCl₂-type phase is present, as the broadening of the diffraction peaks due to the nanoparticle size prevents us from observing the subtle changes in the diffraction patterns associated with such phase transition.¹³⁶ Otherwise, a recent study¹³⁷ with a micron-size X-ray beam spot on 30 nm-diameter particles confirmed the existence of a second-order phase transition. Meanwhile, the transformation to the cubic phase was observed in all studies.

Figure 24 and Figure 25 shows the Raman spectra changes when the particle size is reduced.^{138,139} The understanding of the features associated with nanosize effect have been studied^{11,112,114,139} in particular by Diéguez *et al.*^{11,116}

In these both figures, we can note a broadening and a shift of the classical modes of SnO₂, which is apparently in agreement with a spatial correlation model.

On the one hand, the spectra of the Figure 24 present two main bands (P1 and P2) that grow with the proportion of surface atoms in the high-frequency region of the spectrum.¹³⁸ On the other hand, the spectra of the Figure 25 were fitted using the Peakfit software and they show nine bands from sample F to sample B. Due to its very small particles size, sample A presents a different behavior and some of its bands which appeared before, will disappear. The weak Raman bands 3 and 8, seem to correspond to IR-active LO and TO modes, and it seems reasonable to assign these volume modes to IR-modes whose Raman activity is induced by disorder. Bands 2 and 5 are extremely weak; they are still present in sample B, but both of them have disappeared in the sample A, and these modes could correspond to the LO–TO E_u IR-active modes. The frequency of the volume modes 1, 4, and 10 systematically decreases with the size. This can be interpreted based on a tensile state which should

develop progressively in the bulk of crystallites when their surface contribution increases. Modes 7 and 9 were identified as surface modes and it involves z displacements of atoms (see Fig. 3 in ref ¹¹²) and correspond to ending coordinates.

Many reasons have been invoked to explain the appearance of new peaks and the broadening of existing ones when the particle size decreases: surface modes, phonon confinement models, surface stresses and disorder-induced breaking of selection rules. ^{118,138,139} Additionally, they are interpreted based on surface modes* and are related to the effects of the defect. ^{11,139,140}

* Surface modes are due to the existence of a lattice relaxation which takes place on the outside of the grain, like a disordered skin around each grain. ^{41,119}

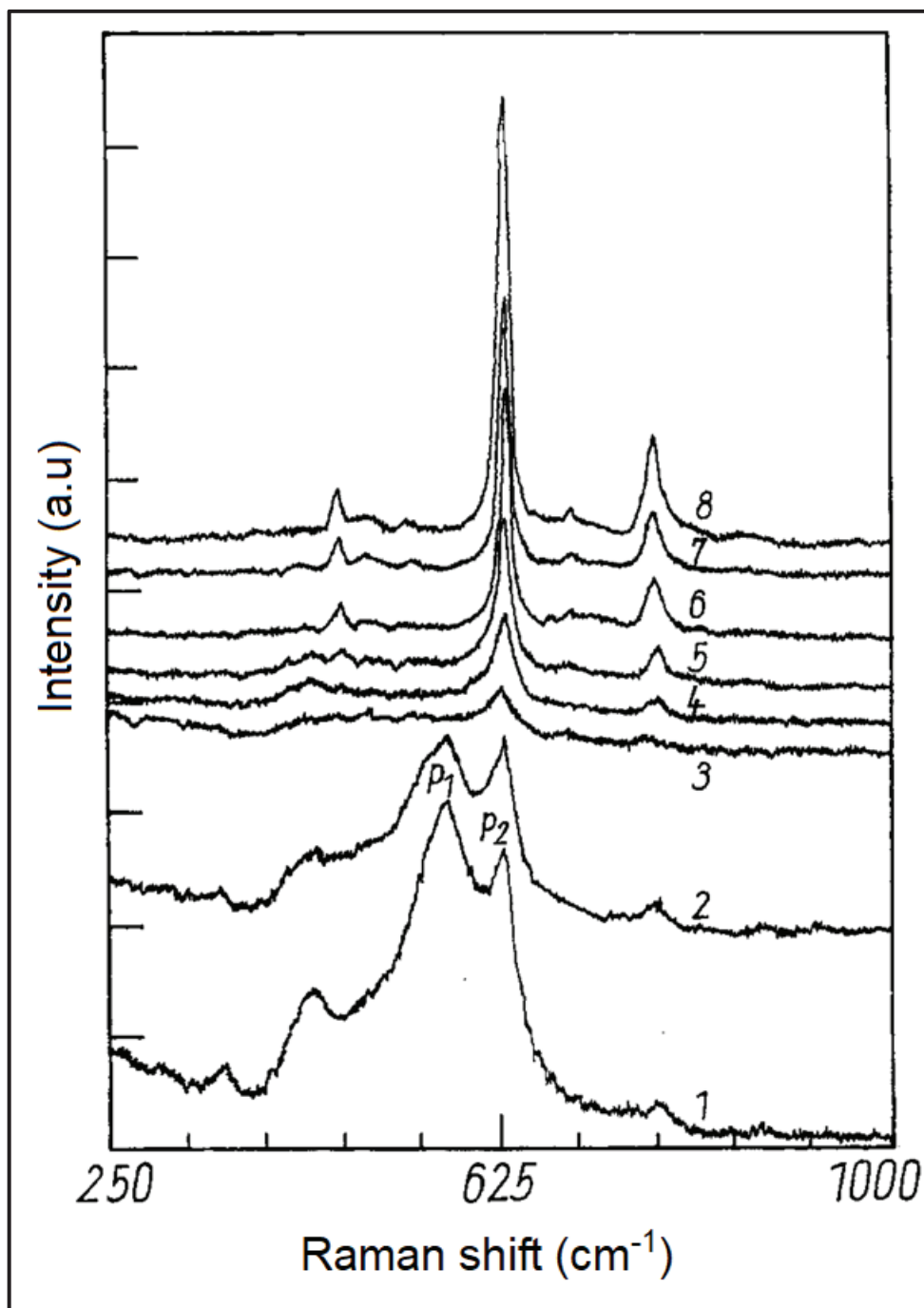


Figure 24 – Raman spectra of nano-SnO₂, specimens heat-treated at different temperatures and of a coarse-grained specimen.¹³⁹

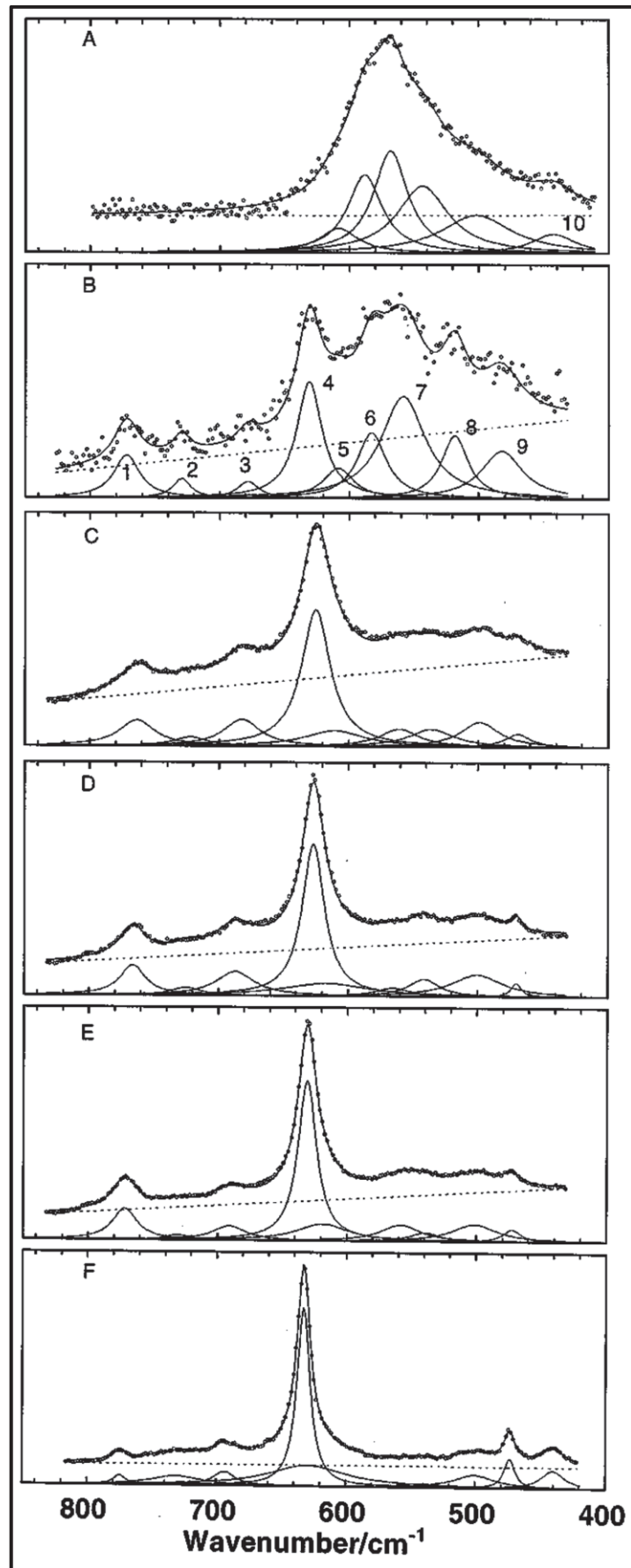


Figure 25 – Raman spectra for five powder samples recorded at 25 °C as presented by Abello et al. The components representative of volume modes (nine bands – F to B samples and Band 10 on A sample) were defined from the single-crystal data and from spectra of a natural cassiterite sample with a large concentration of defects.¹³⁸

Diéguez et al.¹¹⁶ observed low-frequency bands in SnO₂, and this can be seen in Figure 26. They showed in their experiments that the Raman spectra depend on the temperature at which the oxide originally obtained was calcined, *i.e.*, it depends on the nanoparticle size. Analyzing these nanoparticles (ranging from 3 to 100 nm), they realized that disorder and nanoparticle size have a strong influence on the vibrational properties of this oxide. When the particle size decreases, the bands associated with the classical modes of SnO₂ shift and broaden in relation to dispersion curves. When the grain size decreases, two new bands appear in the high-frequency region and according to the authors,¹¹⁶ those are due to a surface layer of SnO₂ nonstoichiometric with a different symmetry than SnO₂.

When fitting the bands which appear in the high-frequency region of the Raman spectrum, there are some extra bands in the region between 475 and 775 cm⁻¹ (S1, S2, and S3 in Figure 27) which will appear ensued of disorder activation. The intensity and the position of these bands also depend on the size of nanoparticles. The presence of oxygen vacancies¹⁴¹ gives rise to a nonstoichiometric SnO_x at the surface, and this could be responsible for producing bands S1 and S2. In the case of S3 band, it can be attributed to disorder activation of the A_{2U} IR active and Raman forbidden mode.¹³⁸

They also showed that the appearance of a low-frequency band associated with acoustic modes depends on the grain size. Such band which shift toward higher wave numbers are less intense, and it broadens as the average nanoparticle size decreases.

When considering the nanoparticle as an elastic body of spherical shape, two types of vibrational modes are derived: the spheroidal and the torsional ones. The spheroidal mode is a vibration with dilatation and it is derived from the scalar and vector potentials. Its eigenvalues depend on the material through the ratio v_l/v_t , where v_l and v_t are the longitudinal and transversal sound velocities, respectively. Conversely, the torsional mode is a vibration without dilatation and does not depend on the material because it is derived only from the vector potential.

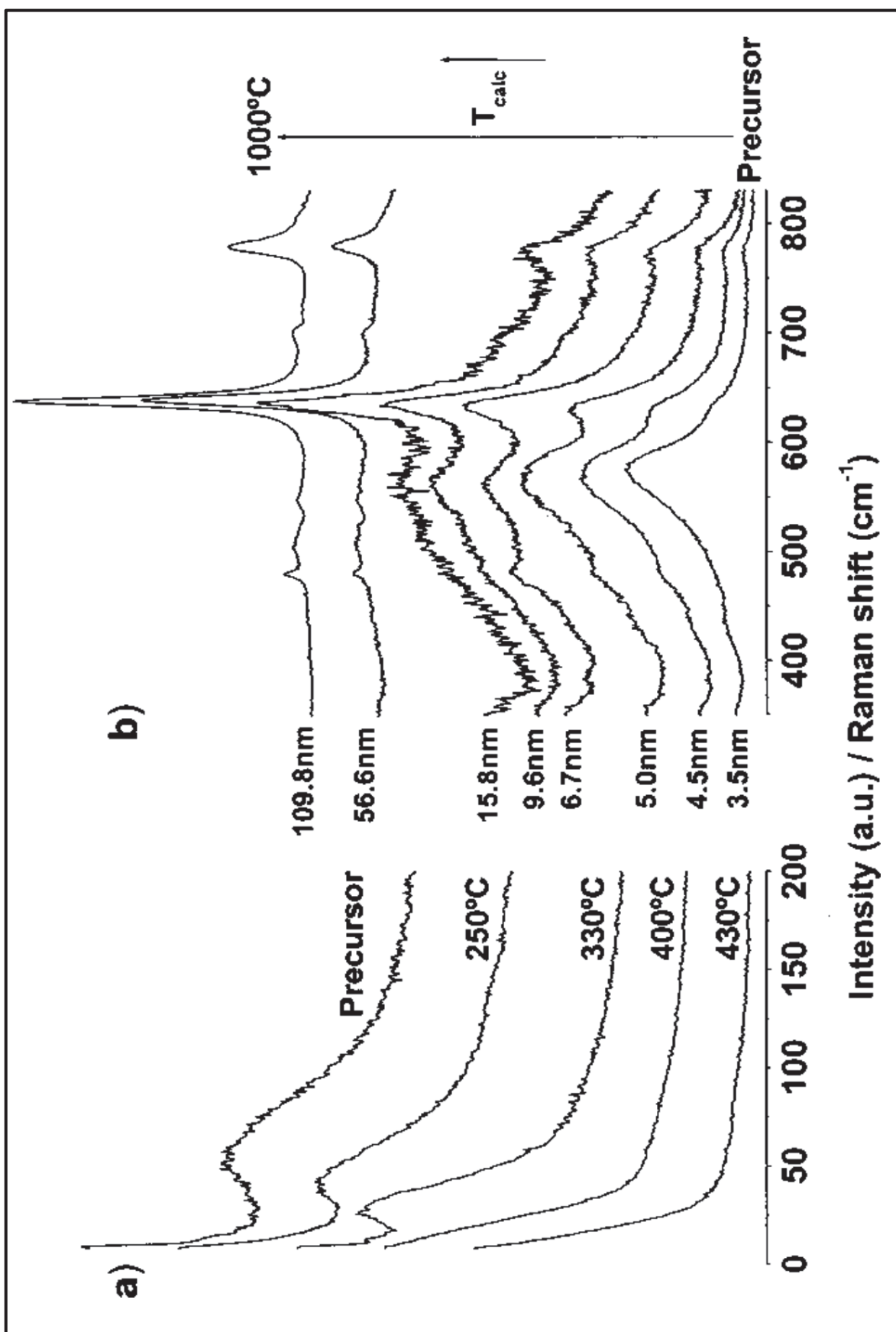


Figure 26 – Raman spectra of the powders calcined up to 1000 °C for 8 h. The spectra have been divided into: (a) the low-frequency region and (b) the high-frequency region. The spectra in the high-frequency region correspond, from bottom to top, to the uncalcined powder and the powders calcined at 250, 330, 400, 430, 450, 800, and 1000°C for 8 h. Additional features were not observed outside these regions. ¹¹⁶

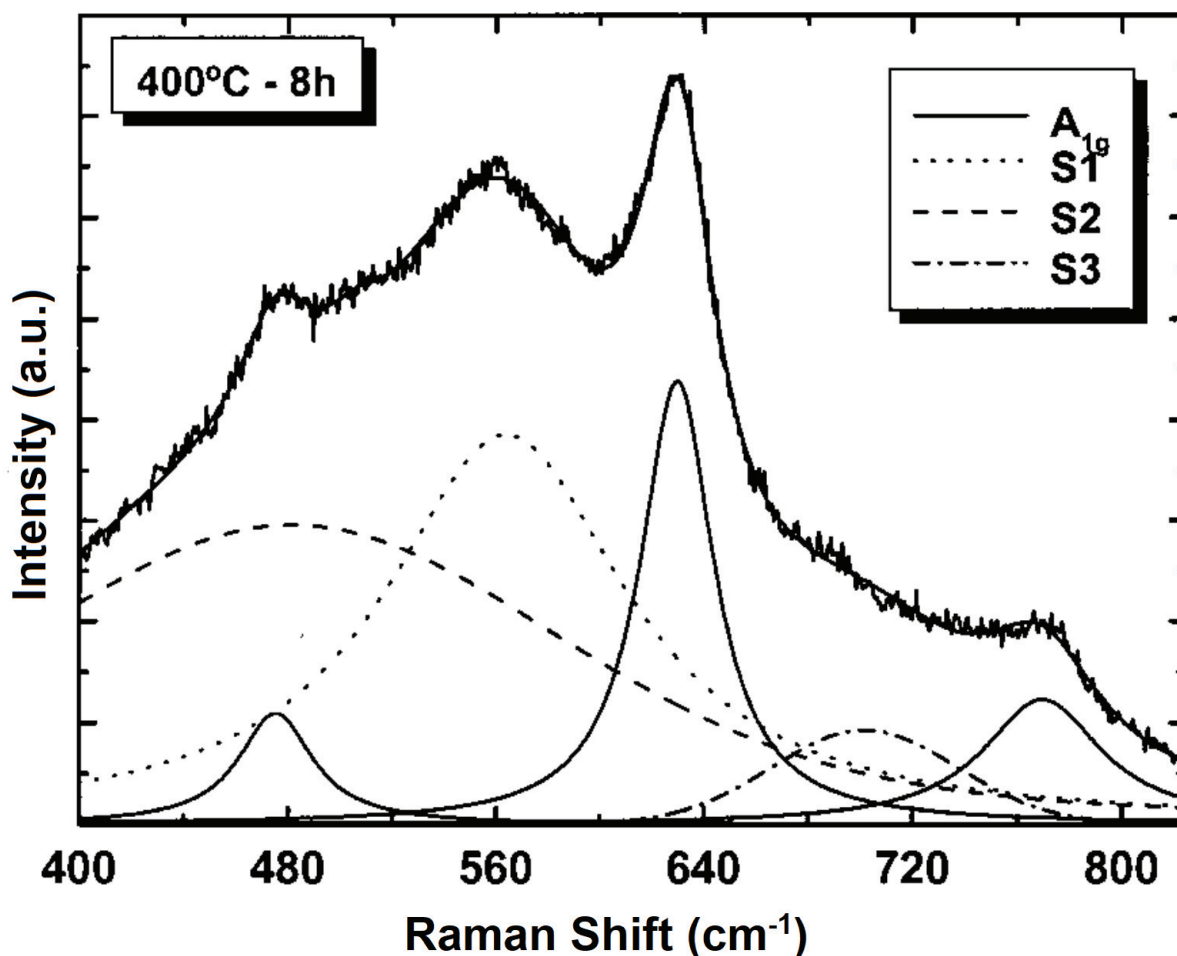


Figure 27 – Fitting of the bands appearing in the high-frequency region of the Raman spectrum of SnO₂ powder of very small grain size. The bands peaking at 634, 568, 486, and 706 cm⁻¹ correspond to A_{1g} mode and bands S1, S2 and S3, respectively. Modes B_{2g}, peaking at ~776 cm⁻¹, and E_g, peaking at 480 cm⁻¹, are also included in the fitting.¹¹⁶

Only the spheroidal mode with $l = 0$ is perfectly symmetric and that only the Raman scattering of such mode is expected to be perfectly polarized (all other modes are partially depolarized). Such behavior based the experimental discrimination of the stress-free boundary condition. So, we expect to observe the spheroidal modes with $l = 0$ in parallel polarizations uniquely, whereas the $l = 2$ ellipsoidal mode should be observed both for parallel and perpendicular polarizations.¹⁴² So, the experimental data were coherent with the rigid boundary condition and $l = 2$ when considering that no changes in the shape of the spectra were detected by using HH or HV polarizations. Then, after considering the “rigid” boundary conditions, one^{143,144} arrives at expressions for estimating the frequency of the vibration as a function of the particle according to Lamb’s conditions (see Appendix A.2.).

2.4. SnO₂ nanometric under pressure from the literature

Nanomaterials may present different physical behavior in comparison to the same material arranged in bulk form. Besides particle sizes,^{128,145,146} these different behaviors depend as well on the nanostructure morphologies.^{147–149} Such differences are discussed during the compression process and in terms of the transition pressure (P_t). However, in HP experiments, the interaction between the nanocrystals and the PTM and the capability of nanoparticles to aggregate cannot be ignored.¹⁵⁰ In addition, due to interface energy effect, the transition pressure^{26,151,152} is expected to be higher in nanocrystals.

The behavior of SnO₂ nanometric under pressure (depending on the particle size) can be synthesized by the schema seen in Figure 28.

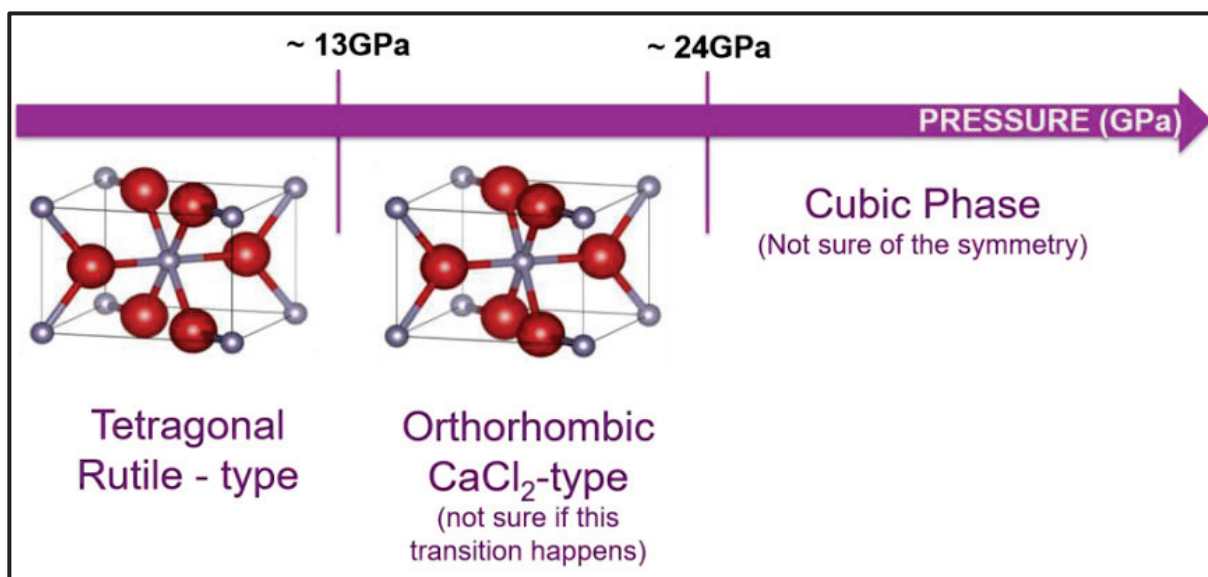


Figure 28 – SnO₂ nanoparticles behavior under pressure. Adapted from ref.¹³⁷

An important study comparing physical properties of bulk and nanomaterials was realized by He *et al.*¹²⁷ They studied the behaviors of SnO₂-bulk (99.95% on average grain size of 5 μm) and nanocrystals (with average grain size of 3, 8, and 14 nm) samples by *in situ* high-pressure synchrotron radiation X-ray diffraction measurements up to about 40 GPa, at ambient temperature using methanol: ethanol: water (16:3:1) as the PTM. They found that the transition pressure increased with a decrease in the particle size. For a 3 nm particle diameter, no transformation to the cubic phase could be observed, even at pressures as high as 39 GPa. In the same study, for 8 nm and 14 nm particles, the transition pressures are 29 ± 2 GPa and 30 ± 2 GPa, respectively. It is worth noting that, in addition to the shift of the transition

pressures, the pressure domain is large, and in all cases, the low-pressure phase (rutile-type) persists up to ~40 GPa.

Figure 29 shows the XRD patterns of bulk and nanocrystalline SnO₂ samples at ambient conditions, for such a study. It was shown that the onset transition pressures for the rutile-to-cubic phase transition were: (i) SnO₂ Bulk: 23±2 GPa; (ii) SnO₂ 14 nm at 29 ± 2 GPa; (iii) SnO₂ 8 nm: 30 ± 2 GPa. They did not detect the cubic phase for the 3 nm nanocrystalline SnO₂ samples, but they have estimated it. This can also be seen in Figure 29, marked as vertical lines that show the possible positions for the peak of the cubic phase of these XRD patterns. In their experiments, they just observed the transition from rutile-to-cubic phase because only a small concentration of α-PbO₂-type phase was formed. They also found that when the size of the SnO₂ nanocrystal decreases, the transition pressure for the rutile-to-cubic phase transformation becomes higher. Thus, such an increase of the transition pressure is caused principally due to the surface energy differences between the rutile and the cubic phases when the SnO₂ crystallite size gets smaller, as is explained below by Zuo *et al.*¹¹⁸

Zuo *et al.*¹¹⁸ showed that when dealing with nanometer SnO₂ with small grain size (*i. e.* when the particle size decreases) some features are observed. By one hand, there are some peaks which are initially present in the Raman spectra of single-crystal and polycrystalline SnO₂, and since the particle size decreases, their intensity diminishes (we will call these peaks as A group peaks). By the other hand, two new peaks (here called B group peaks) grows when the particle size become smaller.

With a decrease in crystal size the number of superficial atoms increases rapidly, whereas the number of interior atoms decreases swiftly. So, the scattering intensity from surface phonons will increase while the scattering intensity from interior phonons will decrease gradually. The B group peaks are explained by the surface phonon modes and they are closely related to the A group. Additionally, the Raman shifts of the B group are smaller than that of the A peaks, respectively. This is evidence that the lowering of surface phonon frequencies is caused by decrease of the superficial force constant. This decrease can lead to an increase in the interatomic distance sin surface layers as compared to those in the interior of samples.

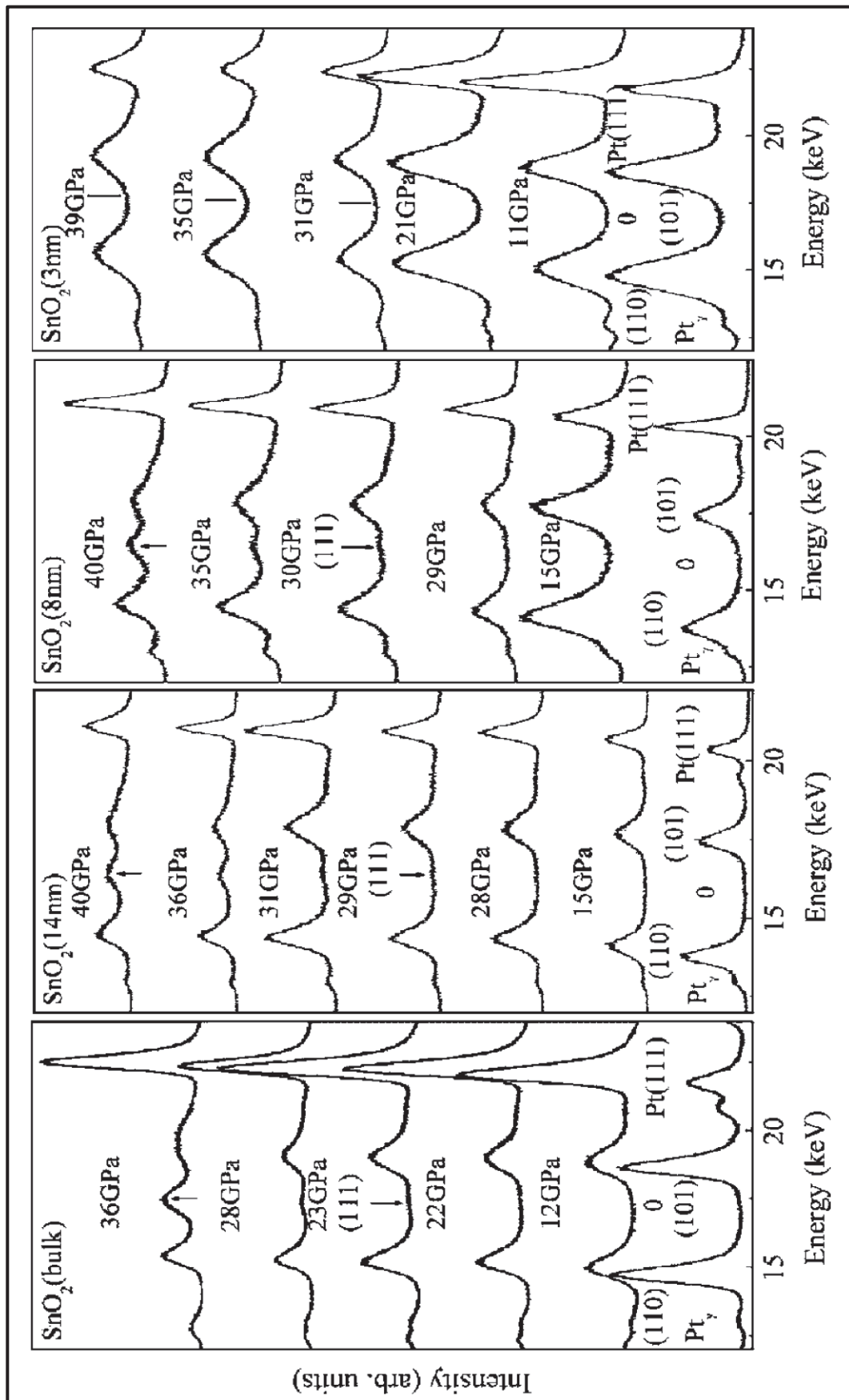


Figure 29 – Room temperature synchrotron radiation energy-dispersive X-ray diffraction patterns recorded at various pressures for bulk, 14 nm, 8 nm, and 3 nm SnO₂ samples. The appearance of the peak of the cubic phase is marked with an arrow. The vertical lines in the XRD patterns for the 3 nm SnO₂ sample mark the possible positions for the peak of the cubic phase.¹²⁷

In a similar experiment, Alka B. Garg¹⁵³ prepared SnO₂ nanocrystals by the chemical precipitation method, with an average grain size of 5 nm up to 34 GPa, also at ambient temperature.

All the diffraction peaks from these samples can be related to rutile structure at low pressure. Upon increasing pressure, no visible changes in the diffraction patterns could be observed except that of the shifting of peaks to a higher angle due to lattice compression. This tendency towards stability was observed up to 18 GPa. Conversely, the diffraction pattern acquired at 18.9 GPa showed a weak diffraction peak appearing between the strong (110) and (101) peaks of the rutile structure, indicating the onset of a structural phase transition (eventually CaCl₂-type to cubic). Upon further compression of the sample, the diffraction peaks related to the rutile-phase decreased their intensity whereas the peaks from the new phase increases in intensity. However, the width of the transition was large, while the phases still coexist at pressures of ~33GPa. The coexistence of both phases (ambient and HP phases) was observed until the highest pressure investigated and after the complete pressure release, the high-pressure daughter phase was retained (Figure 30).

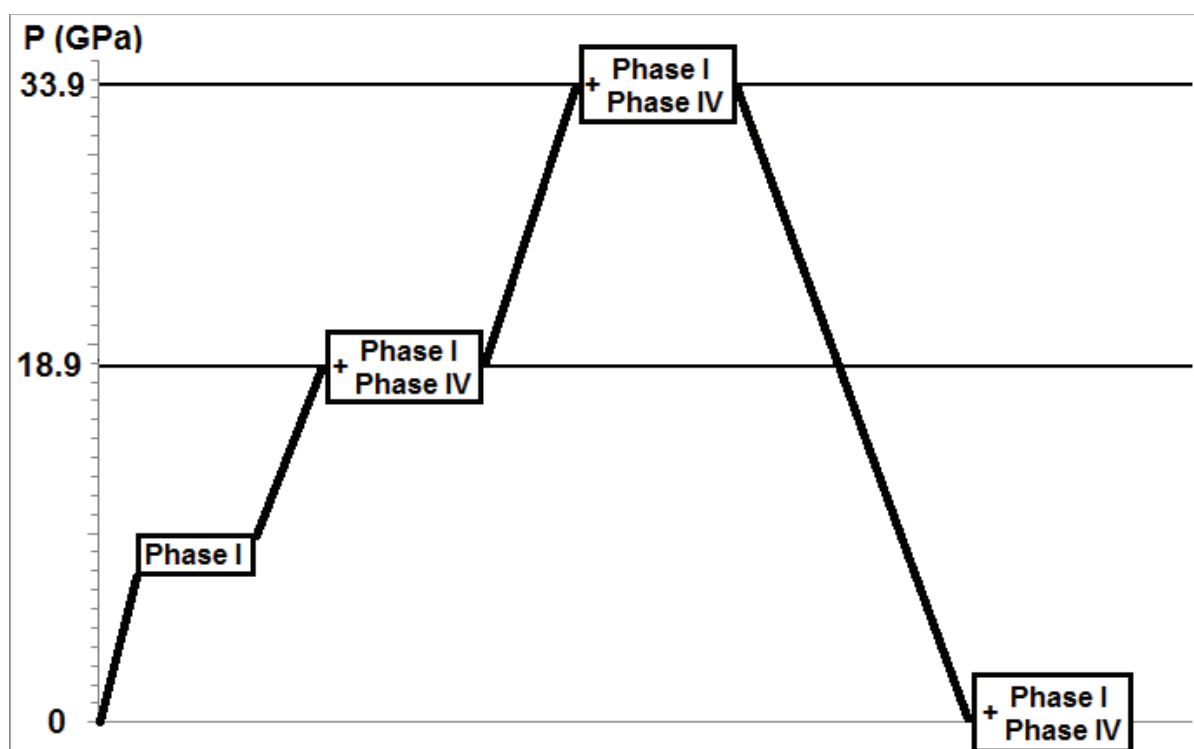


Figure 30 – Schema for Garg's study of SnO₂ nanoparticles (~5nm) transition phase

In this study, considering that, at ambient pressure, XRD peaks are very broad due to nanometer-sized particles, no extra visible broadening is detected, and it is very difficult (almost impossible) to observe this phase. The absence of an extra peak left

to (110) reflection of a rutile phase excludes the possibility of rutile to an α -PbO₂-phase transformation. In addition, the fact that the transition to α -PbO₂-phase is very slow and the data collection time at a synchrotron is low, the fact of not detecting this phase in the current studies is not very surprising. Other high-pressure studies⁹ reported that heating is necessary in order to get a sufficient amount of α -PbO₂-phase under high-pressure. Upon decompression, the high-pressure phase may be retained, but sometimes the α -PbO₂ is stabilized during the decompression path.¹⁵⁴ One of these previous studies¹⁵⁵ reported Raman spectra under pressure, but it was inconclusive because of the strong fluorescence background and the weak signal made it difficult to complete a proper analysis.

Comparing the rutile-to-cubic-type phase transition patterns obtained by both Haines and Léger⁹ and Garg¹⁵³, it can be concluded that the space group “Pa $\bar{3}$ ” related to the position of the new reflections observed by Garg was incorrectly associated with “fluorite-type phase”, while the correct space group for this structure is actually “Fm $\bar{3}m$ ”.

Recently, Grinblat *et al.*²¹ studied the structural behavior of undoped tin dioxide nanoparticles up to 32.2 GPa by using synchrotron X-ray diffraction experiments under high-pressure. A series of twenty-three different pressure measurements were done between 0.4 and 32.2 GPa.

Contrary to Garg’s and other works^{8,9}, they did not observe any coexistence during the transition of rutile-to-CaCl₂-type phase. They explained that their results were expected for a second-order transformation, and they emphasized the importance of using a micro-sized X-ray beam. They reinforced this point of view by explaining that in previous studies, an unfocused X-ray beam was used, and it mapped the whole pressure chamber. Due to the presence of radial pressure gradients within the DAC, two phases, corresponding to parts of the sample under different pressures, were observed; *i.e.* the large X-ray beam was mapping portions of the sample at different pressures, detecting in this way two different phases near P_t . Then they explained that such a drawback has been overcome in their experiments by using a micron-size X-ray beam.²¹

So, from ambient pressure up to 13 GPa, they only found the low-pressure rutile-type phase in the pure SnO₂ sample. But at 14.6 GPa they detected changes in the XRD pattern evidencing the transition to the CaCl₂-type structure. From 14.6 to

21.5 GPa, only this phase is present. However, they also observed that at 24.4 GPa, additional changes take place in the XRD pattern and they identified a transition to a cubic HP phase.

From 24.4 to 32.2 GPa (the highest pressure achieved in the experiment), the CaCl₂-type and cubic phases coexist (from Rietveld refinements the phase fraction of the cubic phase is 20% at 24.4 GPa, reaching a 60% at 32.2 GPa). As shown by Garg's experiment with 5 nm nanoparticles, the transition to the cubic structure is not fully reversible, and what is recovered after decompression is a mixture of rutile and cubic phases. As in Garg's¹⁵³ research, no evidence of α -PbO₂ structure found in bulk SnO₂ by was found in Grinblat *et al.*²¹ experiments.

For Grinblat *et al.*²¹ it was impossible to determine whether the cubic phase found was the pyrite-type or the fluorite-type. This fact can be explained because in the angular range of their experiments appeared three reflections on the pyrite structure which are absent from the fluorite structure, and these ones, which were expected to appear at 12.13%, 13.29%, 16.30% at 24.4 GPa where, unfortunately, expected to be very weak, and the positions predicted for them overlap with Bragg peaks of the CaCl₂-type phase and that of Cu.

Chapter 3

SnO₂ powders and single crystal under high-pressure

Table of contents

Chapter 3	62
3.1. Introduction	63
3.2. The characterization methods	64
3.2.1. The characterization at ambient pressure	64
a) <i>X-ray Diffraction (XRD)</i>	64
b) <i>Photoluminescence (PL) Spectroscopy</i>	67
c) <i>Raman spectroscopy</i>	69
3.2.2. Characterization at high-pressure	71
a) <i>Raman Spectroscopy</i>	71
b) <i>First-principles calculations</i>	81
3.3. Discussion	84

In this chapter, we will talk about the behavior of SnO₂ powders and single crystal under the high-pressure. The pressure-induced changes are shown to be strongly dependent on the morphology of the samples. The single crystal was studied up to ~ 23 GPa and the commercial powders were studied up to ~ 28 GPa both using Raman spectroscopy. Four different set of experiments were done under pressure: single-crystal with PTM, Merck powder with and without PTM, and Aldrich powder with PTM. The Single crystal exhibit phase transitions as reported in the literature whereas powder samples show a disordering of the oxygen sublattice in the first steps of the compression. The observed differences will be discussed based on the density of defects and interpreted in the framework of the theory of invasive percolation.

3.1. Introduction

Stannic oxide powders and single crystals have been studied under high-pressure using X-ray diffraction^{19,121,126,156,157}, Raman spectroscopy,^{3,115,122} and *ab initio* simulations.^{124,129,158,159}

Only a few works^{3,10,115} reports the study of SnO₂ crystal at high-pressure by using optical spectroscopy. The work the most representative work was the reported by Hellwig *et al.*¹⁰ which combined Brillouin and Raman spectroscopy. Such work studies the single crystal under pressure and it shows that the rutile to CaCl₂-type transformation occurs at ~ 14.8 GPa through a ferroelastic transition. Such transformation is driven by the softening of the B_{1g} mode, corresponding to the collective displacement of O atoms.^{8,10,129}

In all these studies on SnO₂ bulk, no sign of amorphization or disordering has been reported. On the one hand, a high-pressure study using X-ray diffraction (which is mainly sensitive to the cationic sublattice) was conducted at pressures up to 30 GPa¹²⁷ did not show any transformation in a sample that contains particles of 3 nm. On the other hand, a recent high-pressure study on nanoparticles¹⁶⁰ using Raman spectroscopy (which probes the oxygen sublattice) demonstrates that some pressure-induced disordering occurs at around 14 GPa. This study underlined the interest of combining experimental techniques to obtain a complete picture of the structural evolution.

A very important information that must be retained is linked to the vibrational modes of the rutile structure. In such structure, only the oxygen atoms are involved in the Raman-active vibrational modes.¹⁶¹ Thus, this characteristic makes this system adapted to the studies in which happens the decoupling of the sublattice.

At this part of the work, we used three different samples. The two first samples (~ 5 μm each one), in powder form, were obtained commercially, one by Aldrich (purity > 99.99%) and the other by Merck (purity > 99.0%) companies. The third one was a natural non-oriented single-crystal (~150 μm), from Viloco Mine in Bolivia, which was obtained collaboratively with the mineralogy collections of ENS Lyon – École Normale Supérieure de Lyon and UCBL – Université Claude Bernard Lyon1. In the next sections, I will explain and detail the experimental procedure steps and discuss the results.

3.2. The characterization methods

3.2.1. The characterization at ambient pressure

The samples were characterized in order to allow us to explain the different evolutions under pressure. These characterizations were based on its physical and chemical qualities. We characterized the structural phase by X-ray diffraction, the density of defects by photoluminescence and by Raman. They will be detail in the next subsections.

a) X-ray Diffraction (XRD)

The X-ray diffractions of the two micro-powder samples (Aldrich and Merck) were held at the Henri Longchambon Diffractometry Center (CDHL – Centre de Diffractométrie Henri Longchambon).

Our XRD experiments at ambient pressure were performed using a Bruker D8 Advance Bragg-Brentano diffractometer (see Figure 31). This device has a lamp (excitation source) which uses copper $K\alpha_{1,2}$ lines at 0.15406 nm. In our experiments, we used an incidence angle of 0.4 degrees to maximize the surface contribution, knowing that this is the limit of such apparatus. In addition, this diffractometer is provided of a linear detector called LynnEye XE which uses a divergence source variable (4 mm). We used a step of 0.02° with each step of 19.2s, and a 2 θ scan varying between 5 and 70 degrees (see schema in Figure 32).

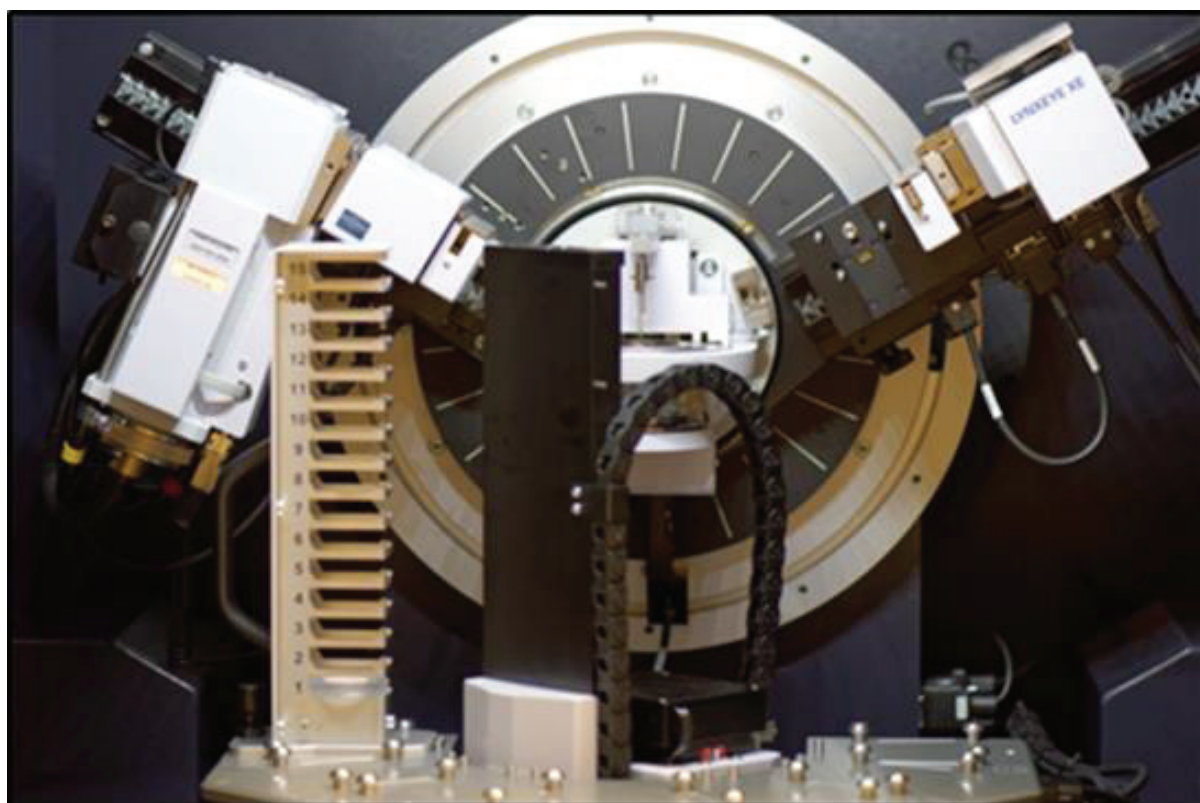


Figure 31 – Bruker D8 Advance Diffractometer ¹⁶²

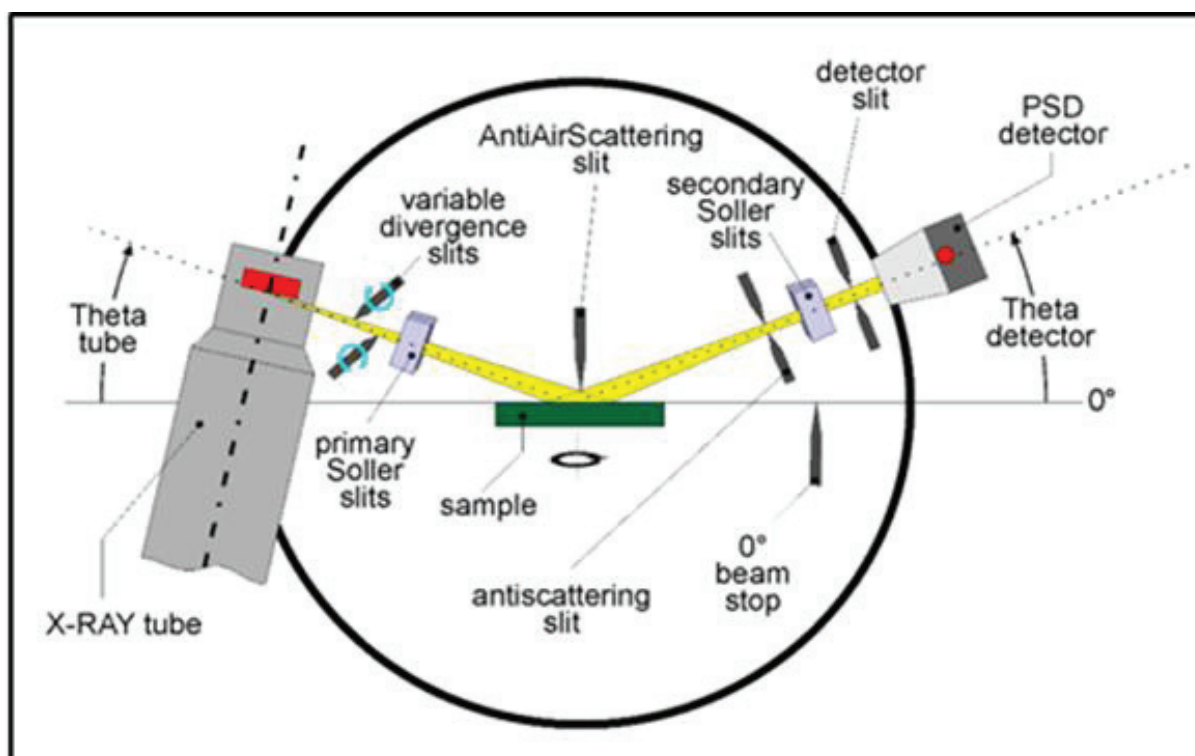


Figure 32 – Bruker D8 Advance diffractometer diagram operating in Bragg Brentano configuration. A copper anticathode produces the radiation. ¹⁶²

After the experiment, we recognized the phases using the data basis of PDF – 4+ (ICDD) via DIFFRAC.EVA program, distributed by Bruker AXS. Based on the results shown in Figure 33 below, we concluded that both samples are microcrystalline, and the initial phase structure corresponds to the rutile-type with no additional phase.

In the case of the SnO₂ single-crystal sample, we did not perform X-ray diffraction on it. We found that it was not necessary because its Raman spectrum presented similar peaks to those of the SnO₂ powder samples, with three main peaks corresponding to the first-order spectrum – confirming the presence of rutile-type phase.

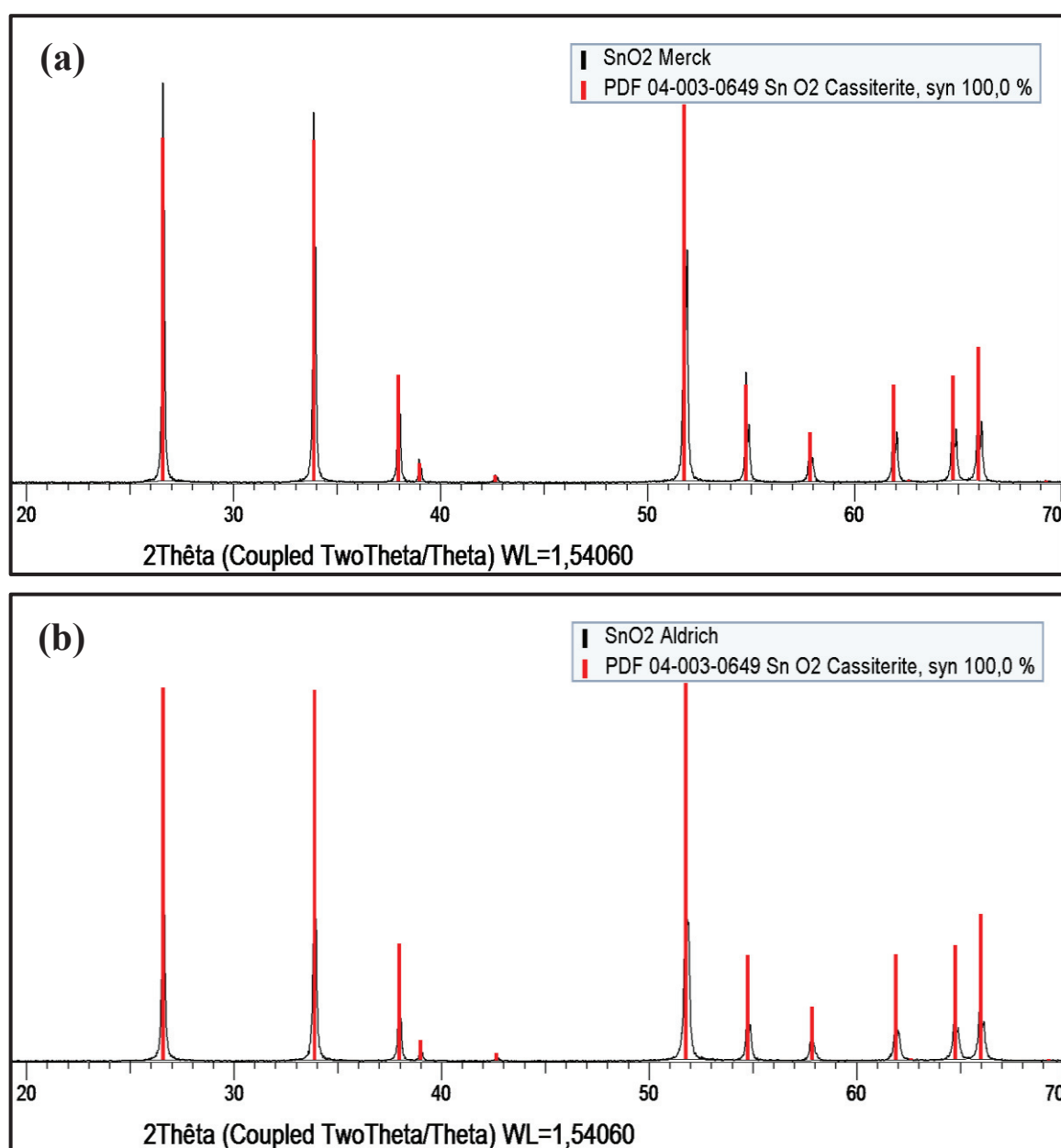


Figure 33 – X-ray diffraction patterns for (a) Merck powder sample; and (b) Aldrich powder sample. Both are indexed in the rutile-type (cassiterite) structure with no additional phase. The red bars are related to the recognition of the phases which were carried out on the data basis of PDF -4+ (ICDD).

In addition to the use of DIFFRAC.EVA program to perform the phases recognition, the X-ray diffraction patterns were analyzed using a Le Bail refinement using the Fullprof software. The cell parameters obtained from this procedure are in very good agreement with parameters from the literature that gives $a = 4.7380(1)$ and $c = 3.1865(2)$ ¹⁶³ and that are characteristic of high-crystallinity SnO₂.

The table below shows the unit-cell parameters (a, c), R_p (profile R-factor) and R_{wp} (weighted profile R-factor) factors obtained from Le Bail refinement of the X-ray diffraction patterns of both Aldrich and Merck powder samples.

Table 2 – Unit-cell parameters (a, c), R_p and R_{wp} factors obtained from Le Bail refinement of the X-ray diffraction patterns of both Aldrich and Merck powder samples.

Sample	Aldrich	Merck
Cell parameters	$a = 4.739 (2)$	$a = 4.739 (1)$
	$c = 3.187 (2)$	$c = 3.187 (2)$
R_p (%)	8.34	9.27
R_{wp} (%)	14.9	14.5

b) Photoluminescence (PL) Spectroscopy

The photoluminescence is an efficient technique to probe the defect density by reflecting the existence of defects creating an electronic state in the bandgap. Additionally, in the literature we can find some *ab initio* calculations giving the position of the level associated to a specific defect, which helps to determine the origin of the disordering. According to a lot of studies,^{164–167} several radiative deexcitation paths are possible all involving oxygen vacancies, either in bulk or at the surface or even in O-H superficial groups. Bonu *et al.*¹⁰² reported the existence of two types of ‘O’ vacancies in the SnO₂ crystal which are: bridging ‘O’ (O^B) and in-plane ‘O’ (O^P) vacancies. They showed that such defects were found to play an essential role in the detection of CH₄ gas at low temperatures.

Our PL experiments were carried out using a Crylas UV laser, which emits a continuous radiation of 10 mW at 266 nm (4.66 eV). The PL emissions from our samples were collected at room temperature by an optical fiber, dispersed by an i-HR 320 Jobin-Yvon spectrometer (600 grooves/mm rating blazed at 500 nm) and registered by a liquid N₂ cooled Si CCD camera.

Figure 34 shows the photoluminescence spectra obtained for our three samples, at ambient pressure. Analyzing such results, we had some difficulty to assign the peak positions, however, it is visible that the single crystal shows a low emission efficiency, *i.e.* a lower radiative defect concentration. Such lower defect concentration is still more accentuated in comparison to the powder samples (Aldrich and Merck) that contain mainly oxygen vacancies defects. It is clear that Aldrich and Merck powders show different luminescence bands, and this is due to the different types of the defects¹⁰³ present in each sample.

A strong peak at ~ 600 nm (*i.e.* 2.06 eV – yellow luminescence) can be perceived on Aldrich powder and it can be ascribed to the O^B vacancies. On Merck powder, the peak which appears at ~ 550 nm (2.25 eV – green luminescence) is less intense than that one seen on Aldrich sample, and it can be attributed to the defect states created by the O^P vacancies. Additionally, these emissions are principally due to the energy states introduced in the band gap due to defects, such as (i) dangling bonds, and (ii) tin interstitials.^{41,111,114,168} They are present with considerable density on the SnO₂ grain boundaries and, generally, they perform as radiative centers in luminescence processes, creating an electronic state in the bandgap, trapping electrons from the valence band to make a contribution to the luminescence.¹⁶⁹

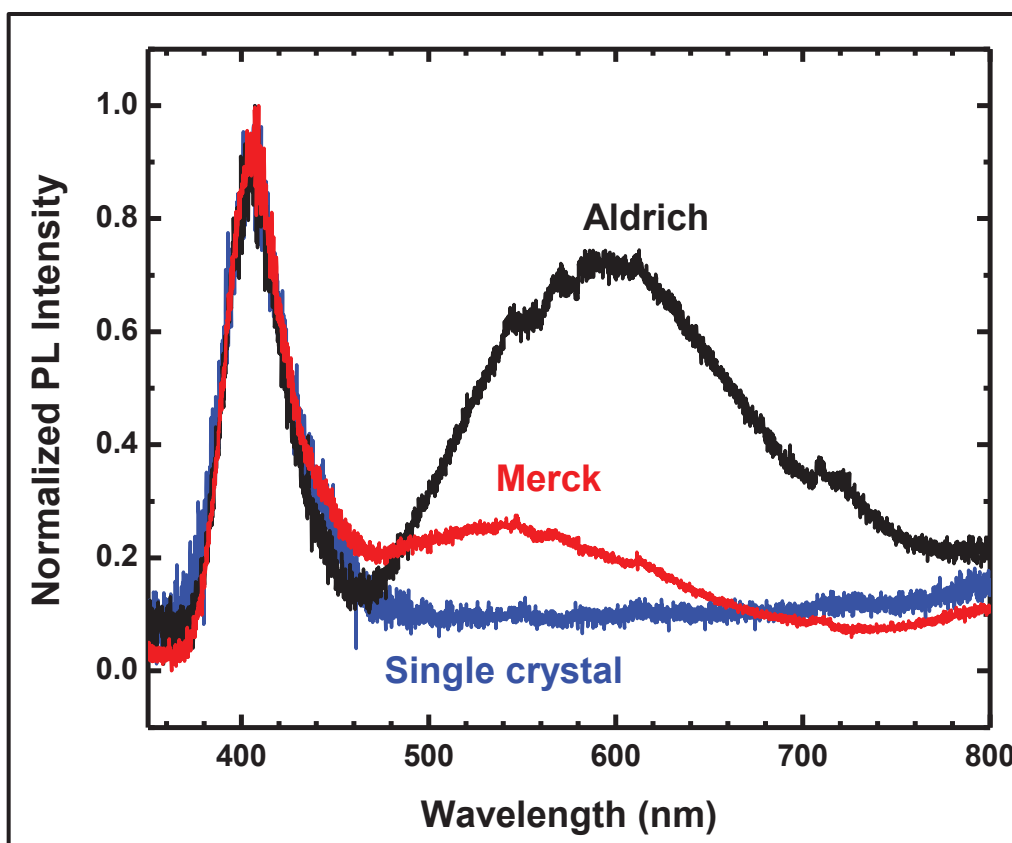


Figure 34 – Normalized photoluminescence spectra of the different SnO₂ samples, excited at 266nm.

c) Raman spectroscopy

Our Raman experiments were realized at CECOMO Platform, using the LabRAM HR Evolution spectrometer (as mentioned on chapter 1, section 1.2.2.b) using an excitation energy of 532 nm, and a power set at 5 mW to avoid heating. The beam was focused on the sample using a 50x objective, with a beam diameter of ~ 2 μm at the sample. The scattered light was collected in backscattering geometry using the same objective. As already mentioned in Chapter 1, such equipment has an interesting specificity of making the acquisition of spectra at frequencies starting from 5 cm^{-1} , which is a very important feature considering that Lamb modes (breathing modes, in the nanoparticles) are situated at low frequencies.

The Raman spectra of the different samples (single crystal and both powders) obtained at ambient conditions are shown in Figure 35. They clearly seem to have a similar behavior at ambient pressure. Such information reinforces the explanation of the why it was not necessary to perform DRX experiments on single crystal sample. Such similarity can be explained due to their low defects rate at the ambient pressure, however, in the next subsection, we will see that they will appear with the increase of the pressure, giving very different spectra.

Along with the expected Raman peaks, several weak features (signaled with black lines in the graph) are observed at $\sim 501\text{ cm}^{-1}$, 542 cm^{-1} , and 695 cm^{-1} . Such modes were assigned to IR active modes ($A_{2u}(\text{TO})$ and $A_{2u}(\text{LO})$), and to the forbidden mode B_{1u} , respectively.¹⁶⁵ Considering that the selection rules are well established for a perfect and infinite crystal, such rules may be broken by the presence of defects leading to the observation of non-active Raman modes, as it is in our case.^{165,170}

As mentioned in subsection 2.1 (Chapter 2), in all four Raman-active modes (A_{1g} , B_{1g} , B_{2g} , and E_g) the oxygen atoms vibrate while Sn atoms are at rest. The positions found of three of the four peaks – $\omega(E_g) \sim 475\text{ cm}^{-1}$, $\omega(A_{1g}) \sim 634\text{ cm}^{-1}$, and $\omega(B_{2g}) \sim 776\text{ cm}^{-1}$ – agree with those established in the literature. However, considering that the B_{1g} mode is a libration mode and, because there is a lot of Rayleigh scattering at low frequency, it is difficult to observe such mode, being absent in several spectra reported in the literature.

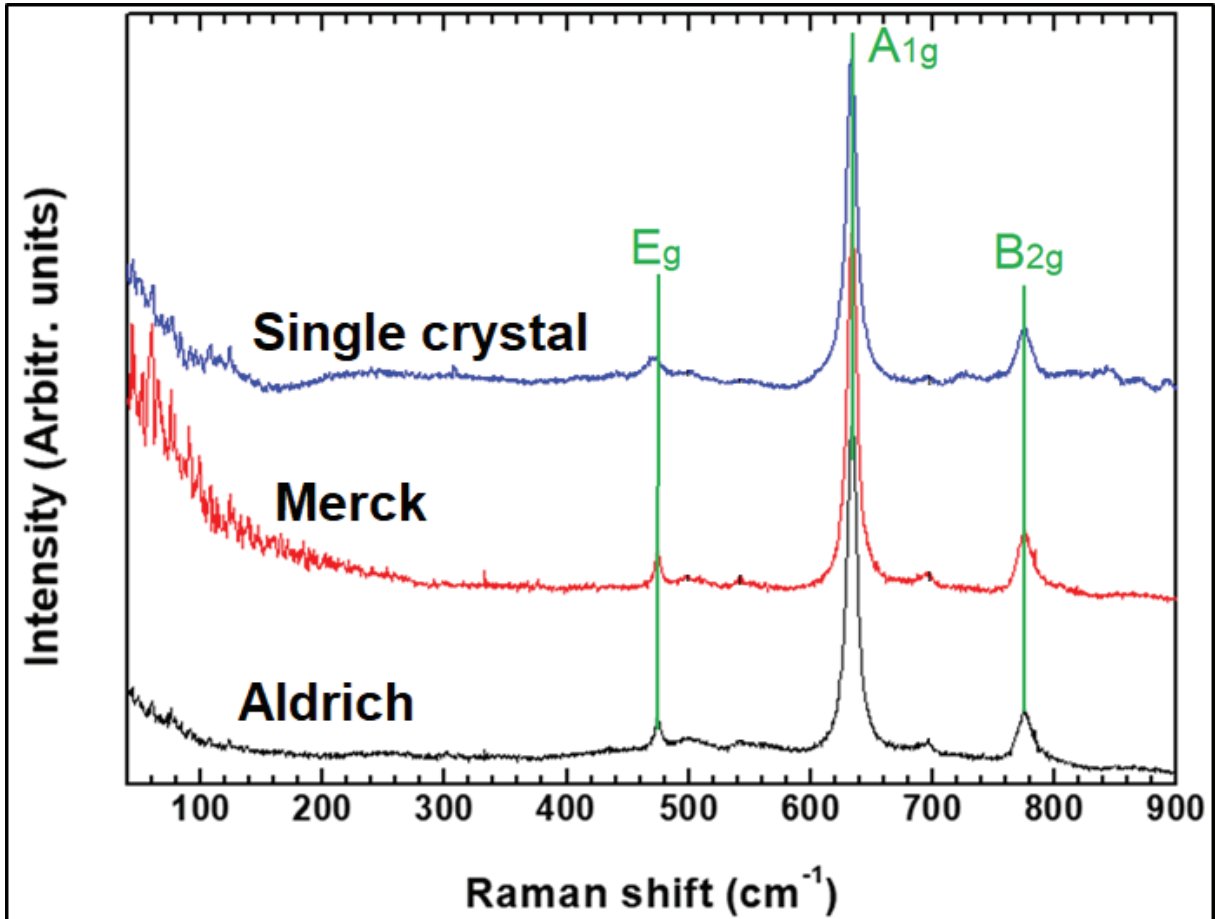


Figure 35 – Raman spectra of the different powders and single crystal under ambient conditions.

We simulated the Raman spectra for the SnO₂ (rutile phase). The B_{1g} peak position was found to lie at $\sim 102 \text{ cm}^{-1}$. However such peak it is a very weak compared to the other peaks. Its intensity ratio $I(B_{1g})/I(A_{1g})$ is equal to 5×10^{-5} , which confirms the difficulty to observe this peak. In Figure 36 we can see and understand these intensities discrepancies.

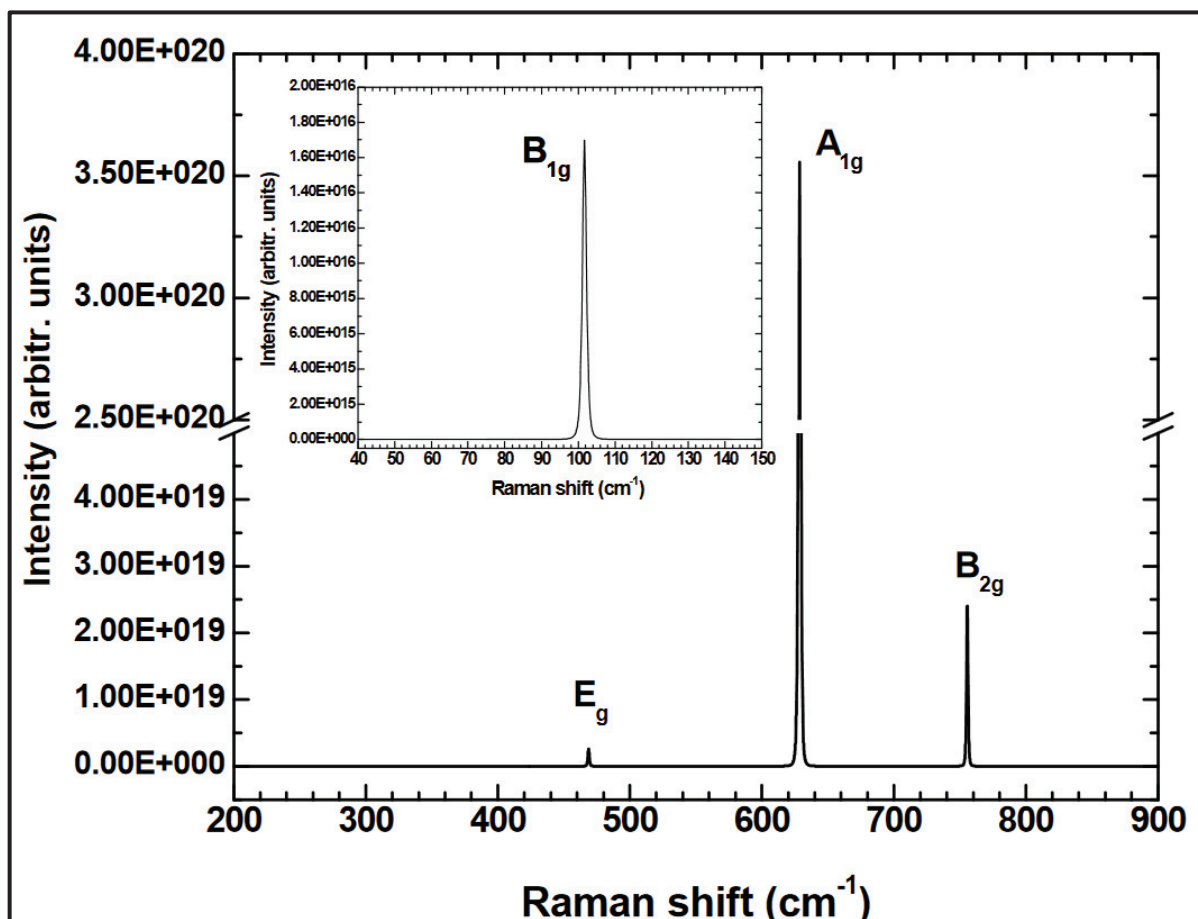


Figure 36 –Raman spectrum simulated of the rutile phase (frequencies and corresponding intensities).

3.2.2. Characterization at high-pressure

a) Raman Spectroscopy

Our high-pressure experiments were realized as a sequence of those at ambient pressure *i.e.* using the same equipment and under the same conditions. To generate the high-pressure, we used a diamond-anvil cell (DAC) with low-fluorescence diamonds (as explained in Chapter 1, subsection 1.2.1). The powders (one at a time) and single crystal samples were placed, respectively, into a 125 and 150 μ m chamber drilled in an indented stainless-steel gasket. Depending on the experiments, no pressure transmitting medium (PTM), methanol-ethanol mixture or paraffin oil were used. It is important to mention that initially, we tried to make the experiments in the same conditions but one of the samples did not work, so we have an odd comparison. The pressure was probed by the shift of the fluorescence line of a small ruby chip (see subsection 1.2.1, in Chapter 1, for further information).

Our experiments were conducted on different runs, namely: 1) Aldrich powder without PTM; 2) Merck powder without PTM; 3) Merck powder using 4:1 Methanol: ethanol mixture as PTM and, finally, 4) single-crystal using paraffin oil as PTM.

It is useful to remember that different PTM's were used in order to study and compare their hydrostaticity, considering that the such a factor can contribute to the promotion of the pressure-induced amorphization.

Table 3 shows some hydrostaticity coefficients associated to certain PTMs.

Table 3 – Nominal hydrostatic limits of pressure media. Adapted from refs.^{72, 73 and 171}

Pressure transmitting medium (PTM)	Hydrostatic limit (GPa)
16:3:1 Methanol – ethanol – water	10.5 ± 0.5
4:1 Methanol–ethanol	9.8 - 10.3
Paraffin oil	5 - 7
Argon	1.9
Nitrogen	3.0
Glycerol	1.4
Silicone oil, viscosity 0.65 cSt	0.9
Silicone oil, viscosity 37 cSt	0.9

- **Aldrich and Merck powders under pressure without PTM.**

The following part is dedicated to the study of the high-pressure experiments realized on the Merck and Aldrich powder, using Raman spectroscopy as a characterization technique. Such experiments were carried out without a pressure-transmitting medium. Their spectra are plotted in Figure 37a and Figure 37b and we can notice that its evolution is quite similar.

We will follow the SnO₂ behavior under pressure paying attention to the evolution of the principal peak (A_{1g}) situated at $\sim 634 \text{ cm}^{-1}$ associated to the emergence and the grown of the peak P1 located at $\sim 122 \text{ cm}^{-1}$.

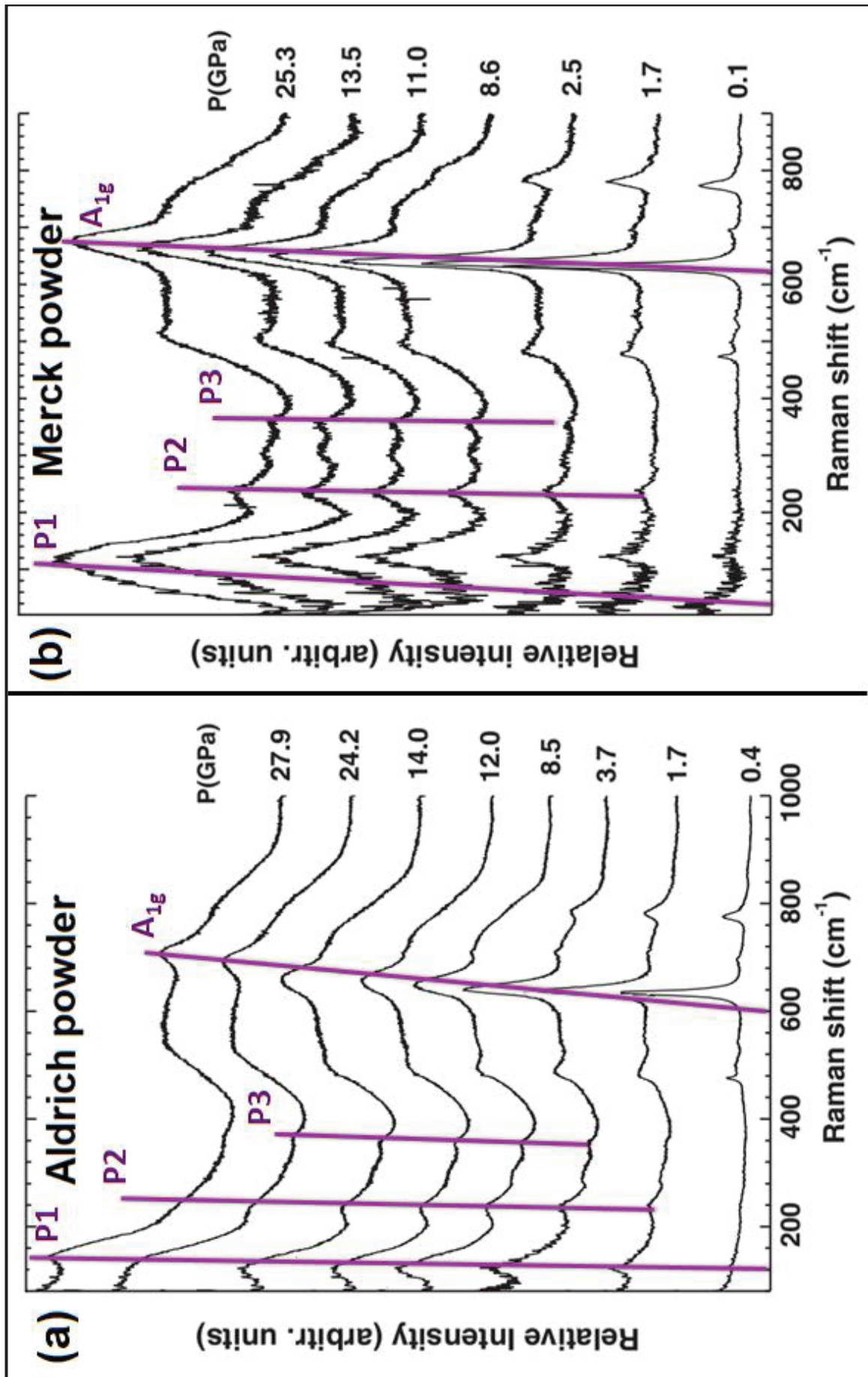


Figure 37 – (a) Raman spectra of SnO₂ powder (Aldrich) with increasing pressure (No pressure-transmitting medium). (b) Raman spectra of SnO₂ powder (Merck) with increasing pressure (No pressure-transmitting medium).

In the first steps of compression, we can notice the appearing of a background between 400 and 850 cm⁻¹. Simultaneously, we can also observe the arising of two other new peaks at lower frequencies in addition to P1. They are founded at P2 ~ 235 cm⁻¹, and P3 ~ 355 cm⁻¹. We observed that especially the low-frequency mode located at around 122 cm⁻¹ (P1) increases very quickly in intensity. Its presence is even more striking starting from 8.6 GPa, principally to Merck powder. Both the P2 (located at ~235 cm⁻¹) and the P3 (found at ~355 cm⁻¹) will vanish at pressures higher than 27.9GPa. Furthermore, even the peak lied at ~780 cm⁻¹ will disappear at pressures above 3.7GPa.

The peaks which appear at the low-frequency band seem to be related to the concentration of defects within the structure developing with the increase of pressure. A possible interpretation of such appearance is linked to the fact that they may be the forbidden modes¹⁶⁵ which become active because of the break of the selection rules due to the presence of defects. For instance, the calculated frequency of a second B_{1u} mode lies around 140 cm⁻¹,¹²⁹ a E_u(TO) mode is also found in the vicinity of the observed frequency at ~235 cm⁻¹ and a E_u(LO) is found to be near 355 cm⁻¹.¹⁷²

Some works^{115,120} report the B_{1g} mode at ~120 cm⁻¹, at ambient pressure. However, such attribution should be revised, and this peak should be assigned as a B_{1u} mode. Such kind of peak is usually activated by the presence of defects.

It is interesting to remark that the Raman spectra change drastically at a low pressure, but an additional compression does not induce a strong further qualitative change, *i.e* the general shape of the spectra does not change with the increase of the pressure, even above ~11 GPa. At such pressure, one expects a phase transition from rutile-to-CaCl₂-type structure,⁹ although, considering the nonhydrostatic stress, such a transition is expected to happens at a lower pressure.

The appearance of the broad bands agrees with a disordering of the structure (see Figure 57). Considering that some broadening of the peaks is attended when a sample is amorphized under pressure, such behavior can be attributed to a pressure-induced amorphization (PIA). However, such conclusion is not supported by the reports in the literature based on X-ray diffraction experiments,^{121,123,156} considering that such a transformation has never been observed. Since no support was found in the literature in X-ray diffraction experiments, a possible explanation for such broadening, can be found in Haines and Léger's⁹ work. When studying SnO₂ under

high-pressure using X-ray diffraction, they had noticed that when a powder is compressed using a PTM that does not guarantee the hydrostaticity (silicon grease, in their case), the broadening of the diffraction peaks may be correctly indexed when using a CaCl₂ structural model in the refinement but with a slightly larger cell parameter.

Thus, for our powder samples, we can conclude that the broadening of the A_{1g} peak can be related to the phase transformation from rutile-to-CaCl₂-type. Besides, even if there is no support in X-ray reports, recently, Girão *et al.*¹⁶⁰ working with SnO₂ nanoparticles under high-pressure, and using Raman spectroscopy as main characterization technique, associated such broadening to a partial pressure-induced disorder of the oxygen sublattice, *i.e.* only the anionic sublattice will suffer amorphization.

- **Merck powder under pressure using 4:1 Methanol: ethanol mixture as PTM.**

It is known that the non-hydrostaticity can promote an amorphous state instead of the crystalline phase.¹⁷³ So, with the purpose of checking the hydrostaticity effect, we did a third experiment using the Merck powder. In order to ensure an hydrostatic compression up to ~10 GPa,^{72,73} we used a 4:1 methanol-ethanol mixture as a pressure-transmitting medium. It is interesting to mention that we could have used helium as PTM (hydrostatic limit ~ 30 GPa), however such option was tried before on previously works and was discarded it due to the loading difficulties.

The Raman spectra presented in Figure 38 show a general pressure-induced evolution quite identical to the case without a PTM. The main difference between them lies in the relative intensity between the low-frequency and the high-frequency regions at high-pressure. In this case (using PTM), the low-frequency modes are much more intense than the high-frequency modes, differently from the previous experiments (without PTM), which the high and the low-frequency peaks have almost the same intensity.

During the compression, it is very complicated to separate the interaction between the morphology of the sample and the hydrostatic conditions. Thus, an amorphous-like signature can occurs thanks to the intergrain contact. Such contact

may induce the local shear stresses, even if the powder sample is compressed with a PTM which provides a good hydrostaticity (to 10 GPa, only).¹⁷⁴

Similarly to the behavior of the non-hydrostatic compression, a peak at ~ 122 cm⁻¹ appears at low pressure. Such peak increases in intensity concomitantly with a rise of a background in the high-frequency region (400-800 cm⁻¹). Considering that the Raman spectra may be interpreted as a vibrational density of state, such behavior may be associated to the signature of a progressive disordering.

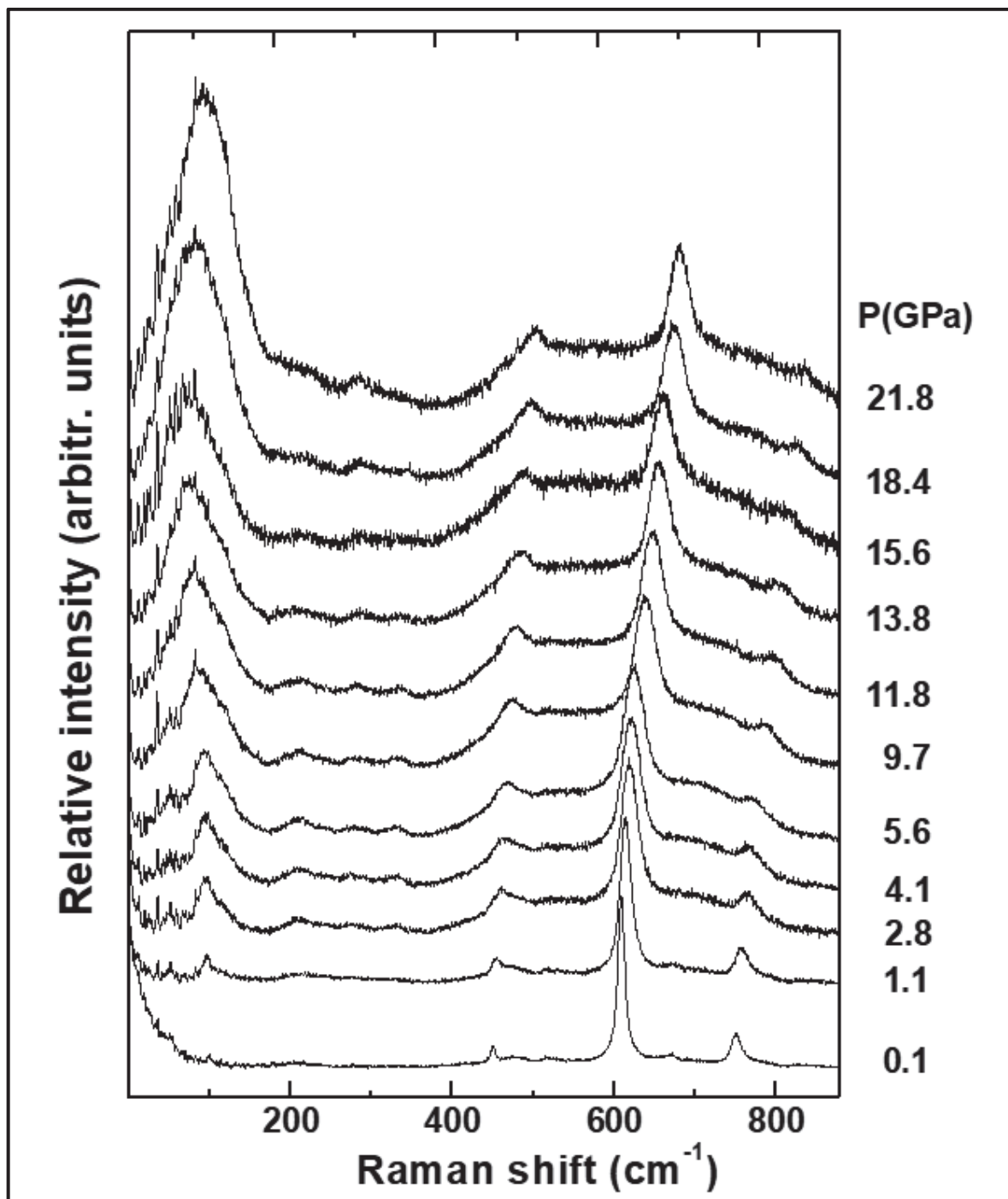


Figure 38 – Raman spectra of SnO₂ powder (Merck) with increasing pressure using a 4:1 methanol-ethanol mixture as the pressure transmitting medium PTM.

- **Single-crystal under pressure. Paraffin oil as PTM.**

Such last high-pressure experiment, the fourth, was realized on the single-crystal sample. The sample was immersed in paraffin oil as the PTM, and the hydrostaticity was ensured up to ~ 3 GPa, *i.e.*, we can consider it as a non-hydrostatic PTM even if such value was found to be higher than that one proposed by Klotz *et al.*⁷² and by Angel *et al.*⁷³. With such experiment, we have the purpose of investigate the effect of (i) the form of the sample; and (ii) the hydrostaticity. Such an experiment was performed up to $\sim 22,6$ GPa and its evolution under high-pressure can be observed in Figure 39.

Observing the red, purple, blue, and green lines draw in the spectra shown in Figure 39, we can notice that the Raman peaks upshift with pressure increasing. These behaviors can be confirmed when observing the Figure 39, in which it was plotted the evolution of the peaks with the increasing of the pressure.

It is important to remark that we could not see/measure the B_{1g} mode (soft mode) at ambient pressure, however, we can observe the raising of a low-frequency peak at ~ 75 cm⁻¹ in pressure starting from ~ 7 GPa. Keeping with increasing pressure, this peak upshifts until the position ~ 120 cm⁻¹ but it maintains with a low intensity until 11.3 GPa. After this pressure, such peak gain in intensity becoming the most intense peak in the Raman spectra. Such peak evolution can be followed observing the red line, and it is expected in the rutile to CaCl₂-type phase changes.

The peak observed initially at ~ 420 cm⁻¹ upshift until ~ 540 cm⁻¹ with the increase of the pressure, as can be seen observing the purple line. Additionally, this peak disappears at ~ 22 GPa. The principal peak initially situated at ~ 640 cm⁻¹ upshift until ~ 720 cm⁻¹. Its evolution can be monitored by observing the blue line's behavior. The last peak initially placed at ~ 780 cm⁻¹ moves until ~ 860 cm⁻¹. Its evolution can be followed by observing the green line's behavior. We can find all their pressure-induced evolutions in Figure 40. These results are in good agreement both with the *ab initio* simulations (open symbols in Figure 40) and with the previous values reported in the literature.¹⁰

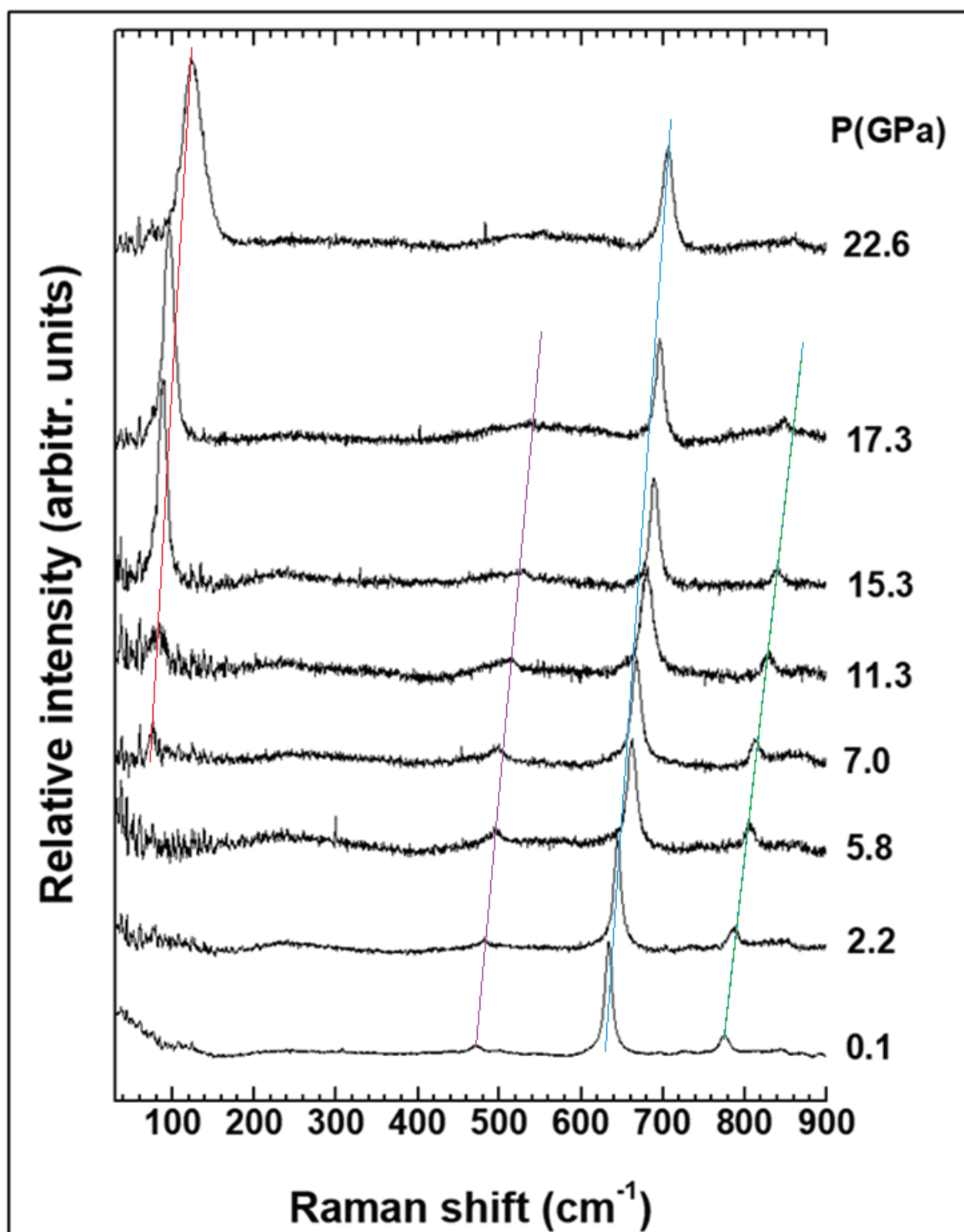


Figure 39 – Raman spectra of a non-oriented SnO₂ single crystal under pressure using paraffin oil as PTM.

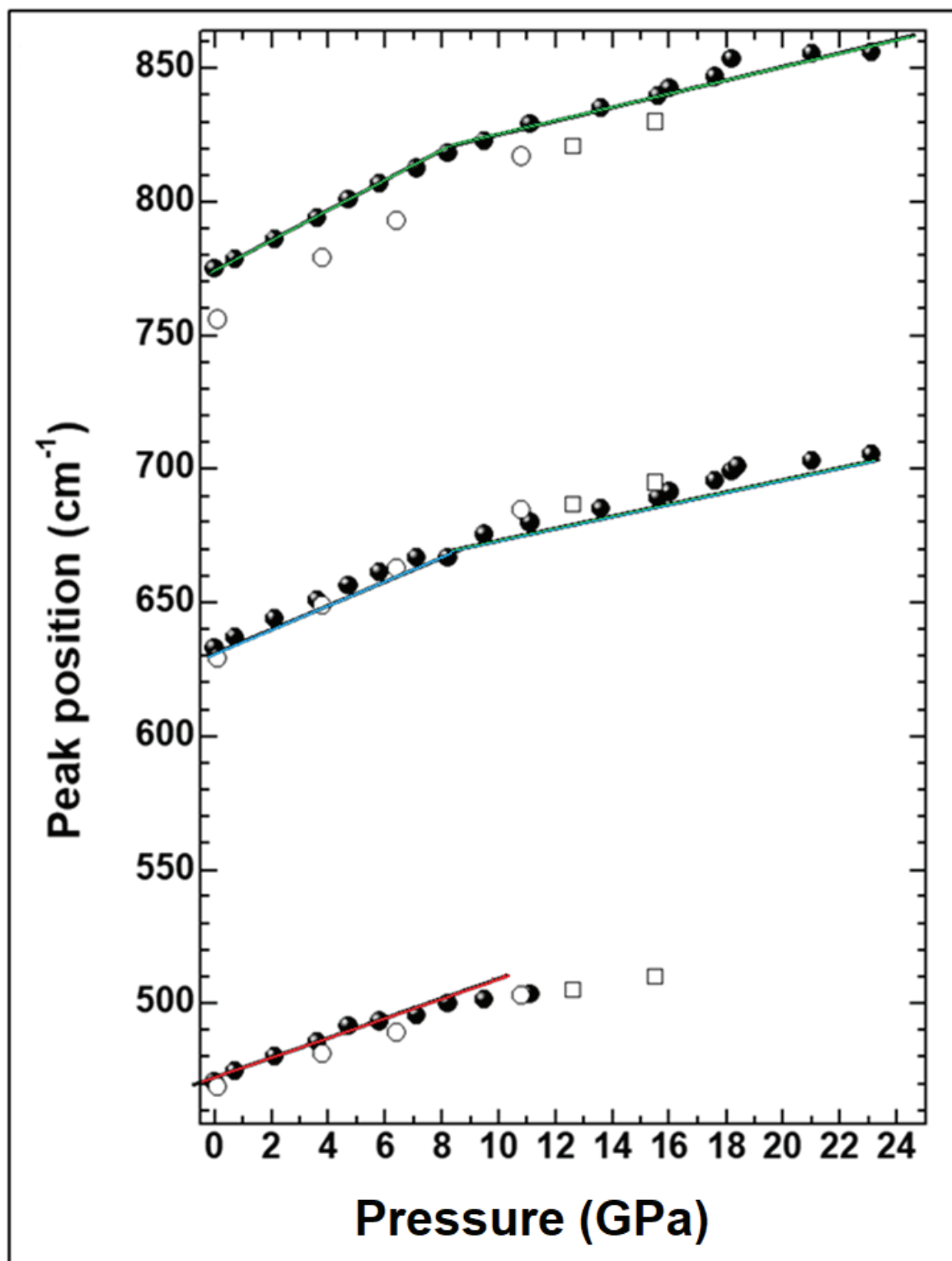


Figure 40 – Peak position as a function of the pressure.

The variation of the intensity of the peaks at high-frequency with the pressure agrees with the lowered transition pressure. This lowered transition pressure may be associated with the effect of non-hydrostatic stress components. For example, Hemley *et al.*¹⁷⁵ demonstrated a linkage between the strain and the order parameter, in the case of a similar ferroelastic transition in dense (stishovite) SiO₂.

- **Comparison between the different samples before and after pressure cycle.**

Figure 41 and Figure 42 show the comparison between the Raman spectra of the different samples before and after pressure cycle, respectively. We can see that the both powders which were pressurized under non-hydrostatic conditions show similar spectra at high-pressure. However they present subtle differences in the low-frequency peak. Such low-frequency peak ($\sim 122\text{ cm}^{-1}$) is certainly due to the transformation from rutile to CaCl₂-type structure.

We can also observe that the powder which is compressed under hydrostatic conditions does not lead to a complete disordering. Such behavior may indicate that the sample is a mixture between ordered and disordered zones. Therefore, it is worth noting that the non-hydrostaticity may promote the activation of the presence of defects through shear stresses. In addition, the non-hydrostaticity can conduct to some difficulties the X-ray diffraction pattern refinement.⁹

Finally, we can also perceive that the single-crystal, which was compressed under non-hydrostatic conditions, does not show any marked disordering.

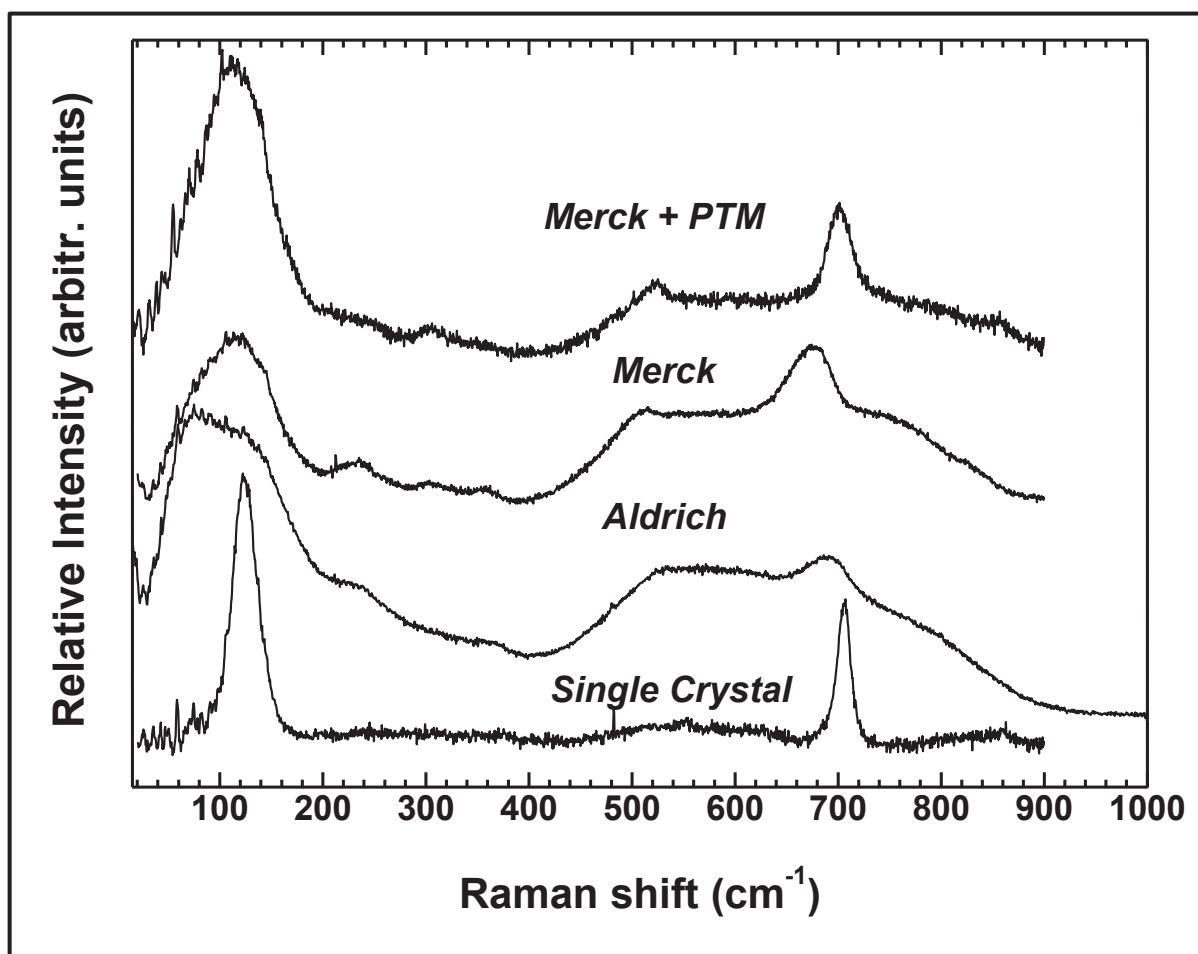


Figure 41 – Comparison of the spectra at high-pressure ($P > 20\text{ GPa}$) for each experiment.

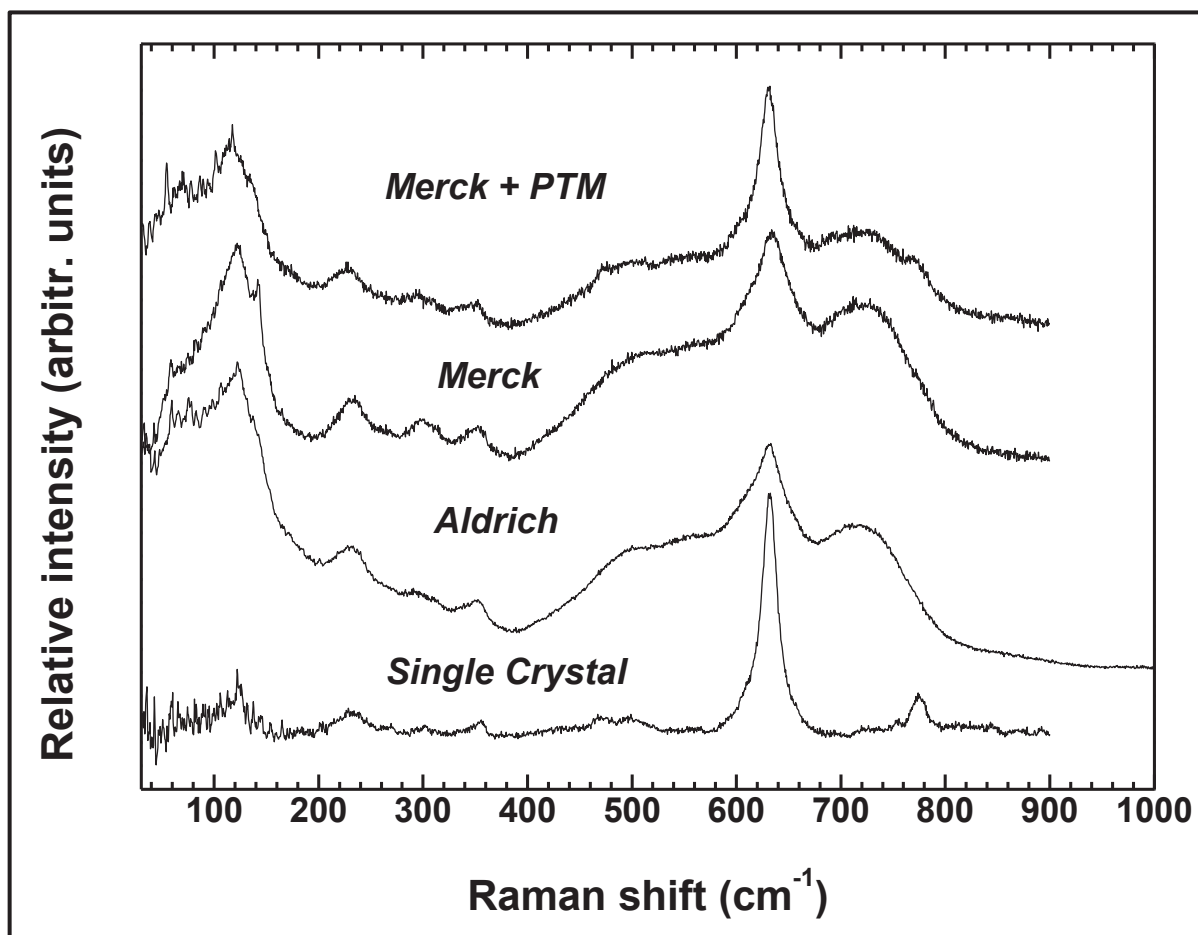


Figure 42 – Comparison of the spectra after pressure cycle for each experiment

b) First-principles calculations

First-principle calculations were performed in collaboration with Patrick Hermet from the *Université de Montpellier*, within the density functional theory (DFT) framework as implemented in the ABINIT package.¹⁷⁶ The exchange-correlation energy functional is evaluated using the local density approximation parametrized by Perdew and Wang.¹⁷⁷ The all-electrons potential is replaced by norm-conserving pseudopotentials. Sn ($4d^{10}, 5s^2, 5p^2$) and O ($2s^2, 2p^4$)-electrons are considered as valence states. The electronic wave functions are expanded in plane waves up to kinetic energy cutoffs of 60 Ha* and integrals over the Brillouin zone are approximated by sums over an 8x8x8 mesh of special k-points according to the Monkhorst-Pack scheme.¹⁷⁸

* Generally, in Rydberg 1 Hartree= 2 Rydberg

Dynamical matrix, dielectric constants and Born effective charges are calculated within a variational approach to density functional perturbation theory (DFPT). Phonon dispersion curves are interpolated according to the scheme described by Gonze *et al.*¹⁷⁹ In this scheme, the dipole-dipole interactions are subtracted from the dynamical matrices before Fourier transformation so that only the short-range part is handled in real space. We considered a 2x2x2 q-points grid for the calculation of the phonon band structure and a denser 100x100x100 grid is used for the calculation of the phonon density of states (also called vibrational density of states – vDOS).

The broad features observed in powders during compression resemble a vibrational density of states (VDOS) observed when the Raman selection rules are broken because of the presence of disorder. The simulated vDOS of the rutile structure at 3.8 GPa have been computed and compared to the experimental data at the same pressure, and they can be seen in Figure 43a.

Comparing the bands of the both Raman spectrum, we can notice an evident similarity between the broad bands observed in powders during compression (Aldrich, specifically) and the simulated vDOS when the presence of disorder breaks the Raman selection rules. The evolution of the simulated peaks can be followed observing the black lines in the Figure 43b.

These results are in very good agreement with the maxima of the phonon density of states. The experimental data were well reproduced by the simulations (see Figure 43b when considering a structural transformation to the CaCl₂-type form with the increasing of the pressure. For instance, the peak at ~122 cm⁻¹ is found to remain in the same position in both simulations and experiment.

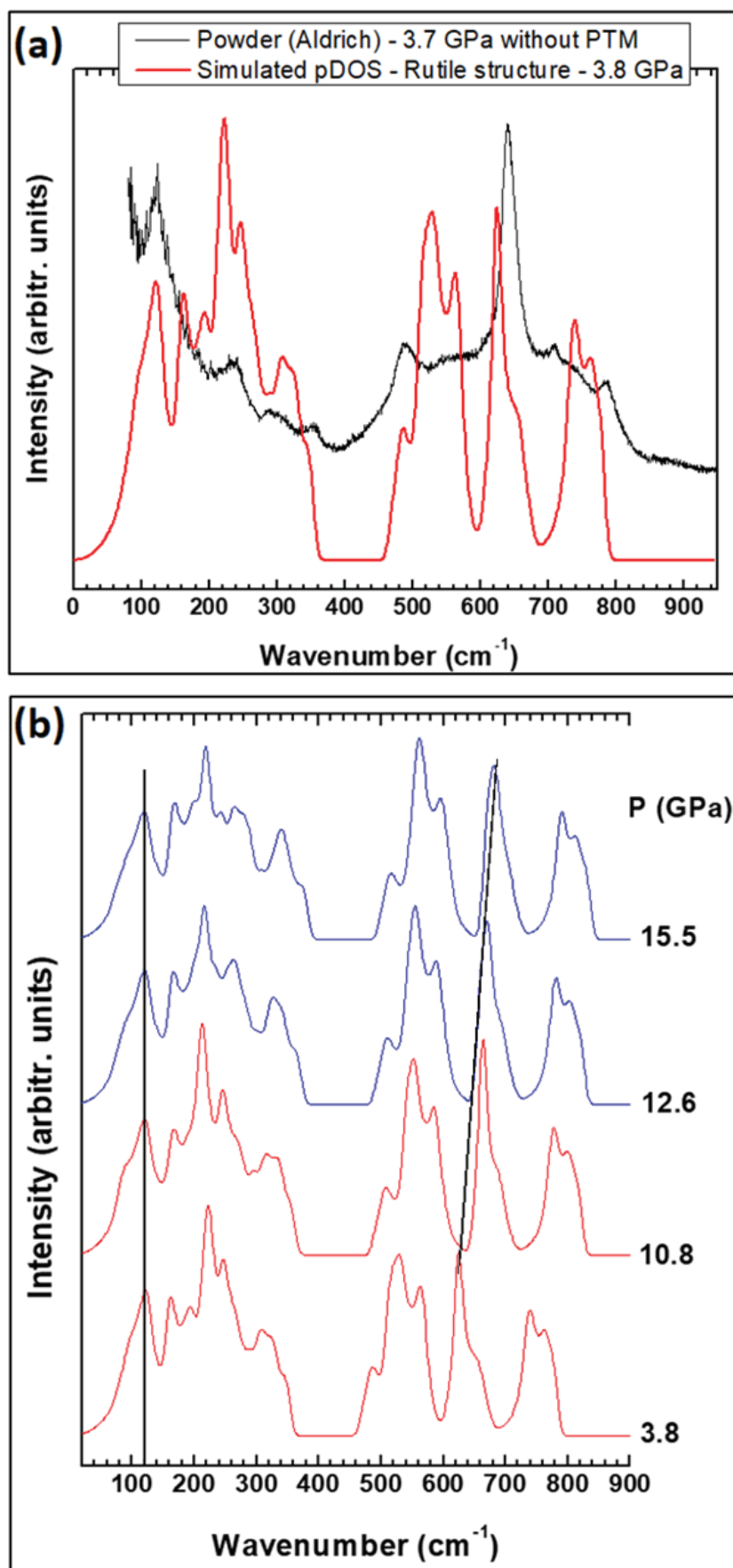


Figure 43 – (a) Comparison of the Raman spectrum of SnO₂ powder with a calculated phonon density of states of the rutile structure at ~3.8 GPa. (b) Simulated vDOS at different pressures in rutile (red) and CaCl₂-type (blue) structures. The black lines follow the peak evolution under pressure

3.3. Discussion

Previous studies on SnO₂ crystal at high-pressure seem to give a coherent picture for its phase transition mechanism. We found a lot of discrepancies between the high-pressure behaviors of powder and single-crystal samples, *i.e.* SnO₂ powder samples have a more complex behavior compared to single-crystal. We can describe its structural phase transitions during the pressure-induced transformations based on the decoupling of sublattices.

In complex structures of rare earth molybdates, a two-step amorphization has been observed whatever the form of the samples. The anionic sublattice starts to exhibit amorphous-like Raman, photoluminescence or EXAFS signatures at a lower pressure than the cationic sublattice probed by X-ray diffraction.^{170,180} However, amorphization pressures for both sublattices are significantly lower in a powder than for a single crystal. Partial (sublattice) amorphization has also been discussed in Co(OH)₂ where infrared spectroscopy reported a disordering of O-H sublattice.¹⁸¹ Interestingly, in Ca(OH)₂ a disordering of Ca-O and O-H sublattices occurred simultaneously.¹⁸² To the best of our knowledge, such a decoupling between sublattices in simple and dense structures has never been reported*

Considering that Raman spectroscopy is very sensitive to the oxygen sublattice, it appears that the disorder which affects the Raman spectra only affects such sublattice, as in the case of pressure-induced transformations in SnO₂ nanoparticles.¹⁶⁰ It is important to remark that Raman spectroscopy does not reveal the disorder of Sn sublattice. Such conclusion that only oxygen sublattice suffer disorder was taken considering XRD behavior.

We observed a strong correlation between the presence of defects initially present in the samples and the selective disordering in SnO₂ upon compression. This correlation can be explained by invasive percolation and will be discussed in the following. Such an approach has been used with some success in the case of size-dependent pressure-induced amorphization by explaining the lower of the amorphization pressure with a decreasing nanoparticle size.¹⁸⁴

* For a discussion on the notion of complexity of a structure, see ref. ¹⁸³.

A little about invasive percolation theory...

In this study, it was used the invasive percolation theory to explain the process of the anionic sublattice disorder. While the standard theory of percolation is related with static properties of the medium, the invasive percolation theory is a form of percolation that considers the transport process taking place. The model was motivated by the problem of one fluid displacing another from a porous medium under the action of capillary forces described in the Chandler *et al.*¹⁸⁵ study.

The invasive percolation theory considers a specific dynamical model on the microscopic scale which describes the displacement process at a constant flow rate, rather than at constantly applied pressure. It is this feature which leads to the dynamical rule of advancing the interface at the point of least resistance, as opposed to advancing all interfaces up to some chosen threshold resistance. In principle, the invasive percolation theory may be applied to any kind of invasion process which proceeds along a path of least resistance. The theory also considers that must exist local variations in the medium which have a strong effect on the invasion process.¹⁸⁶

We must to consider that a sample as divided in two domains A and B, where the domain A will be the crystalline one (the defender), and the domain B will be the amorphous one (the invader). Since we have an increase of the pressure, the domain B will attack the domain A, and the structure which was crystalline starts to be amorphous.

In our case, the defects which are present on the oxygen sublattice will invade the stain sublattice conducting the structure to an amorphization. Even though the total amorphization does not happen, we can see clearly that is the anionic sublattice which leads the disorder.

Let us now present our model.

Long-range correlations in crystalline solids were demonstrated by Mermin and Wagner.¹⁸⁷ These correlations are needed in a crystalline solid that undergoes a structural phase transition, considering that all sites must change their bonding or coordination state simultaneously to preserve the translational symmetry.¹⁸⁷ However, these long-range correlations can be affected by crystal defects: atoms are statically displaced from an ideal lattice and can be viewed as perturbations to the lattice introducing local fluctuation. Defects can be present initially or created during the

compression process (for instance during a reconstructive phase transition). High defect density (points or extended defects) will, in turn, favors local correlations and the formation of the local amorphous state.

Percolating systems have a parameter p which controls the occupancy of sites in the system: a Voronoi cell. This parameter represents the probability of a site to be amorphous and it increases with increasing pressure and shear stresses developing in powder samples. A Voronoi cell can be defined around each defect. When approaching the stability field of the amorphous state, this cell can present two possible states: a crystal-like or an amorphous-like. Figure 44 represents a percolating system where we can define the “experimental” crystal-to-amorphous transition at the percolation threshold.

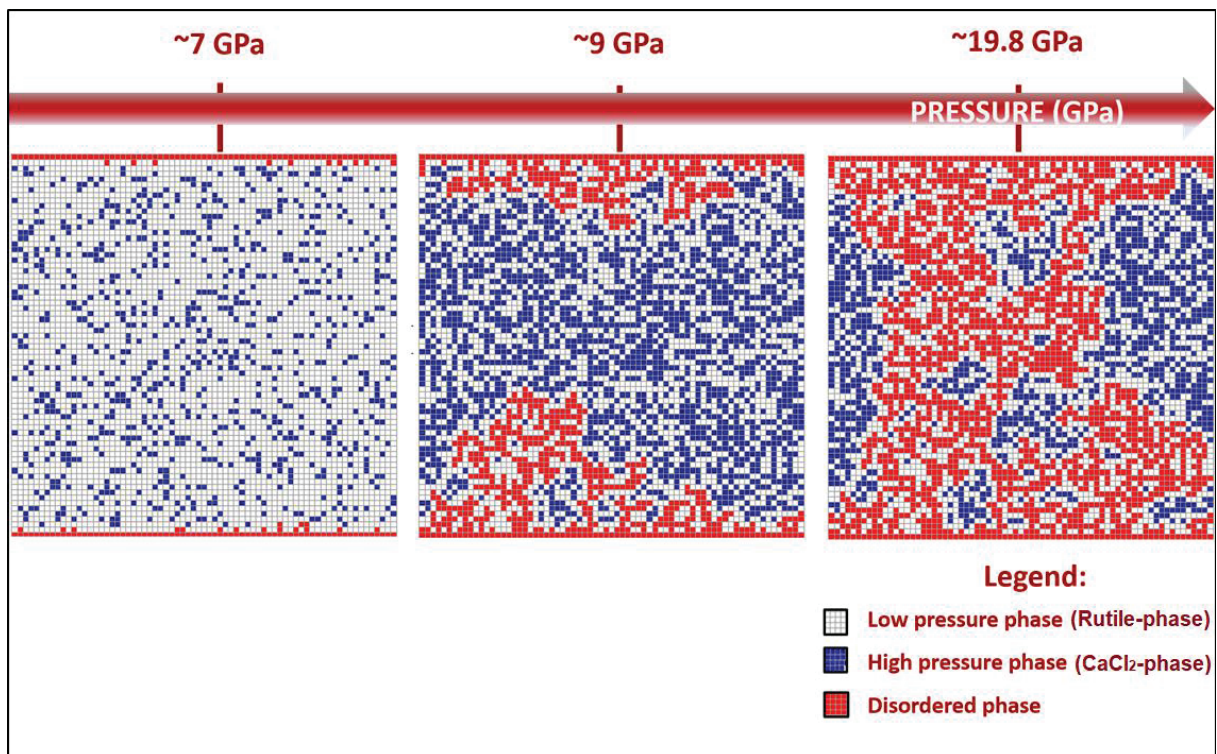


Figure 44 – Representation of oxygen sublattice disorder by an invasive percolation system with an increase of pressure. Adapted from ref. ¹⁸⁸

The Voronoi cells are independent but an amorphous cell grows during pressurization above the critical pressure. In this case, this corresponds to an invasive percolating system where the amorphous state is the invader and can penetrate the isolated crystallized region (so-called defender). This is called invasive percolation without trapping. It has been established that percolation without trapping and regular percolation are of the same universality class.¹⁸⁹ Thus, microscopic description of the transition at a local order is not necessary. The propagating disorder leads to an

amorphous-like (VDOS) Raman spectra at the percolating threshold as discussed in Ref. 33. The key point of the description is the fractal structure of the infinite cluster defined just above the percolation threshold as discussed by Machon *et* Mélinon.¹⁸⁴

At a critical value $p = p_c$, where the percolation transition takes place, the mean cluster size given by the correlation length ξ diverges following a power law:¹⁹⁰

$$\xi \approx \xi_0 |p - p_c|^{-\mu} \quad (5)$$

Where μ is the critical exponent which depends on the type of percolation and on the type of lattice.¹⁹¹ The crystal-to-amorphous transition occurs at the percolation threshold. The offset between the pressures of polymorphic transition and of amorphization $\Delta P = P_c^* - P_c^{am}$ can be determined by {26}

$$\Delta P = \frac{\xi^{2\mu-2}}{\alpha_0 \xi^{2\mu} \Gamma^2(3-\mu)} \quad (6)$$

Where Γ is the Euler gamma function, ξ is the microscopic correlation length, and α_0 is a numerical parameter. The maximum offset is given for an invasive percolating system $D_f = 2.5$ (ref. 27) and yields

$$\Delta P_{max} \approx \frac{16\xi^{-2}}{9\alpha_0\pi} \quad (7)$$

The microscopic correlation length ξ is defined in percolation theory as the typical radius of the largest finite cluster. In the case of nanoparticles, ξ cannot exceed r , the radius of the nanoparticle. This spatial limitation leads to

$$P_c^{am} = P_c^* - \frac{16}{9\alpha_0\pi r^2} \quad (8)$$

Where P_c^* is the polymorphic transition pressure in the nanoparticle. This pressure can be expressed as

$$P_c^* = P_c + 3\delta \frac{\gamma_{hp} - \gamma_{lp}}{\alpha_0 \cdot r} \quad (9)$$

Where P_c corresponds to the polymorphic transition pressure in the bulk material.

Finally,

$$P_c^{am} = P_c + 3\delta \frac{\gamma_{hp} - \gamma_{lp}}{\alpha_0 \cdot r} - \frac{16}{9\alpha_0 \pi r^2} \quad (10)$$

It has been demonstrated that amorphization occurs only when a sufficient defect density is attained in the nanoparticles,^{23,32} *i.e.*, when the number of sites is sufficient to reach the percolation threshold. When the defect density is sufficient, then amorphization may occur at a critical size (which depends on the materials). In that case, a crossover can occur and amorphization becomes the dominant mechanism. One striking consequence is that $\Delta P > 0$, *i.e.*, the crystal-to amorphous transition occurs at a lower pressure than the polymorphic transformation. This prediction has been observed in all experimental reports of size-dependent PIA.^{32,23,192}

It is important at this point to discuss the possible experimental discrepancies depending on the analytical techniques. At the percolation threshold, not the whole sample becomes amorphous ($p_c = 0.2$ for sites in fcc lattice).¹⁹³ However, due to the fractal nature of the amorphous state, the spatial distribution is highly inhomogeneous. The density of crystallized clusters n of size s (s being the number of Voronoi cells) decreases rapidly according to the law:¹⁹³

$$n(s) = s^{-\tau} (2 < \tau < 2.5). \quad (11)$$

Consequently, the remaining crystalline domains are small (typically few distances between two adjacent defects) and may be smaller than the correlation length of the characterization probe leading to an amorphous-like material even though a significant part of the sample is still crystalline. In SnO₂, the typical distance between oxygen atoms is 2.8 Å which means that crystalline domains are of the nanometer scale.

In our case, this invasive percolation is restricted to the oxygen sublattice and the cationic sublattice is resistant to this invasive percolation. This property seems related to the closed-packing of the cations. Thus, in the rutile and CaCl₂-type structures, the Sn atoms are arranged through a centered tetragonal lattice. In the PdF₂-type form, this sublattice slightly evolves into an *fcc* arrangement. Therefore, the pressure-induced phase transitions mainly involve the oxygen sublattice.¹²¹ The stability of the cationic sublattice that is close-packed-like may act as a rigid backbone, showing only pressure-induced distortion without diffusion. This strongly supports

recent papers on oxides, reporting the observation that the crystal structures and even the unit cell dimensions of oxides depend on cation-cation interactions.^{194,195} The changes in the oxygen sublattice that are responsible for the phase transitions allow defects in this substructure to propagate. To observe the phase transformation – here called percolation – it is not necessary to observe a complete transformation of each particle. It is enough a percolation threshold of $< 1^*$.

The explanation of such resistance to pressure-induced amorphization may be extended to other examples. In ZnO, no pressure-induced amorphization has been reported. In the case of defective nanocrystals, Raman spectra resembling a vDOS appear at $P = 9$ GPa, the transition pressure from the wurtzite to the rocksalt structure. X-ray diffraction does not report such disordering, an observation like the case of bulk SnO₂. On the contrary, in ZnO nanoparticles with a very low defect concentration, no such vDOS has been observed using Raman spectroscopy.³⁷ Close inspection of the cationic sublattice indicates that Zn atoms in the wurtzite structure are arranged through an *hcp* packing. In the high-pressure rocksalt structure, cations are also in an *fcc* close-packed arrangements.

* Where 1 is the whole system

Chapter 4

SnO₂ nanoparticles study under high-pressure

Table of contents

Chapter 4	90
4.1. Synthesis and characterization methods	91
4.1.1. The Synthesis	91
4.1.2. The characterization at ambient pressure	93
a) <i>Transmission electron microscopy (TEM)</i>	93
b) <i>X-ray Diffraction (XRD)</i>	95
c) <i>Raman spectroscopy</i>	96
4.1.3. The characterization at the high-pressure.....	99
a) <i>X-ray diffraction</i>	99
b) <i>Raman Spectroscopy</i>	100
c) <i>The ab-initio Simulations</i>	109
4.2. Discussion	110

In this chapter, we will talk about our experiments with SnO₂ nanoparticles under the high-pressure. Our nanoparticles were produced by chemical way (Sol-gel) and studied up to approximately 20 GPa using Raman spectroscopy in a diamond anvil cell and by using *ab initio* simulations. This technique was chosen for two main reasons: *i*) it allows us to probe optical phonons that are related to the oxygen sublattice, and *ii*) to follow the confined acoustic modes. Disorder was initially located at the surface, and above ~7 GPa it propagates to the center of the nanoparticles leading to an amorphous-like spectra. This behavior was understood as a disordering of the oxygen sublattice, which is specially probed by Raman spectroscopy. Such behavior conflicts with powder X-ray diffraction technique data. The goal of this chapter is to explore the pressure-induced phase transformation in SnO₂ nanoparticles by Raman spectroscopy.

4.1. Synthesis and characterization methods

Here we will talk about the synthesis method used to produce our nanoparticles as well the experimental and numerical techniques used in this work. Sample characterization will be detailed emphasizing the low-frequency region recorded in Raman spectra. Pressure-induced evolution of the low-frequency mode shown were modeled using bulk parameters, from the literature. Furthermore, X-ray diffraction will be shown to support the use of these data. In the final part of this chapter, the high-frequency region of Raman spectra of SnO₂ nanoparticles under pressure will be presented and discussed in the light of *ab initio* simulations.

4.1.1. The Synthesis

Our tin dioxide nanoparticles were prepared by the sol-gel method.¹⁹⁶ In a typical procedure, 7 mL of is tin(IV) isopropoxide* in 10% weight per volume isopropanol/toluene (1.97 mmol) were added to a refluxing aqueous solution (50 mL) of 0.636g of tetraalkylammonium bromide[†] under vigorous stirring. After an immediate precipitation, the medium was heated under reflux for 2h. Solid was separated by centrifugation and then was washed twice with deionized water and once with ethanol, and finally, dried at 70°C for 20 h, obtaining the SnO₂ nanoparticles.

A synopsis of the procedure used in this experiment to obtain SnO₂ nanoparticles can be seen in Figure 45.

* Sn(OⁱPr)₄(HOⁱPr)₂, where i = iso and ⁱPr = CH(CH₃)₂.

[†] N(ⁿBu)₄Br, where the capital N is nitrogen and ⁿBu stands for normal butyl group.

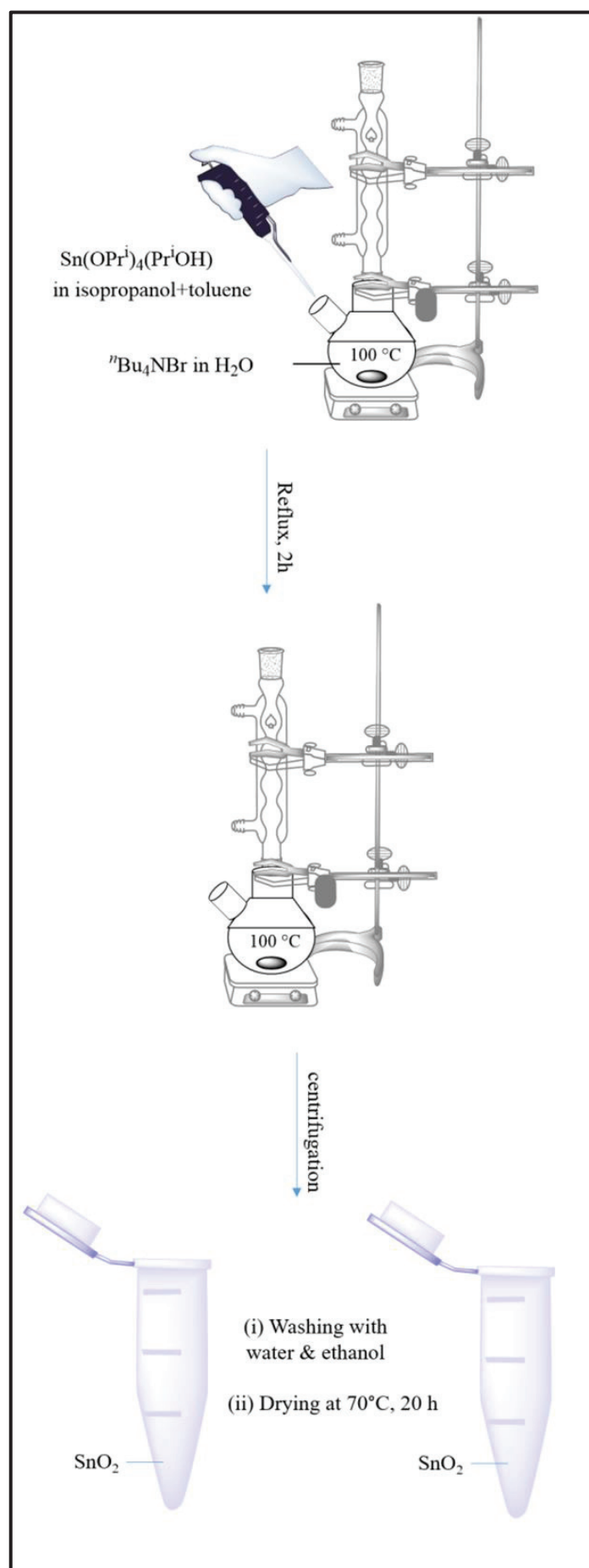


Figure 45 – Sol-gel synopsis to produce our SnO₂ nanoparticles. All the rights reserved to S. MISHRA.

4.1.2. The characterization at ambient pressure

In these experiments, no PTM was intentionally used to prevent further interactions with the samples. We must to introduce an additional interface energy term if we have an interaction between the PTM and the sample. The compression was non-hydrostatic, even though in nanoparticles, because of multiple contact points, the transmission of pressure is rather uniform.⁸⁰ The use of a PTM does not necessarily ensure hydrostaticity because nanoparticles have a tendency to aggregate and the PTM might not surround each nanoparticle. This point was discussed in ref. 37 to ZnO nanoparticles, in which we compared the pressure-induced phase transitions with methanol/ethanol mixture as the PTM and without a PTM. However, the lack of hydrostaticity is known to favor amorphization under pressure.¹⁹⁷ Even though, up to now, non-hydrostaticity has not been found to be a preponderant term in the amorphization of nanoparticles, it cannot be discarded with the available data.

a) Transmission electron microscopy (TEM)

Our experiments were realized at Lyon Saint-Etienne Microscopy Consortium (CLYM, FED 4092), which is a platform of the University Lyon1. The observations were carried out on JEOL 2010F transmission electron microscope (see Figure 46) equipped with a field emission gun (Shottky emission) and with the voltage acceleration set to 200 kV. Images in a high-resolution mode were acquired with an Orius 200 (Gatan) camera and they were processed using the free software ImageJ.

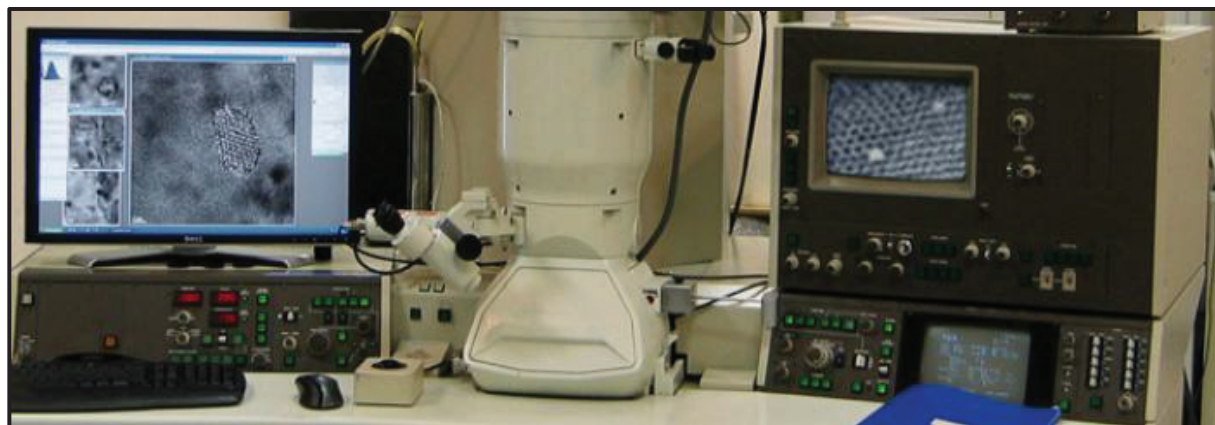


Figure 46 – Microscope JEOL 2010F FEG ¹⁹⁸

The morphology of the nanoparticles was examined by transmission electron microscopy (TEM) and they are showed in Figures 47a and Figure 47b. After analysis using ImageJ software, we can observe that the nanocrystallites have ~ 2–3 nm of diameter, they are well crystalized. In addition, the particles are dense and homogeneous.

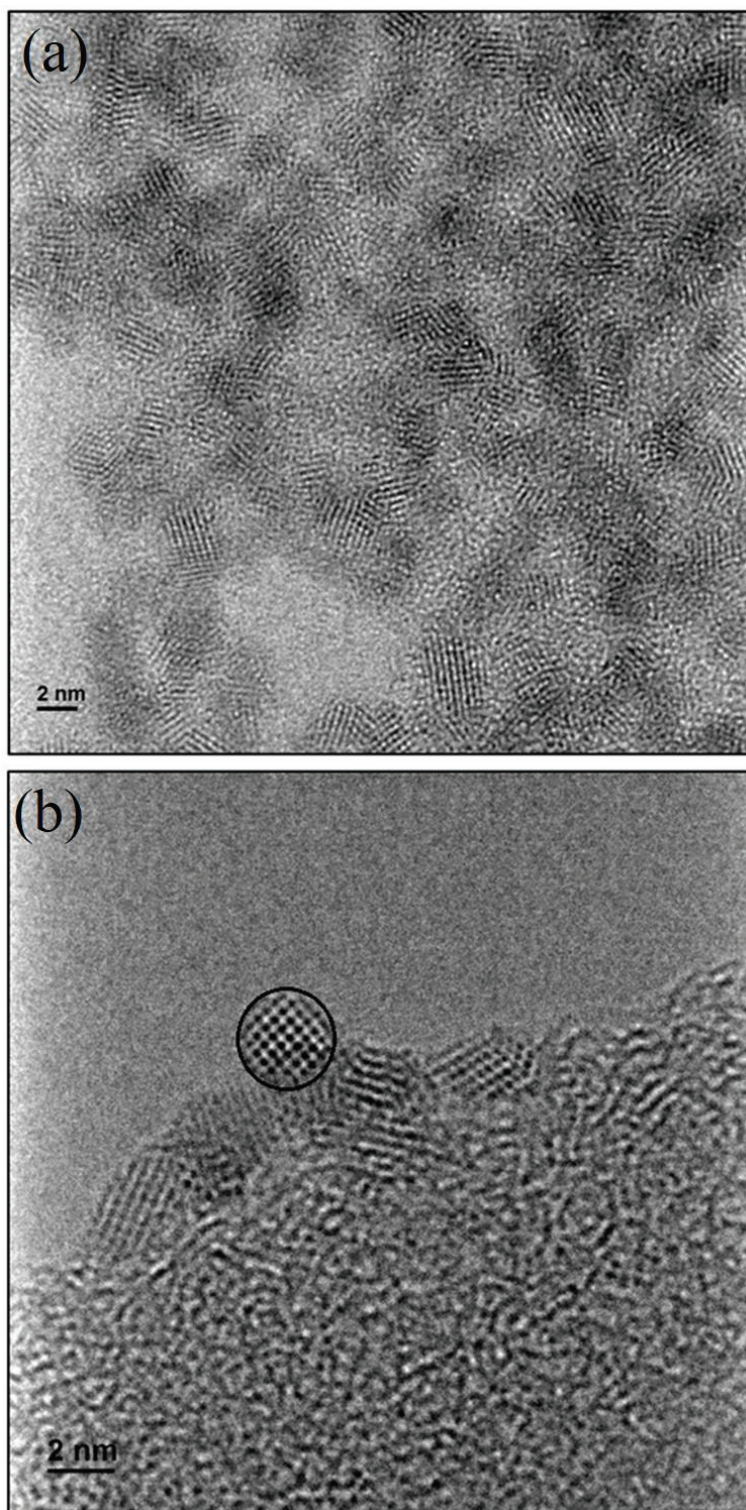


Figure 47 – (a) Transmission Electron Micrographs (TEM) of the as-prepared SnO₂ sample. (b) Zoom of image (a). Excellent crystallinity may be assumed from these images.

b) X-ray Diffraction (XRD)

The X-ray diffractions in our nanometric sample, produced by sol-gel were managed at the Henri Longchambon Diffractometry Center (CDHL – Centre de Diffractométrie Henri Longchambon).

The both XRD spectra – at ambient pressure and under high-pressure – were conducted using a microfocus Oxford Xcalibur Mova diffractometer (Figure 48), which operated using a beam of ≈ 150 micrometers in diameter and molybdenum (Mo) source. It is compatible with our Almax's diamond anvil cell (DAC) setup.

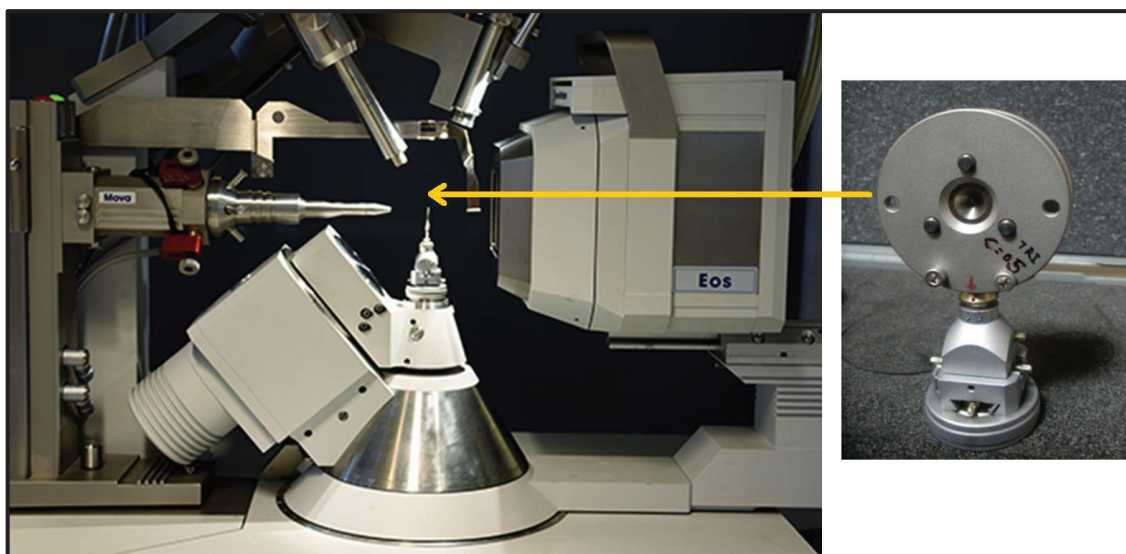


Figure 48 – (Left) Oxford Xcalibur Mova Spectrometer. (Right) DAC Almax's type on a support that allows it to arrange the DAC on the four circles of the diffractometer's goniometer.¹⁹⁹

The X-ray diffraction data show that the sample is a crystalline phase with a well-ordered atomic lattice, and may be indexed as cassiterite (rutile) structure with cell parameters $a \sim 4.74\text{\AA}$ and $c \sim 3.19\text{\AA}$, in agreement with the literature data (Figure 49).¹²¹ Such results (excellent crystallinity) were confirmed by electron microscopy technique. We must highlight that as these techniques are mainly sensitive to high-Z elements. Usually, they do not give sufficient information of defects in materials, such as oxides which are principally oxygen vacancies. Complementary techniques like optical spectroscopy, for example, are required to get access to the oxygen sublattice.

Using the Scherrer equation ($D = \frac{k\lambda}{\beta \cos\theta}$), we could find an average size of ~ 2.7 nm for these SnO₂ nanoparticles with no residual stress, and such value agrees with that one found by TEM.

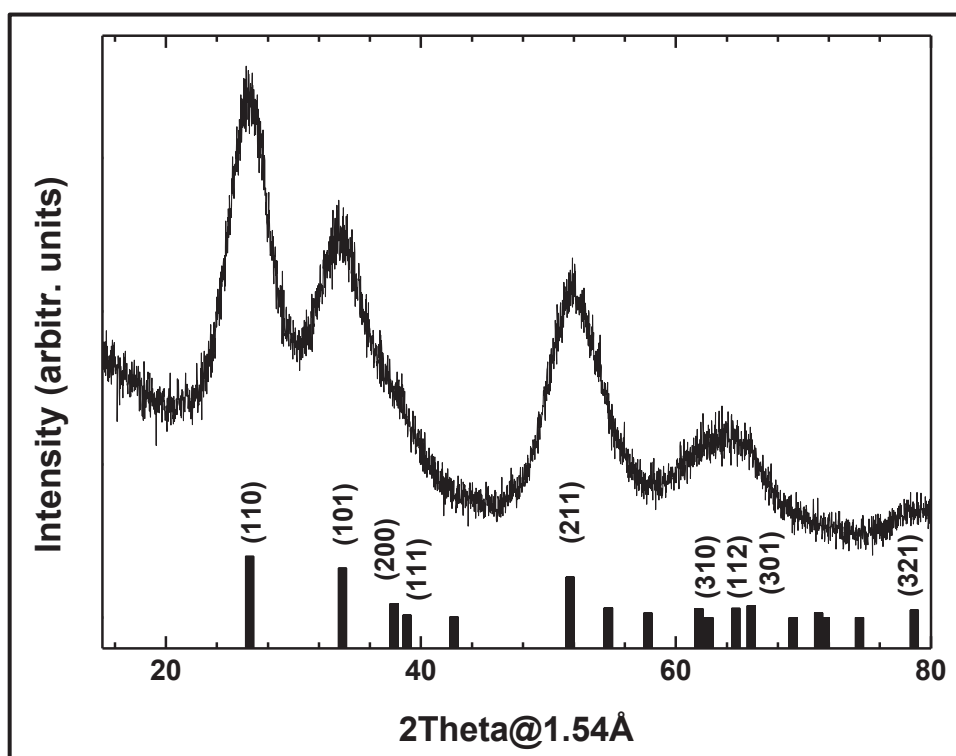


Figure 49 – X-ray diffraction pattern of the as-prepared SnO₂ sample. The peak positions and relative intensities of the rutile structure are plotted. The diffraction pattern may be indexed in this structure with usual cell parameters: $a \sim 4.74 \text{ \AA}$ and $c \sim 3.19 \text{ \AA}$.

c) Raman spectroscopy

Our Raman spectra, showed in Figure 50, were also collected using the Labram HR Evolution Spectrometer. We used the same features that those used in the powder and the single-crystal characterization, *i.e* we used as an excitation energy of 532 nm and, to avoid heating, the power, was set to 5 mW at the entrance of the DAC. The beam was focused on the sample by using a Mitutoyo 50x lens, with a beam diameter of $\sim 2 \mu\text{m}$ at the sample. The scattered light was collected in backscattering geometry using the same objective.

When comparing both SnO₂ bulks and nanocrystal spectra showed in Figure 50a, we can see that their Raman signature are strongly modified. Firstly, the nanoparticle peaks are much broader than those of bulk sample. Besides, the Raman peaks in the low-frequency modes (Lamb modes) do not exist for the bulk material, as mentioned in the precedent chapter.

Handling with SnO₂ nanoparticles, the measurement of additional low-frequency modes (below 100 cm⁻¹) is new and very important feature of the Raman spectrum. As highlighted in Chapter 2, these bands are due to confined acoustic vibrations and are attributed to spheroidal vibration modes of a spherical elastic body.²⁰⁰ From a classic point of view, the problem in the low-frequency region is often taken into account by considering the acoustic vibration of the particle as a whole.

The Lamb solution for a homogeneous, elastically isotropic continuum sphere, for which the frequency of the vibration is given by:

$$\omega = S_l v_l / dc \quad (12)$$

where v_l longitudinal velocity of sound in the bulk of the oxide ($v_l = 6.53 \times 10^5 \text{ cm} \cdot \text{s}^{-1}$); S_l is a coefficient that depends on the sound velocities (our case we took $S_l = S_{1,0} = 0.887$), d is particle size (diameter) and c is the vacuum light velocity.

The low-frequency Raman scattering probes to be very effective in providing the size of very small nanoparticles.¹¹⁹ Using this relation, we could determine the average diameter, which was estimated to be centered around 2.6 nm, in good agreement with the XRD pattern and TEM images. In addition to such information, Diéguez *et al.*¹¹⁹ showed by the deconvolution of the theoretical curve with low-frequency Raman spectra that the particle size distribution can be extracted. Such values were compared to size distributions obtained by Raman spectroscopy and by TEM measurements. The particle size distribution for our sample is shown in Figure 50b. We conclude that the particle size is mainly comprised between 2 and 4 nm.

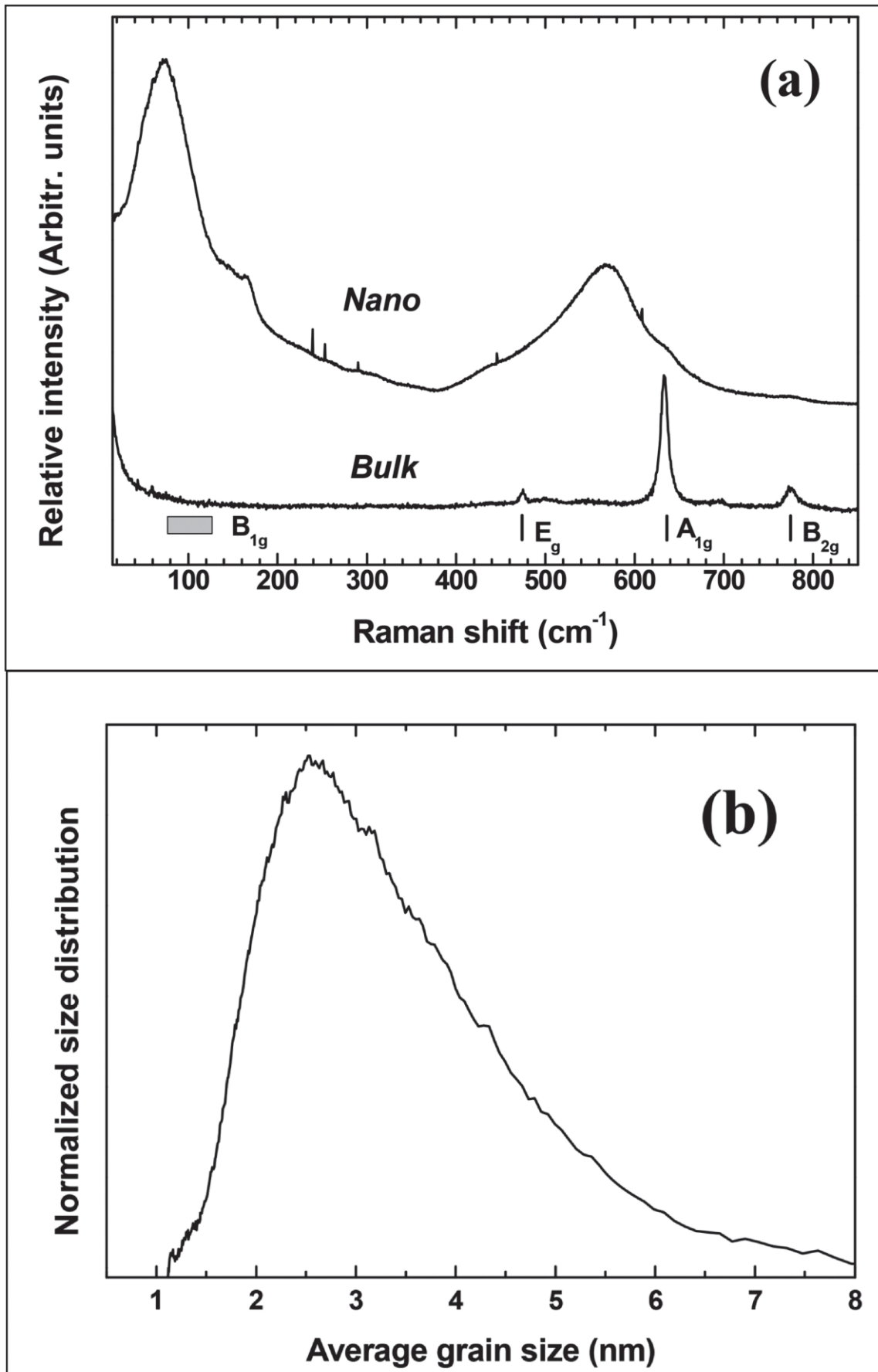


Figure 50 - (a) Raman spectrum of the SnO₂ nanoparticles used in this study compared to such one of a bulk sample. Ticks show the position of the Raman peaks in a bulk sample. (b) Size distribution of the particles deduced from the low-frequency peak.

4.1.3. The characterization at the high-pressure

a) X-ray diffraction

For these samples, we realized X-ray diffraction under high-pressure. SnO₂ nanoparticles were placed inside a 250 μm chamber drilled in an indented stainless-steel gasket, along with a ruby acting as a pressure gauge. To generate the high-pressure we used an Almax-type (DAC). The X-ray diffraction data are shown in Figure 51a. The SnO₂ nanoparticles were placed inside a 250 μm chamber drilled in an indented stainless steel gasket, along with a ruby acting as a pressure gauge³⁴. As it was highlighted in the begin of the chapter, we did not use pressure-transmitting medium (PTM) in this experiment.

Because of the size-induced broadening of the peaks, no subtle change can be analyzed during compression. For instance, the second-order phase transition to the CaCl₂-type is not detected. It requires larger particles and/or smaller beam size (to avoid the pressure gradient leading to an apparent coexistence of phases).¹³⁷ This result is consistent with previous works on nanoparticles of the same size.¹³⁶ It is worth noting at this point that the oxygen sublattice is hardly accessible through X-ray diffraction because of the low Z-contrast.

An equation of state (EoS) describes how the volume or density of a material varies with changes in pressure and temperature. It also defines how some of the elastic properties of the material change in response to compression and expansion. So, in order to analyze the pressure dependence of the volume (Figure 51b), the relative volume has been fitted using a second-order Birch-Murnaghan equation of state (BM) EoS²⁰² as shown below:

$$P = 1.5B_0[(V/V_0)^{-7/3} - (V/V_0)^{-5/3}] \times \{1 + 0.75(B'_0 - 4)[(V/V_0)^{-2/3} - 1]\} \quad (13)$$

where B_0 and B'_0 are the bulk modulus and its first pressure derivative, respectively, at ambient pressure.

The bulk modulus that defines the instantaneous volume variation with the pressure is given by:

$$K = -V(\partial P / \partial V) \quad (14)$$

As mentioned before, it was used $B_0 = 252$ GPa as a value to fit the pressure-induced variation of the low-frequency Raman mode, a satisfactory agreement between experimental data and this model equation of state was achieved.

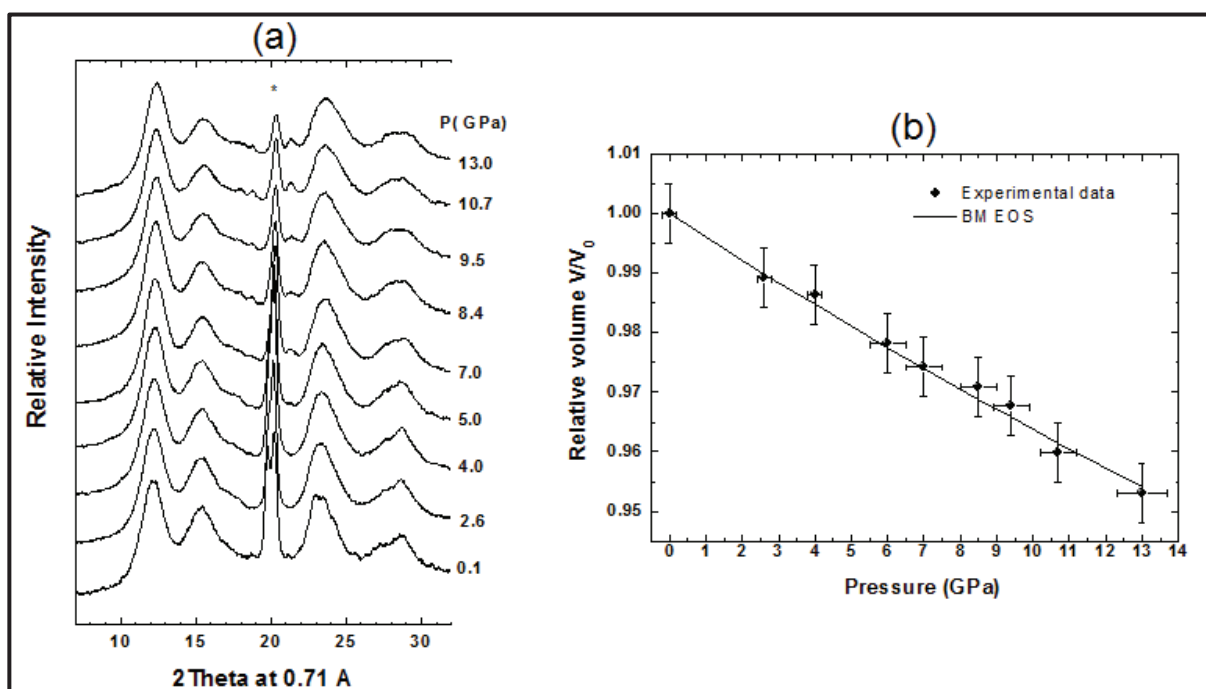


Figure 51 – (a) XRD diffraction patterns with increasing pressure. The asterisk shows the diffraction signal coming from the stainless-steel gasket. (b) The relative volume as a function of pressure (points) along with a second order Birch-Murnaghan equation of state (line) using $B_0 = 252$ GPa.

b) Raman Spectroscopy

The Raman spectra at high-pressure were done in continuation of the experiment at ambient pressure, consequently, under the same conditions. The signal was recorded by the LabRAM 6 software, while the software Fityk was used to decompose the experimental Raman spectra obtained. After subtracting the background, Raman peaks were simulated using Lorentzian and Gaussian functions. The high-pressure was generated using a Chervin-type DAC, as shown in the subsection 1.2.1. Another characteristic linked to the nanoparticles is the fact of the frequency of the peaks shifts toward larger frequencies when the average diameter of the particle decreases.

The low-frequency region

Figure 52a shows the low-frequency region of SnO₂ nanoparticles Raman spectra under high-pressure. At ambient pressure, we can observe two peaks: the main peak (P1) situated at $\sim 73 \text{ cm}^{-1}$ and the second one (P2) located at $\sim 166 \text{ cm}^{-1}$. P1 is related to confined acoustic vibrations, it was found that it shifts slightly to higher frequencies as pressure increases, and it was well fitted up to 12 GPa using a log-normal function. Such an expected outcome is due to the changing of the density and the elastic constants of SnO₂ with pressure increasing. P2 will disappear up to 7 GPa and above 12GPa another peak (P3) arises at $\sim 139 \text{ cm}^{-1}$. P1 and P3 will behave differently under pressure: while P3 increases in intensity and P1 decreases in it. At the highest pressure ($\sim 20 \text{ GPa}$), a component centered around 200 cm^{-1} (P3) has a similar intensity as the initial low-frequency peak P1. These changes happen simultaneously with a broadening of the high-frequency peaks and with the loss of the structuration of the Raman spectra, which will be detailed hereafter.

Calculating the breathing vibration frequency at all pressures is not an easy task. It requires the knowledge of bulk and shear modulus values at ambient pressure but also their pressure dependencies, and these values show some dispersion in literature. Haines *et al.*¹²¹ reported a bulk modulus of $205 \pm 7 \text{ GPa}$ and its pressure derivative were found to be 7.2 ± 2.0 . In another study, He *et al.*¹³⁶ found $B_0 = 252 \pm 10 \text{ GPa}$ for a fixed value of $B_0' = 4$. We tested different sets of B_0 and B_0' values to calculate the frequencies as a function of the pressure and we found an excellent agreement with the data obtained by He *et al.*¹³⁶ because our samples have almost the same size of theirs (Figure 52b). Haines and Léger⁹ worked with micrometric powder, so their values of B_0 and B_0' are not appropriated.

The pressure-induced shift of the peak (for the bulk, at ambient pressure) is related to the to the changes in both R , the radius of the particle, and v_l , the longitudinal sound velocity (R and v_l are supposed to be equal to nanoparticles and bulks).^{160,203} The pressure-dependence of the frequencies related can be expressed as^{160,203}:

$$v_l = \left(\frac{B + \frac{4}{3}G}{\rho} \right)^{1/2} \quad (15)$$

with

$$R = \left(\frac{3M}{4\pi\rho} \right)^{\frac{1}{3}}, \quad (16)$$

Where: B and G are bulk and shear moduli, respectively; ρ is the mass density; and M is the mass of a spherical nanoparticle.

Approximating our nanoparticles to Lamb's conditions, *i.e.*, considering that our nanoparticles are homogeneous, elastically isotropic and continuous spheres, it will be possible to calculate the vibrational frequencies. The frequency of the spheroidal vibration S_l will be proportional to v_l/R .²⁰³ The proportionality constants can be discarded. Thus,

$$S_l \approx \frac{v_l}{R} \quad (17)$$

Taking equation 16 and 17, we arrive at:

$$S_l \approx \frac{\left(\frac{B + \left(\frac{4}{3}\right)G}{\rho} \right)^{\frac{1}{2}}}{\left(\frac{3M}{4\pi\rho} \right)^{\frac{1}{3}}} = \left(\frac{B + \left(\frac{4}{3}\right)G}{\rho} \right)^{\frac{1}{2}} \left(\frac{4\pi\rho}{3M} \right)^{\frac{1}{3}} = \left(\frac{4\pi}{3M} \right)^{\frac{1}{3}} \frac{\left(B + \left(\frac{4}{3}\right)G \right)^{\frac{1}{2}}}{(\rho)^{\frac{1}{2}}} (\rho)^{\frac{1}{3}}$$

$$S_l \approx \left(B + \left(\frac{4}{3}\right)G \right)^{\frac{1}{2}} (\rho)^{-\frac{1}{6}} \quad (18)$$

So, to spheroidal vibration peak, the pressure-dependent factor in the position of the Raman peaks is therefore $\left(B + \left(\frac{4}{3}\right)G \right)^{\frac{1}{2}} (\rho)^{-\frac{1}{6}}$.

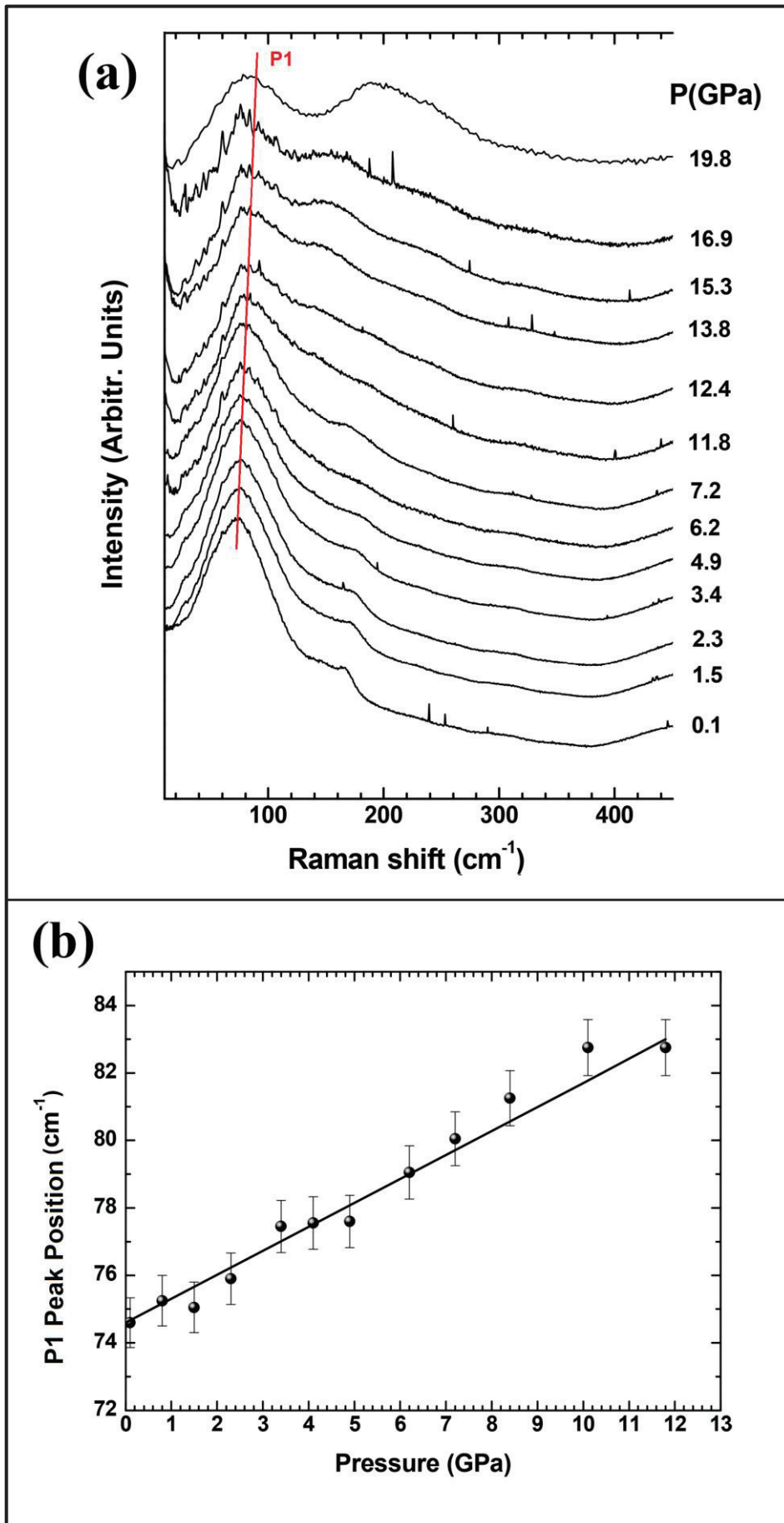


Figure 52 – (a) Pressure-induced evolution of the low-frequency range. (b) Low-frequency peak position (P1) as a function of pressure along with the calculated variation (black line) using B_0 and B_0' values reported by He et al.¹³⁶

The high-frequency region

Now, let us analyze the high-frequency region of the Raman spectra of the SnO₂ nanoparticles under high-pressure. Figure 53 shows the pressure-induced evolution of the Raman spectra in the range 100 cm⁻¹ to 850 cm⁻¹. The high-frequency region was fitted using a minimal number of functions to reproduce the spectra and five Gaussian components were enough to model the spectra and to analyze the pressure-induced evolution.

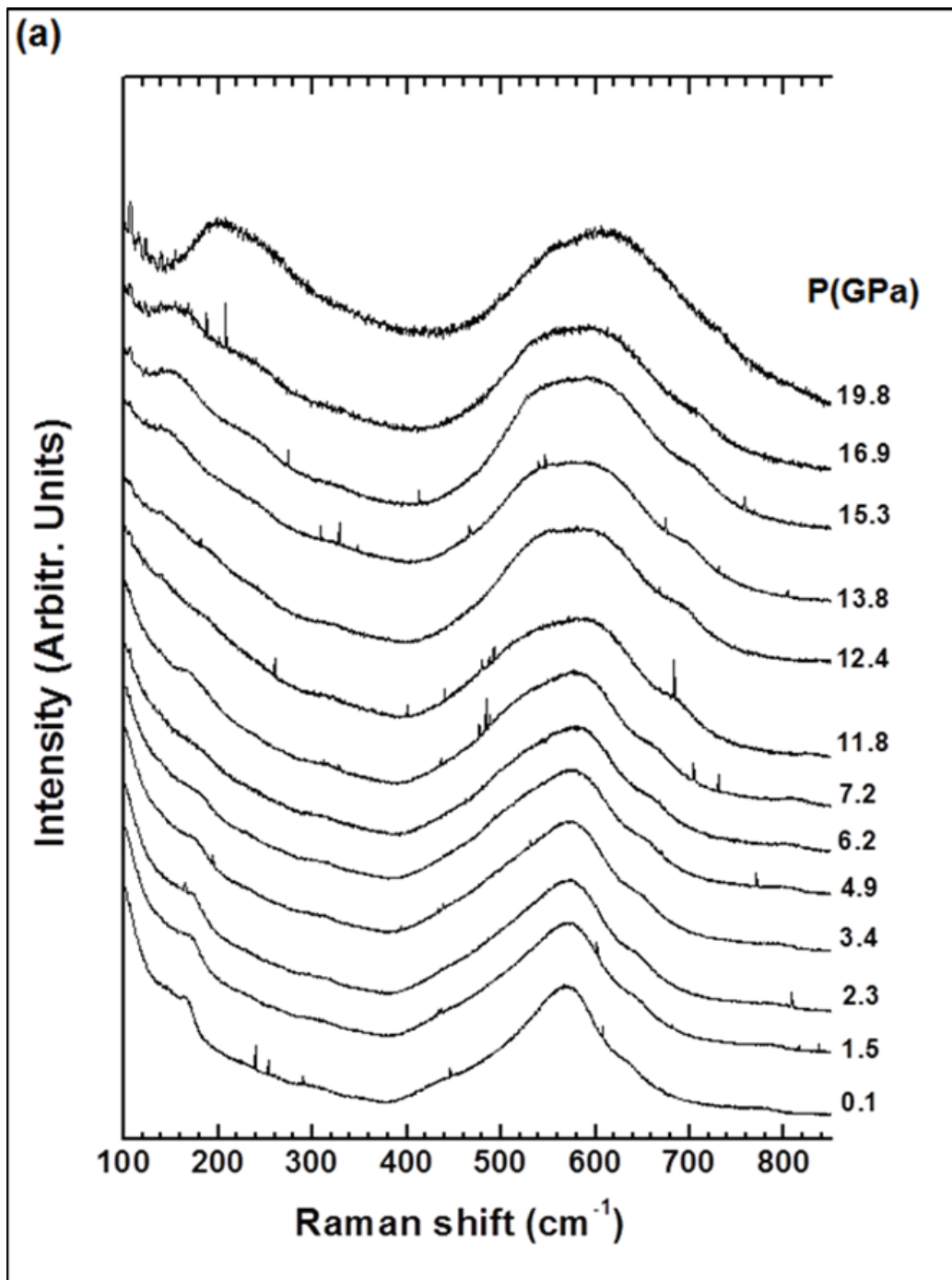


Figure 53 – Raman spectra of SnO₂ nanoparticles with increasing pressure.

Their pressure dependencies are plotted in Figure 54 below.

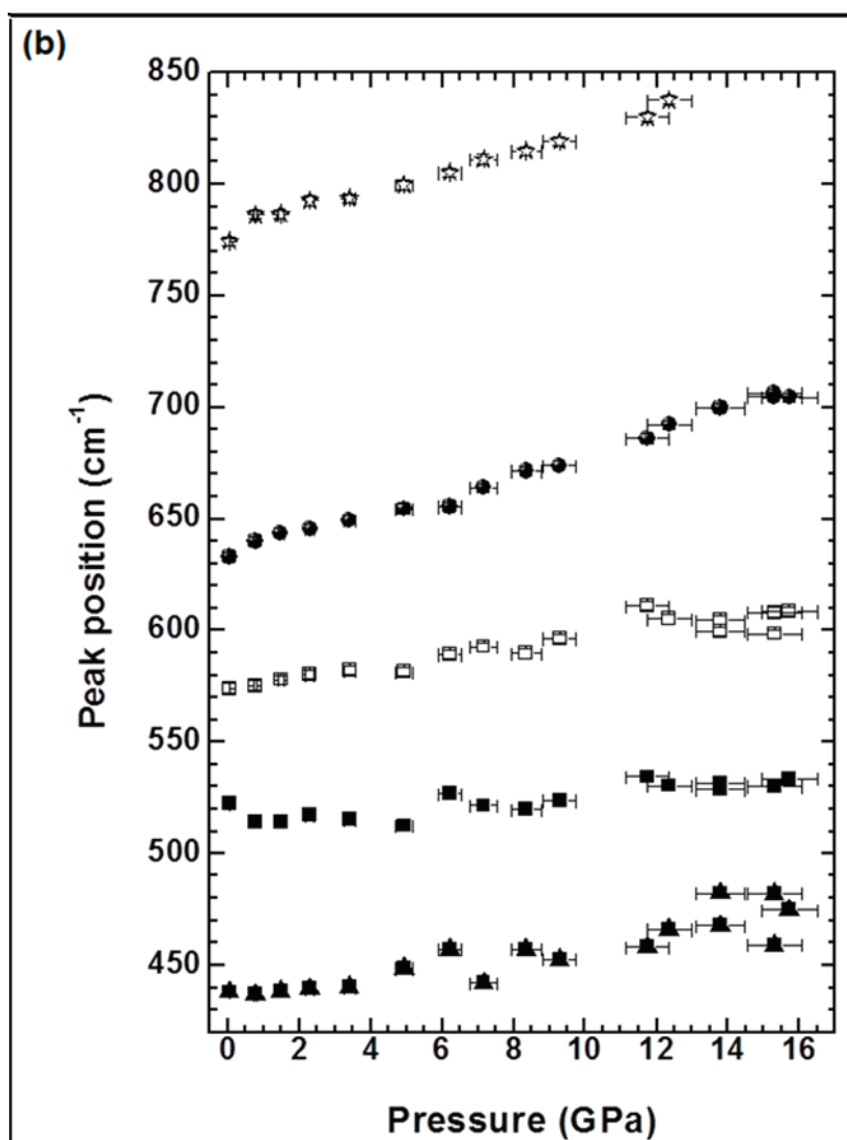


Figure 54 – Pressure-induced evolution of the centers of the Gaussian functions used to fit the Raman spectra.

The slopes of $\nu(P)$ are indicated in Table 4.

Table 4 – Peak position at ambient pressure and their pressure dependencies

Initial Peak Position (cm ⁻¹)	Slope ($\nu(P)$) (cm ⁻¹ . GPa ⁻¹)
774(1)	4.0(1)
633(1)	4.6(1)
575(1)	2.1(2)
515(1)	1.1(2)
434(1)	2.5(3)

Two peaks are related to the ones observed in bulk samples. The peak situated at $\sim 633 \text{ cm}^{-1}$ corresponds to the A_{1g} mode (slope of $\nu(P) = 4.9 \text{ cm}^{-1} \cdot \text{GPa}^{-1}$ in bulk) and the other one lied at 774 cm^{-1} corresponds to the B_{2g} mode ($\nu(P) = 5.4 \text{ cm}^{-1} \cdot \text{GPa}^{-1}$ in bulk). Additional modes have been proposed as result from the surface and disorder.

A change in the general shape of the broad features ranged between 400 and 800 cm^{-1} can be seen above 7.2 GPa, agreeing with the *ab initio* simulations which will be described in the next subsection. At pressure higher than 13.8 GPa, new features between 200 and 300 cm^{-1} start to emerge in the spectra. It is difficult to relate these changes to a transition to the CaCl₂-type structure even though this transition should occur in this pressure range. At 19.8 GPa, two broad features ($\sim 200 \text{ cm}^{-1}$ and $\sim 600 \text{ cm}^{-1}$) are observed. The organization initially present in the spectra had disappeared and amorphous-like spectra are observed in accordance with the spreading of the Sn-O distances, that will be shown in Figure 57 (*ab initio* simulations).

Figure 55a shows the Raman spectra upon decompression. A reversibility of the pressure-induced transformation can be inferred. It is worth noting that the low-frequency peak position after pressure release is slightly shifted to the low-frequency side (Figure 56a). It looks like that the average particle size increased during the compression (Figure 56b). However, a potential source of frequency variation (and then that of this apparent size variation) could be the change in the shape of the nanoparticles under pressure associated with a plastic deformation, for instance, and/or residual mechanical stresses affecting the mechanical properties.

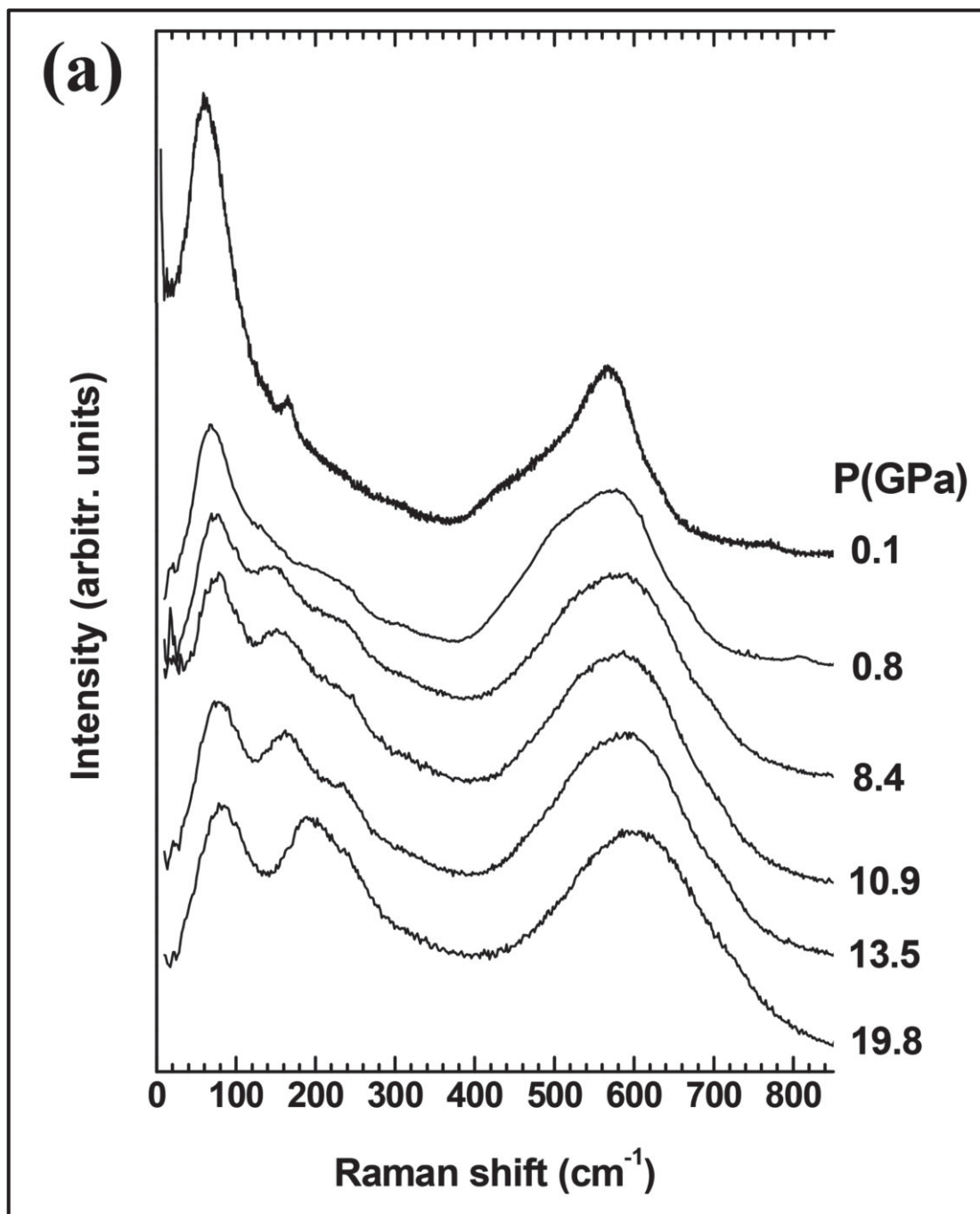


Figure 55 – Raman spectra upon decompression showing the reversibility of the pressure-induced transformations.

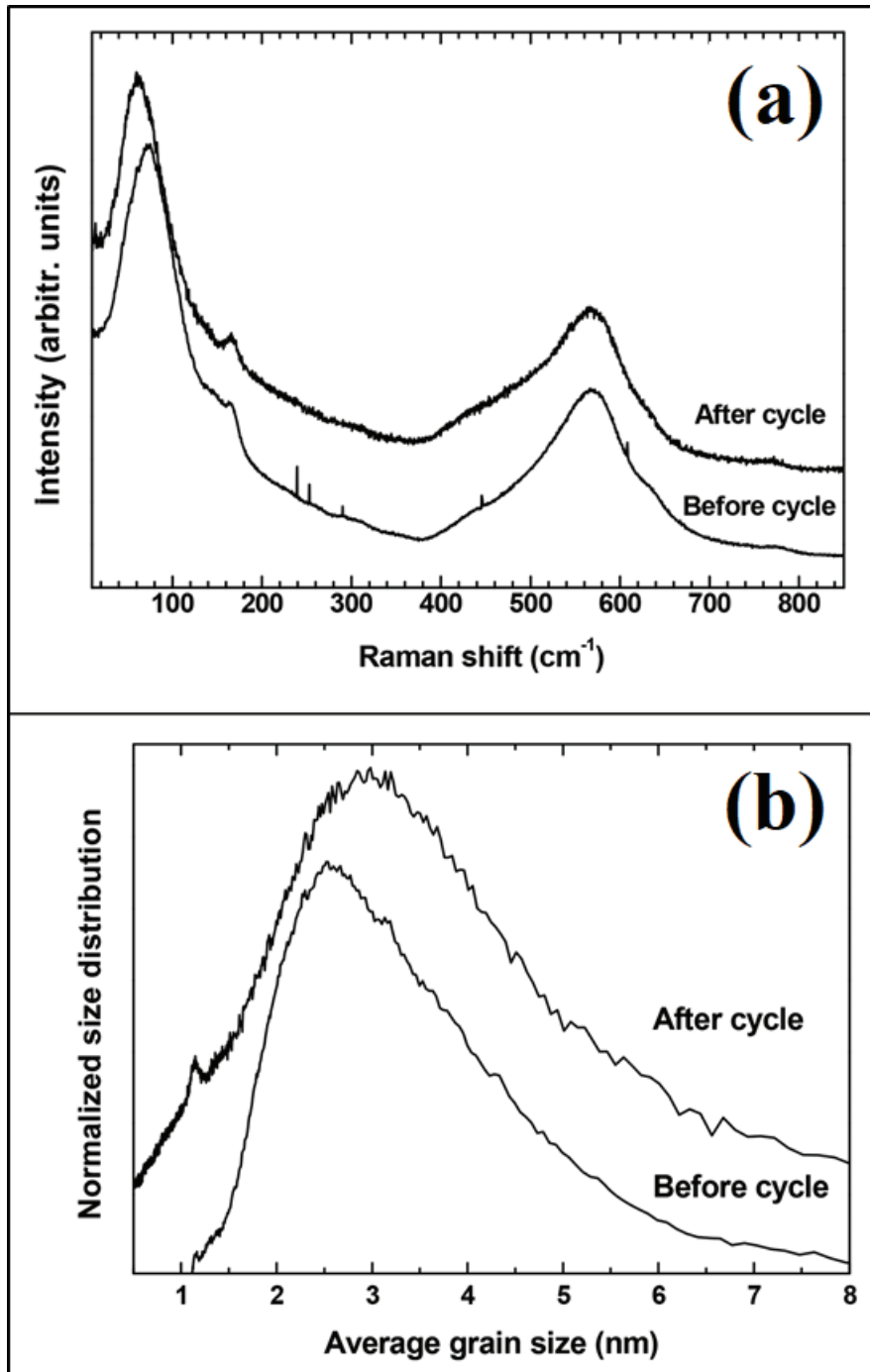


Figure 56 – (a) Raman spectra before and after the pressure cycle. (b) Distribution of the particle size using the low-frequency region of the Raman spectra before and after the pressure cycle.

c) The *ab-initio* Simulations

Ricardo A. Casali and Maria A. Caravaca, from the Universidad Nacional del Nordeste in Argentina, performed sophisticated *ab initio* simulations on a system similar to that one used in our experiments. They used a particle with a diameter of ~2.8 nm containing 984 atoms in order to better understand the interface impact on the system evolution under pressure, and to obtain more structural information about the pressure-induced changes.

Density Functional Theory (DFT) and its implementation in several electronic structure codes have proven to be reliable tools to study the solid-state bulk and small aggregate of atoms (clusters) with defects, surfaces, and interfaces. Recent developments of localized *ab initio* implementation of DFT by means of pseudo-potential and localized atomic wave functions were introduced in SIESTA code.²⁰⁴ This flexible implementation allows the study of systems in bulk¹⁵⁸ and in aperiodic systems with a larger number of atoms than in other methods. In that study for the search of minimum energy structure of each particle, an annealing method with finite variable temperature technique improved the conventional conjugate gradient method.

An example of this capability is a recent study of the stability and thermodynamic properties of SnO₂ nanoparticles that included up to 1309 atoms.²⁰⁵ In that study, the surface formation energies and thermodynamic stabilities of nanoparticles were estimated as functions of O₂ pressure and temperature. In addition, the electronic properties of the surfaces, formation of complexes, and details about the relaxations of atoms inside, close to, and at the surface of the nanoparticles were investigated. These electronic, structural, and physicochemical properties were correlated with the changes in the nanoparticle stoichiometry. In that study, for the search for the minimum-energy structure of each particle, an annealing method using a technique with a variable finite temperature improved on the conventional conjugate-gradient method.

Our study is an extension of Ponce *et al.* work.²⁰⁵ However, we target the pressure and the temperature of Parrinello-Rahman technique^{206,207} together with a Nosé thermostat. The time step was fixed between 1 and 3 femtoseconds, and the number of steps was in the order of at least 2000, making a total relaxation time of at least 3 to 6 picoseconds.

4.2. Discussion

SnO₂ nanoparticles of ~2-3 nm have been investigated at ambient and at under high-pressure, both experimentally using TEM, Raman spectroscopy, X-ray diffraction, and numerically by *ab initio* simulations.

These kinds of nanoparticles have also been studied using powder X-ray diffraction (PXRD). However, only recently, the first report of a complete high-pressure study¹⁶⁰ of SnO₂ nanoparticles using Raman spectroscopy has shown a pressure-induced disordering of the anionic sublattice.¹⁶⁰ Contradictorily, PXRD on particles of this size concluded that no important structural changes can occur at pressure as high as 30 GPa,²¹ indicating that the transition pressure to the high-pressure cubic phase is drastically shifted due to the size effect.

Figure 47 shows the transmission electron micrograph (TEM) of an assembly of SnO₂ nanoparticles with an average size of 2–3 nm. Our results are in good agreement with those obtained with a high-resolution transmission electron micrograph (HRTEM) by Pinna *et al.*,²⁰⁸ *i.e.*, high crystallization, quasi-spheroidal particle, etc.

Raman spectroscopy seems to indicate a pressure-induced amorphization as the spectra above 19.8 GPa resembles the ones of amorphous samples. However, this is in apparent contradiction with the conclusions obtained by X-ray diffraction. Therefore, to explain this seeming paradox, we interpreted our observations as a disordering in the oxygen sublattice.

In order to provide complementary information, we combine our Raman spectroscopy data to the *ab initio* simulations. A first stage, from ambient pressure to 6 - 7 GPa, does not show noticeable changes. At higher pressure, the disorder, initially located at the surface of the particles, starts to propagate to the core of the nanoparticles. Spectra at high-pressures are very similar to the ones of an amorphous state indicating a possible pressure-induced amorphization (PIA). This seems to be in contradiction with X-ray diffraction data on SnO₂ that has never reported PIA whatever the nanoparticles size and the synthesis routes. However, the seeming paradox can be explained by the chemical selectivity associated with both experimental techniques. X-ray diffraction is affected by the heaviest atoms (Sn in this case) whereas Raman spectroscopy is mainly sensitive to the oxygen sublattice, particularly in the case of a

rutile-type structure where the Raman-active modes only involve oxygen displacements. Such sublattice disordering has already been reported,¹⁹⁷ in particular in Eu₂(MoO₄)₃.¹⁷⁰ In compounds with a high contrast on the Z of the constituent atoms (such as some oxides), the combination of different characterization techniques is required to obtain complementary information on the structure and its evolution.

We can see the results of the *ab initio* simulations in Figure 57. We could study the internal order of the particle through the Radial Pair Distribution Function ($g(r)$) for the two atomic species Sn and O, as can be seen on Figure 58.

At $P = 0$ GPa, the nanoparticles are characterized by a slight disorder at the surface but with a well-ordered core. However, such a situation changes under high-pressures and the disorder which was initially located at the surface, increases significantly above 6 GPa. Such behavior can be deduced from the spreading of the Sn-O distances.

Under pressure, the O-O pair distance became reduced and, the two peaks located at 2.58 and 2.92 Å change their distribution towards only one broad peak, located near 2.6 Å at 19 GPa. Similar behavior is found for Sn-Sn pairs, with peaks in the $g_{\text{SnSn}}(r)$ distribution located at 3.26 and 3.73 Å merging into one broad peak located near to 3.4 Å at 19 GPa. This could be due to a distorted lattice including a possible phase transition to a high-density phase like a distorted fluoride structure, e.g. the $Pa\bar{3}$ (pyrite) phase, or α -PbO₂¹²¹ in some part inside the nanoparticle. Interestingly, the inner core of the nanoparticle remains in the rutile structure (being not so much distorted) at all range of pressures.

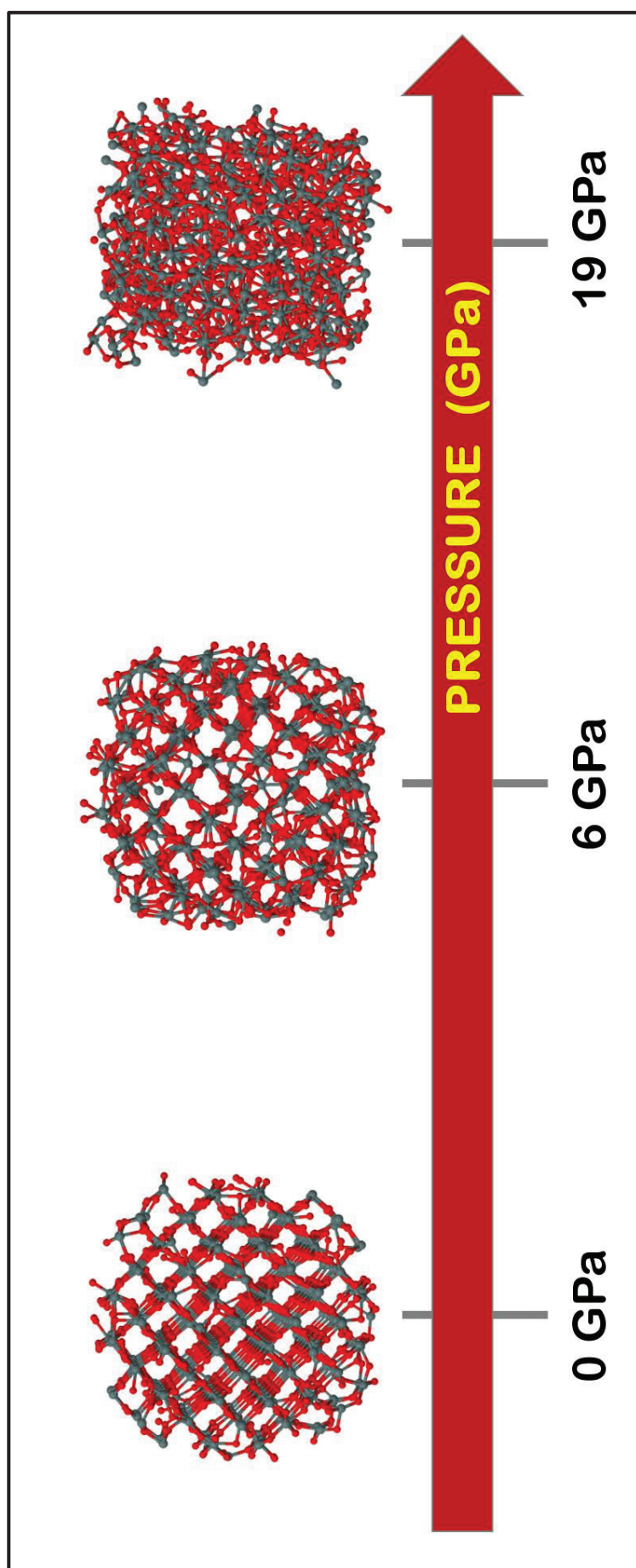


Figure 57 – Snapshots obtained by *ab initio* simulations of a particle with a diameter of 2.8 nm (984 atoms) at different $P = 0, 9$ and 19 GPa.

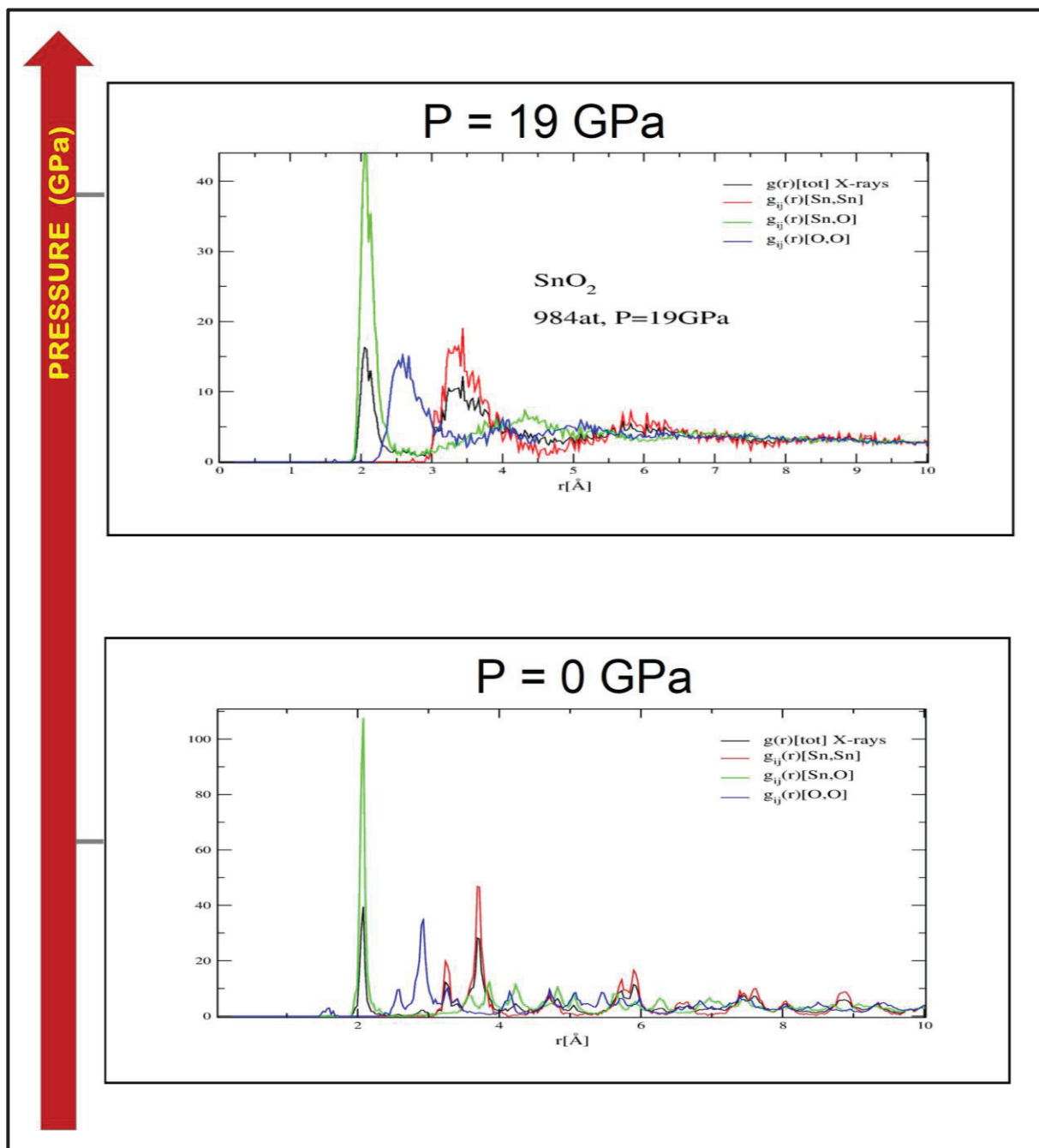


Figure 58 – The internal order of the particle can be studied by means of the Radial Pair Distribution Function ($g(r)$), for the two-atomic species Sn and O.

This broadening of the Raman spectra for pressures between 7 and 12 GPa may be related to the increase of disorder of the shells of nanoparticles. At higher pressures, new features are observed. The combination of the phase transitions (to the CaCl₂-type structure at P~12 GPa and to the pyrite-type structure at P~19 GPa), of disordering, and of nanosize effects leads to a Raman spectrum resembling vibrational density of states and is similar to an amorphous-like spectrum.²⁰⁹

However, another hypothesis may be invoked. First, this may be due to the fragmentation of the nanoparticles in smaller domains due to the first-order nature of the transition to the cubic phase. The new peak located at around 200 cm⁻¹ would be of the same nature as the peaks at ~ 75 cm⁻¹ (acoustic vibrations of the particles considered as an elastic medium) but for smaller particles. However, the Raman signal almost reverses when pressure is brought back down, particularly the position of the low-frequency spheroidal mode is inversely proportional to the particle size (Figure 55(a)). This observation rules out the hypothesis of the fragmentation of the nanoparticles in smaller domains as such a phenomenon would be irreversible. Secondly, the peak centered around 200 cm⁻¹ in the amorphous-like spectra has been assigned to vibrations of sub-stoichiometric SnO_{2-y}. Such decomposition effect is indeed invoked to describe the amorphous state as an intermediate; kinetically hindered state as in the case of SnI₄²¹⁰. However, here again, reversibility rules out this possibility as the enthalpy to form SnO₂ is very big so there is no chance to redo it. It is impossible to reformulate the basic components. The reversibility upon the pressure release may be due to either the relaxation of mechanical stresses or a structural reversibility from cubic to rutile initiated by the core of the nanoparticles remaining in the rutile-type structure, according to the simulations and acting as a nucleus for the back transformation.

General Conclusion

What is the main conclusion?

We presented in this thesis a complete study of the pressure-induced disorder in the SnO₂, going from the bulk (in all its forms: powder and single-crystal) to the nanoparticles, mainly using Raman spectroscopy. As well as this technique, X-ray diffraction (XRD) was used on the high-pressure experiments. On the one hand, the XRD is mainly affected by the heaviest atoms (Sn in our case), and on the other hand, the Raman spectroscopy is more sensible to the oxygen sublattice. Both characterization methods are complementary, principally because they probe different sublattices. Until now, no study about the amorphization of the SnO₂ under pressure using XRD was reported. However, recently, Girão et al.²¹¹ studying SnO₂ under pressure, and using Raman spectroscopy, developed an original model in which only the anionic sublattice amorphized. The development of such framework based on the decoupling of the sublattices was possible thanks to the behavior's difference between XRD and Raman. So, it was possible to perceive that such amorphization concerned only the anionic sublattice.

Defects vs. hydrostaticity influence on the high-pressure transition

It has been showed that the density of defects is an important parameter to be considered in the phase transition from a crystalline to an amorphous phase.²³ On the one hand, analyzing powder and single-crystal at high-pressure, we found that while the powder having an initial concentration of defects showed a Raman spectra that resembled a vibrational density of state at quite low pressure; a single crystal presenting a low density of defects showed a sequence of polymorphic transitions without drastic broadening. On the other hand, when dealing with nanoparticles, we did not perceive noticeable changes from ambient pressure to 6-7GPa. However, at higher pressures, the disorder located at the surface of the particles started to propagate to the core of the nanoparticles. Their Raman spectra obtained at high-pressure seemed to those of an amorphous state, suggesting a possible pressure-induced amorphization (PIA).

As well as the density of defects, it is known that nonhydrostaticity also can leads a crystalline structure to an amorphous state ^{212,173,213}. Based on such studies, we realized an investigation on our samples in order to verify the importance of such parameter.

Firstly, we used paraffin oil as the pressure transmitting medium (PTM) on the single crystal experiments, guarantying the hydrostaticity up to ~ 3 GPa. We found that the change in the slope of $\nu(P)$ agrees with the lowered transition pressure, and such effect was inferred to the effect of the nonhydrostaticity stress components.

Secondly, to check such effect on powder samples, we loaded an experiment using a 4:1 methanol: ethanol mixture as PTM, ensuring a hydrostatic compression up to 10 GPa. The Raman spectra obtained under pressure was similar to that one obtained without PTM. The main difference lied in the relative intensity between the low-frequency and the high frequency regions at high-pressure. Thus, even compressing a powder sample with a PTM that provides good hydrostaticity, an amorphouslike signature could be verified because of the intergrain contact induces the shear stresses.¹⁷⁴

Finally, in the last experiment, we do not use PTM. This choice was motivated because, in nanoparticles, its use does not ensure the hydrostaticity. Nanoparticles tend to aggregate and the PTM might not surround each one of them. The compression was nonhydrostatic, even though in nanoparticles, due to the multiple contact points, the transmission of the pressure was rather uniform.⁸⁰ All these experiments show how easy is to find, in the literature, results which are in discordance

So now? How did we apply these influences our model?

Particularly in the case of the SnO₂, all of its properties are very influenced by the concentration of the defects in both bulk and nanoparticle form. So, the SnO₂ was found to be very adequate to test such influence under pressure. Additionally, the tin dioxide has a rutile structure (in ambient conditions) which is particularly adapted to the studies of decoupled sublattices. However, considering that an amorphization signature are never been observed when using X-ray diffraction, it raises the question about the choice of the most appropriate characterization technique. While the XRD experiments reported a sequence of structural phase transitions in bulks, Raman spectroscopy detected a sublattice disordering, as only the oxygen atoms move⁹ in the Raman-active vibrational modes, inclusive under high-pressure.

In this way, we had been interested in understanding for what reasons SnO₂ does not show amorphization if its “column neighbor” (which have the same valence number) from the periodic table, Si (SiO₂) and Ge (GeO₂) show it.

In order to verify if such peculiarity was related to atomistic or structural reasons, we created a new framework to apply to this unique system: the decoupling of the sublattices under pressure, considering only a “partial” pressure-induced disorder of the oxygen sublattice.

We observed a correlation between the defect density initially present in the samples and the selective disordering in SnO₂ upon compression. Such linkage was explained and discussed by the invasive percolation theory.

Considering that only the oxygen sublattice present sub-stoichiometry and defects, thus the transition from the crystal to the amorphous phase will be conducted by such sublattice. In our case, we used the invasive percolation theory was applied in order to analyze only the oxygen sublattice amorphization. The cationic sublattice seems to be resistant to the amorphization. Such resistance to PIA (only one sublattice amorphized) may be extended to other examples. For instance, no PIA has been reported in ZnO.

Generally, a crystallographic description of a structure relies on the packing of fundamental building blocks usually taken as a cation-centered polyhedron. The “traditional” picture implicitly assumes strong coupling between cationic and anionic sublattices, an idea that is questioned by our results where disordering occurs in a sublattice without implications for the cations. Non-close packing of silicon atoms would lead to pressure-induced transformations in both sublattices. In addition, sublattice disordering in SnO₂ questions the effects of the defect density in the observation of PIA in SiO₂ and GeO₂. For instance, in SiO₂, depending on the sample form and on the hydrostaticity conditions, an amorphous state may be observed.^{212,213} The transition to the stable high-pressure rutile-type form (stishovite) requires a major rearrangement of both cation and anion sublattices, giving rise to competition between the amorphous form and crystalline phases. An initial defect density may thus favor a disordering of the anionic sublattice that induces a destabilization of the quartz structure contrary to SnO₂, where the cationic sublattice remains ordered.

Perspectives

We realized that it would be interesting to obtain some TEM micrographs after compression, even knowing that it is difficult to recuperate these samples after compression. These TEM micrographs could serve to correlate TEM and low-frequency Raman spectra. This is an actual project but cannot properly be done with such small nanoparticles.

Further works on nanoparticles, using helium as the PTM, are required to determine whether the SnO₂ sublattice disordering might be related to the lack of hydrostaticity. Additionally, new experimental works using EXAFS measurements, in order to proof our model, can be developed by our data and our conclusions.

Appendix

A.1. Physical principles of Raman spectroscopy	120
A.2. Lamb explanation for the origin of low-frequency vibrations	122
A.3. Published works	125

A.1. Physical principles of Raman spectroscopy

As discussed in section 1.3.2(b), when an electromagnetic wave reaches a material, its oscillating electric field prints off the constituent ions, generating moments of oscillating dipoles that influence the electric susceptibility and, consequently, the polarization of the material. The harmonic modulation of polarization is the source of the emission of electromagnetic radiation, just as in the case of an antenna. The expression for the polarization of the medium,²¹⁴ modified by the incidence of radiation can be given by:

$$\mathbf{P} = \vec{\chi}_0 \cdot \mathbf{E}_0 e^{i(\mathbf{k}_i \cdot \mathbf{r} - \omega_i t)} + \mathbf{E}_0 \cdot \mathbf{u}_0 e^{i[(\mathbf{k}_i \pm \mathbf{q}) \cdot \mathbf{r} - (\omega_i \pm \omega_0)t]} \frac{d\vec{\chi}}{du} + \frac{1}{2} \mathbf{E}_0^2 \cdot \mathbf{u}_0^2 e^{i[(\mathbf{k}_i \pm 2\mathbf{q}) \cdot \mathbf{r} - (\omega_i \pm 2\omega_0)t]} \frac{d^2\vec{\chi}}{du^2} + \dots, \quad (19)$$

Where $\vec{\chi}$ is the electric susceptibility tensor of the medium; \mathbf{E}_0 is the amplitude vector of the electric field; \mathbf{u} is the displacement relative to the equilibrium position of the atomic centers and \mathbf{q} the wave vector; \mathbf{k} , \mathbf{r} and ω are: the wave vector, the displacement vector and the angular frequency of the electromagnetic wave oscillation, respectively. Rayleigh scattering occurs when the oscillating polarization has the same frequency as the incident radiation. In equation (14) above, the first term of the equation refers to the elastic scattering of light; the second member represents the first-order anti-Stokes (+) and Stokes (-) Raman scatters, respectively, when the frequency of the oscillating system is increases or decreased by ω . The third term of Eq. (14) refers to second-order Raman scattering – in which the frequency change process is more pronounced – and so on.

In classical Raman spectroscopy experiments, assuming the use of visible light ($\lambda=500$ nm), the incident and the scattered radiation moments will be in the order of 10^5 cm⁻¹. This value is much smaller than the typical extension of the Brillouin Zone of most materials ($q \leq 2\pi/a_0 \leq 10^8$ cm⁻¹). Thus, the first-order Raman scattering involves only oscillations with moments near the center of the Brillouin Zone, i.e., $q \cong 0$.

A.1. Physical principles of Raman spectroscopy

The intensity of scattered radiation is proportional to the square of the induced polarization and depends on the polarization of scattered light \hat{e}_s of the form $|\mathbf{P}_{ind} \cdot \hat{e}_s|^2$. Using the approximation that $q = 0$ and denoting the polarization of the incident light by \hat{e}_i , the intensity of the scattered light in the first order I_S can be written as

$$I_S \propto \left| \hat{e}_i \cdot \left(\frac{d\bar{\chi}}{d\mathbf{u}} \right)_{q=0} \mathbf{u}(\omega_0) \cdot \hat{e}_s \right|^2. \quad (20)$$

Making $\hat{u} = \mathbf{u}/|\mathbf{u}|$ parallel to the direction of the atomic displacement, we can define the *Raman tensor* \vec{R} as

$$\vec{R} = \left(\frac{\partial \bar{\chi}}{\partial \hat{u}} \right)_{q=0} \hat{u}(\omega_0) \quad (21)$$

Thus, the intensity of scattered light can be written as

$$I_S \propto |\hat{e}_i \cdot \vec{R} \cdot \hat{e}_s|^2, \quad (22)$$

It can be seen from the equation (16) that the Raman tensor \vec{R} depends on the symmetry of the atomic oscillations that modify the polarization of the medium. This tensor can be obtained through the matrix of an irreducible representation of the crystal symmetry.

Since the Raman tensor for a specific oscillation is known and since the scattered radiation intensity is not zero - for a given combination of polarization between the incident and the scattered light, we say that the mode of vibration is Raman active, i.e, this vibrational mode is accessible by Raman scattering. On the other hand, since the intensity of the light coming from the dispersion process involving a certain mode of vibration is zero, the mode is not active. The Equations (16) and (17) shows that the Raman activity depends on the direction of propagation of the oscillations dictated by the Raman tensor and the dispersion geometry, that is, the polarization and direction of the incident and scattered radiation. This set of combinations that considers the dispersion geometry is called the Raman selection rules.

A.2. Lamb explanation for the origin of low-frequency vibrations

A theoretical explanation for the origin of low-frequency vibrations was first introduced by Lamb²¹⁵, for a homogeneous, elastically isotropic continuum sphere. Such theory begins with a motion's equation for a three-dimensional elastic body, which is given by:

$$\rho \frac{\partial^2 \mathbf{D}}{\partial t^2} = (\lambda + \mu) \nabla (\nabla \cdot \mathbf{D}) + \mu \nabla^2 \mathbf{D} \quad (23)$$

Where: \mathbf{D} is the displacement vector; λ and μ are Lamé's constants; and ρ is the mass density. The equation above can be solved when writing both scalar potential Φ_S and vector potential $\mathbf{A} = (r\psi_V, 0, 0)$ in spherical coordinates. So, we can obtain the spheroidal and torsional modes, before mentioned by expressing the displacement vector \mathbf{D} as

$$\mathbf{D} = \nabla \Phi_S + \nabla \times \nabla \times \mathbf{A}. \quad (24)$$

Two boundary conditions are considered: "free" ones, meaning that there is no force on the particle surface, and "rigid" ones, meaning that there is no displacement of the particle. For each case, for non-torsional solutions, the equations are given below.

In the case of "free" boundary conditions, its eigenvalue is given by:

1) for $l \geq 0$:

$$2 \left[\eta^2 + (l-1)(l+2) \left(\frac{\eta j_{l+1}(\eta)}{j_l(\eta)} - (l+1) \right) \right] \frac{\xi j_{l+1}(\xi)}{j_l(\xi)} - \frac{\eta^4}{2} + (l-1)(2l+1)\eta^2 + [\eta^2 - 2l(l-1)(l+2)] \frac{\eta j_{l+1}(\eta)}{j_l(\eta)} = 0 \quad (25)$$

A.2. Lamb's explanation for the origin of low-frequency vibrations

2) for $l = 0$, to

$$\frac{\tan \xi}{\xi} = \frac{1}{1 - \eta^2/4} \quad (26)$$

where $\eta = \omega d/v_t$ and $\xi = \omega d/v_l = \eta v_t/v_l$, are dimensionless eigenvalues, and the spherical Bessel function of the first kind is written by $j_l(\eta) = \sqrt{\pi/2\eta} J_{l+1/2}(\eta)$. The angular frequency ω is characterized by the angular momentum quantum number l , and d is the diameter of the nanocrystal. The spheroidal mode is derived from the scalar and vector potential and its eigenvalues depends on the material through the ratio v_l/v_t , where v_l and v_t are the longitudinal and transversal sound velocities, respectively. Contrarily to the first one, the torsional mode is a vibration without dilatation and does not depend on the material because it is derived only from the vector potential.

Saviot *et al.*²¹⁶ considered the “rigid” boundary conditions when the particles were embedded in a matrix. For the spheroidal mode, here are the solutions reported:

$$1) \text{ for } l = 0: \quad \tan \xi = \xi \quad , \quad (27)$$

and

$$2) \text{ for } l \geq 1: \quad \xi j_l'(\xi)[\eta j_l'(\eta) + j_l(\eta)] - l(l+1)j_l(\xi)j_l(\eta) = 0 \quad (28)$$

Tanaka *et al.*²¹⁷ described that, for even l , only the spheroidal modes are Raman-active. The energy associated with these modes is only a few cm^{-1} and its effects can be measured in the low-frequency region. So, approaching our nanoparticles to Lamb's conditions and using the average sound velocity of SnO_2 bulk,¹⁷² $v_l = 6.53 \times 10^5 \text{ cm.s}^{-1}$ and $v_t = 3.12 \times 10^5 \text{ cm.s}^{-1}$ on the previous equations, it enables us to estimate the frequencies of the Raman lines according to

$$\omega = S_l v_l / L_C \quad \text{for } l = 0 \quad (29)$$

and

A.2. Lamb's explanation for the origin of low-frequency vibrations

$$S_t v_t / Lc \quad \text{for } l = 2, \quad (30)$$

where c is the vacuum light velocity.²¹⁸ For the stress-free, the values obtained for S_l and S_t were 0.887 and 0.844, respectively; and for the rigid boundary conditions $S_l=1.430$ and $S_t=1.987$.¹¹⁹

A.3. Published works

- 1) Pressure-Induced Sublattice Disordering in SnO₂: Invasive Selective Percolation. – Girão, H. T. *et al.* – *Physical Review Letters* **120**, 265702 (2018) – DOI: 10.1103/PhysRevLett.120.265702

- 2) Pressure-Induced Disordering in SnO₂ Nanoparticles. – Girão, H. T. *et al.* – *Journal of Physical Chemistry C* **121**, 15463–15471 (2017). – DOI: 10.1021/acs.jpcc.7b04079

Bibliography

1. Lowther, J. E. Superhard Ceramic Oxides. *MRS Bull.* **28**, 189–193 (2003).
2. Yu, X., Marks, T. J. & Facchetti, A. Metal oxides for optoelectronic applications. *Nat. Mater.* **15**, 383 (2016).
3. Mammone, J. F., Nicol, M. & Sharma, S. K. Raman spectra of TiO₂-II, TiO₂-III, SnO₂, and GeO₂ at high pressure. *J. Phys. Chem. Solids* **42**, 379–384 (1981).
4. Hemley, R. J., Jephcoat, A. P., Mao, H. K., Ming, L. C. & Manghnani, M. H. Pressure-induced amorphization of crystalline silica. *Nature* **334**, 52 (1988).
5. Haines, J. & Léger, J. M. X-ray diffraction study of TiO₂ up to 49 GPa. *Phys. B Condens. Matter* **192**, 233–237 (1993).
6. Prakapenka, V. B. *et al.* α -PbO₂-type high-pressure polymorph of GeO₂. *Phys. Rev. B* **67**, 132101 (2003).
7. Prakapenka, V. ., Shen, G., Dubrovinsky, L. ., Rivers, M. . & Sutton, S. . High pressure induced phase transformation of SiO₂ and GeO₂: difference and similarity. *J. Phys. Chem. Solids* **65**, 1537–1545 (2004).
8. Haines, J., Leger, J. M. & Schulte, O. Pa₃ modified fluorite-type structures in metal dioxides at high pressure. *Science* **271**, 629 (1996).
9. Haines, J. & Léger, J. M. X-ray diffraction study of the phase transitions and structural evolution of tin dioxide at high pressure: Relationships between structure types and implications for other rutile-type dioxides. *Phys. Rev. B* **55**, 11144–11154 (1997).
10. Hellwig, H., Goncharov, A. F., Gregoryanz, E., Mao, H. & Hemley, R. J. Brillouin and Raman spectroscopy of the ferroelastic rutile-to-CaC₂ transition in SnO₂ at high pressure. *Phys. Rev. B* **67**, 174110 (2003).
11. Diéguez, A. *et al.* Morphological analysis of nanocrystalline SnO₂ for gas sensor applications. *Sens. Actuators B Chem.* **31**, 1–8 (1996).
12. Ansari, S. G. *et al.* Grain size effects on H₂ gas sensitivity of thick film resistor using SnO₂ nanoparticles. *Thin Solid Films* **295**, 271–276 (1997).
13. Li, B. *et al.* Zn₂SnO₄–SnO₂ heterojunction nanocomposites for dye-sensitized solar cells. *J. Alloys Compd.* **509**, 2186–2191 (2011).
14. Piot, L. Influence de l'énergie d'interface sur les transitions de phase sous pression: étude de nanoparticules d'oxydes fonctionnels. (Université Claude Bernard, 2013).
15. San-Miguel, A. Nanomaterials under high-pressure. *Chem. Soc. Rev.* **35**, 876 (2006).

16. Otto, D. P. & de Villiers, M. M. Why is the nanoscale special (or not)? Fundamental properties and how it relates to the design of nano-enabled drug delivery systems. *Nanotechnol. Rev.* **2**, (2013).
17. Zaera, F. Nanostructured materials for applications in heterogeneous catalysis. *Chem Soc Rev* **42**, 2746–2762 (2013).
18. Monty, C. Défauts ponctuels dans les oxydes : non-stoechiométrie et transport de matière. *J. Phys. Colloq.* **39**, C2-74-C2-85 (1978).
19. Shieh, S. R., Kubo, A., Duffy, T. S., Prakapenka, V. B. & Shen, G. High-pressure phases in SnO₂ to 117 GPa. *Phys. Rev. B* **73**, 014105 (2006).
20. Gupta, S. D., Gupta, S. K., Jha, P. K. & Ovsyuk, N. N. A first principles lattice dynamics and Raman spectra of the ferroelastic rutile to CaCl₂ phase transition in SnO₂ at high pressure: Ferroelastic rutile to CaCl₂ phase transition. *J. Raman Spectrosc.* **44**, 926–933 (2013).
21. Grinblat, F. *et al.* Compressibility and structural behavior of pure and Fe-doped SnO₂ nanocrystals. *Solid State Sci.* **64**, 91–98 (2017).
22. Roduner, E. Size matters: why nanomaterials are different. *Chem. Soc. Rev.* **35**, 583 (2006).
23. Piot, L., Le Floch, S., Cornier, T., Daniele, S. & Machon, D. Amorphization in Nanoparticles. *J. Phys. Chem. C* **117**, 11133–11140 (2013).
24. Tolbert, S. H. & Alivisatos, A. P. Size dependence of the solid-solid phase transition in CdSe nanocrystals. *Z. Für Phys. At. Mol. Clust.* **26**, 56–58 (1993).
25. Tolbert, S. & Alivisatos, A. Size Dependence of a First-Order Solid-Solid Phase-Transition - the Wurtzite to Rock-Salt Transformation in Cdse Nanocrystals. *Science* **265**, 373–376 (1994).
26. Tolbert, S. H., Herhold, A. B., Brus, L. E. & Alivisatos, A. P. Pressure-Induced Structural Transformations in Si Nanocrystals: Surface and Shape Effects. *Phys. Rev. Lett.* **76**, 4384–4387 (1996).
27. Tolbert, S. H. & Alivisatos, A. P. Se EXAFS Study of the Elevated Wurtzite to Rock Salt Structural Phase Transition in CdSe Nanocrystals. in *Nanophase Materials* (eds. Hadjipanayis, G. C. & Siegel, R. W.) 471–482 (Springer Netherlands, 1994). doi:10.1007/978-94-011-1076-1
28. Sarah H. Tolbert & Alivisatos, and A. P. High-Pressure Structural Transformations in Semiconductor Nanocrystals. *Annu. Rev. Phys. Chem.* **46**, 595–626 (1995).
29. Alivisatos, A. P., Harris, T. D., Brus, L. E. & Jayaraman, A. Resonance Raman scattering and optical absorption studies of CdSe microclusters at high pressure. *J. Chem. Phys.* **89**, 5979–5982 (1988).

30. Yang, C. C. & Mai, Y.-W. Thermodynamics at the nanoscale: A new approach to the investigation of unique physicochemical properties of nanomaterials. *Mater. Sci. Eng. R Rep.* **79**, 1–40 (2014).
31. Machon, D. *et al.* Thermodynamics of Nanoparticles: Experimental Protocol Based on a Comprehensive Ginzburg-Landau Interpretation. *Nano Lett.* **14**, 269–276 (2014).
32. Machon, D. *et al.* Interface Energy Impact on Phase Transitions: The Case of TiO₂ Nanoparticles. *J. Phys. Chem. C* **115**, 22286–22291 (2011).
33. Machon, D. & Mélinon, P. Size-dependent pressure-induced amorphization: a thermodynamic panorama. *Phys Chem Chem Phys* **17**, 903–910 (2015).
34. Machon, D., Pinheiro, C. B., Bouvier, P., Dmitriev, V. P. & Crichton, W. A. Absence of pressure-induced amorphization in LiKSO₄. *J. Phys. Condens. Matter* **22**, 315401 (2010).
35. Barnard, A. S. & Curtiss, L. A. Prediction of TiO₂ Nanoparticle Phase and Shape Transitions Controlled by Surface Chemistry. *Nano Lett.* **5**, 1261–1266 (2005).
36. Chen, X. & Mao, S. S. Titanium Dioxide Nanomaterials: Synthesis, Properties, Modifications, and Applications. *Chem. Rev.* **107**, 2891–2959 (2007).
37. Machon, D. *et al.* Thermodynamics of Nanoparticles: Experimental Protocol Based on a Comprehensive Ginzburg-Landau Interpretation. *Nano Lett.* **14**, 269–276 (2014).
38. Li, Q.-J. & Liu, B.-B. High pressure structural phase transitions of TiO₂ nanomaterials. *Chin. Phys. B* **25**, 076107 (2016).
39. Carenco, S., Portehault, D., Boissière, C., Mézailles, N. & Sanchez, C. Exploring Nanoscaled Matter from Speciation to Phase Diagrams: Metal Phosphide Nanoparticles as a Case of Study. *Adv. Mater.* **26**, 371–390 (2014).
40. Ristić, M., Ivanda, M., Popović, S. & Musić, S. Dependence of nanocrystalline SnO₂ particle size on synthesis route. *J. Non-Cryst. Solids* **303**, 270–280 (2002).
41. Sarmah, S. & Kumar, A. Optical properties of SnO₂ nanoparticles. *Indian J. Phys.* **84**, 1211–1221 (2010).
42. Brinker, C. J. & Scherer, G. W. *Sol-Gel Science: The Physics and Chemistry of Sol-Gel Processing*. (Academic Press, 2013).
43. Brinker, C. J. *et al.* Sol–gel derived ceramic films — fundamentals and applications. in *Metallurgical and Ceramic Protective Coatings* (ed. Stern, K. H.) 112–151 (Springer Netherlands, 1996). doi:10.1007/978-94-009-1501-5_6
44. Process for making chemically bonded sol-gel ceramics.
45. Olding, T., Sayer, M. & Barrow, D. Ceramic sol–gel composite coatings for electrical insulation. *Thin Solid Films* **398–399**, 581–586 (2001).

-
46. *Handbook of gas sensor materials: properties, advantages and shortcomings for applications. Vol. 2: New trends and technologies.* (Springer, 2014).
47. 12.4: Defects in Crystals. *Chemistry LibreTexts* (2013). Available at: [https://chem.libretexts.org/Textbook_Maps/General_Chemistry/Map%3A_Chemistry_\(Averill_and_Eldredge\)/12%3A_Solids/12.4%3A_Defects_in_Crystals](https://chem.libretexts.org/Textbook_Maps/General_Chemistry/Map%3A_Chemistry_(Averill_and_Eldredge)/12%3A_Solids/12.4%3A_Defects_in_Crystals). (Accessed: 17th December 2018)
48. Kofstad, P. & Norby, T. *Defects and Transport in Crystalline Solids.* (2010).
49. Gu, F. *et al.* Luminescent characteristics of Eu³⁺ in SnO₂ nanoparticles. *Opt. Mater.* **25**, 59–64 (2004).
50. Nakano, Y., Morikawa, T., Ohwaki, T. & Taga, Y. Band-gap narrowing of TiO₂ films induced by N-doping. *Phys. B Condens. Matter* **376–377**, 823–826 (2006).
51. San, H., Li, B., Feng, B., He, Y. & Chen, C. Point-defects-induced band edge displacements and band-gap narrowing in CdIn₂O₄ thin films. *Thin Solid Films* **483**, 245–250 (2005).
52. Kamble, V. B. & Umarji, A. M. Defect induced optical bandgap narrowing in undoped SnO₂ nanocrystals. *AIP Adv.* **3**, 082120 (2013).
53. J.W Morris, J. Chapter 4 - Defects in Crystals. in *A Survey of Materials Science* 135 (2007).
54. Laulhé, C. Chapitre IV - Défauts dans les Cristaux. in *L3 Physique et Applications - Structure de la Matière*
55. Kılıç, Ç. & Zunger, A. Origins of Coexistence of Conductivity and Transparency in SnO₂. *Phys. Rev. Lett.* **88**, (2002).
56. Ingram, B. J., Gonzalez, G. B., Kammler, D. R., Bertoni, M. I. & Mason, T. O. Chemical and Structural Factors Governing Transparent Conductivity in Oxides. *J. Electroceramics* **13**, 167–175 (2004).
57. Godinho, K. G., Walsh, A. & Watson, G. W. Energetic and Electronic Structure Analysis of Intrinsic Defects in SnO₂. *J. Phys. Chem. C* **113**, 439–448 (2009).
58. Schottky Defect - Point Defect in Ionic Crystal - Materials Science. *Minaprem.com*
59. Tolédano, J.-C. *Bases physiques de la plasticité des solides.* (Éditions de l'École polytechnique, 2007).
60. Martin, J.-L. *Dislocations et plasticité des cristaux.* (Presses polytechniques et universitaires romandes, 2000).
61. Callister, W. D. & Rethwisch, D. G. *Materials science and engineering: an introduction.* (John Wiley & Sons, 2010).
62. Ashcroft, N. W. & Mermin, N. D. *Solid state physics.* (Holt, Rinehart and Winston, 1976).

-
63. Atkins, P. W. *Shriver & Atkins' inorganic chemistry*. (W.H. Freeman and Co., 2010).
64. Kofstad, P. Defects and transport properties of metal oxides. *Oxid. Met.* **44**, 3–27 (1995).
65. Madou, M. J. & Morrison, S. R. *Chemical Sensing with Solid State Devices*. (Elsevier Science, 1989).
66. Betsch, R. J., Park, H. L. & White, W. B. Raman spectra of stoichiometric and defect rutile. *Mater. Res. Bull.* **26**, 613–622 (1991).
67. Kar, A., Kundu, S. & Patra, A. Surface Defect-Related Luminescence Properties of SnO₂ Nanorods and Nanoparticles. *J. Phys. Chem. C* **115**, 118–124 (2011).
68. Carbon phase diagram. *Wikimedia Commons*
69. Piermarini, G. J., Block, S., Barnett, J. D. & Forman, R. A. Calibration of the pressure dependence of the R1 ruby fluorescence line to 195 kbar. *J. Appl. Phys.* **46**, 2774–2780 (1975).
70. Gillet, P. La cellule à enclumes de diamant — Planet-Terre. *Planet Terre - ENS Lyon* (2004). Available at: <http://planet-terre.ens-lyon.fr/article/cellule-diamant.xml>. (Accessed: 12th December 2016)
71. Le choix du milieu transmetteur de pression. Available at: http://conditions-extremes.geologie-lyon.fr/index.php?option=com_content&view=article&id=25:le-choix-du-milieu-transmetteur-de-pression&catid=13&Itemid=111. (Accessed: 8th April 2018)
72. Klotz, S., Chervin, J.-C., Munsch, P. & Le Marchand, G. Hydrostatic limits of 11 pressure transmitting media. *J. Phys. Appl. Phys.* **42**, 075413 (2009).
73. Angel, R. J., Bujak, M., Zhao, J., Gatta, G. D. & Jacobsen, S. D. Effective hydrostatic limits of pressure media for high-pressure crystallographic studies. *J. Appl. Crystallogr.* **40**, 26–32 (2007).
74. Eremec, M. I. *High pressure experimental methods*. (Oxford Univ. Press, 1996).
75. Jamieson, J. C. The phase behavior of simple compounds. *Phys. Earth Planet. Inter.* **3**, 201–203 (1970).
76. Azároff, L. V. *Elements of x-ray crystallography*. (McGraw-Hill Book Company, Inc., 1968).
77. Balima, F. Structure et porosité de systèmes lamellaires sous haute pression: cas du graphite et de la vermiculite. (École Doctorale des Matériaux, 2012).
78. Okuno, E. & Yoshimura, E. M. *Física das radiações*. (Oficina de Textos, 2010).
79. Vainshtein, B. K., Feigl, E. & Spink, J. A. *Structure Analysis by Electron Diffraction*. (Elsevier Science, 2013).

-
80. Palosz, B. *et al.* High pressure x-ray diffraction studies on nanocrystalline materials. *J. Phys. Condens. Matter* **16**, S353 (2004).
81. Apostila sobre Difractometria de Raios-X (DRX). *E-disciplinas USP* Available at: <https://edisciplinas.usp.br/mod/resource/view.php?id=1384233>. (Accessed: 19th April 2018)
82. Johnson, S. Advantages & Disadvantages of XRD and XRF. *Sciencing* (2018). Available at: <https://sciencing.com/advantages-disadvantages-xrd-xrf-6054766.html>. (Accessed: 19th April 2018)
83. *Handbook of vibrational spectroscopy*. (J. Wiley, 2002).
84. Workman, J. & Springsteen, A. W. *Applied spectroscopy: a compact reference for practitioners*. (Academic Press, 1998).
85. Spectroscopy. *Wikipedia* (2018).
86. Raman, C. V. & Krishnan, K. S. A New Type of Secondary Radiation. *Nature* **121**, 501–502 (1928).
87. de Giovanni, A. & Galzerani, J. C. Espectroscopias de infravermelho, Raman e de fotoluminescência: potencialidades e complementaridades. *Rev. Bras. Ensino Fis.* **34**, 4309 (2012).
88. Chalus, P., Roggo, Y. & Ulmschneider, M. La spectroscopie Raman: un outil pour répondre à l'initiative 'Process Analytical Technology' (PAT) dans l'industrie. *Spectra Anal.* **17** (2006).
89. What is Raman Spectroscopy? | Nanophoton. Available at: <https://www.nanophoton.net/raman/raman-spectroscopy.html>. (Accessed: 22nd February 2018)
90. Piermarini, G. J., Block, S. & Barnett, J. D. Hydrostatic limits in liquids and solids to 100 kbar. *J. Appl. Phys.* **44**, 5377–5382 (1973).
91. Asaumi, K. & Ruoff, A. L. Nature of the state of stress produced by xenon and some alkali iodides when used as pressure media. *Phys. Rev. B* **33**, 5633–5636 (1986).
92. Shuker, R. & Gammon, R. W. Raman-Scattering Selection-Rule Breaking and the Density of States in Amorphous Materials. *Phys. Rev. Lett.* **25**, 222–225 (1970).
93. Ultra Low Frequency Raman Module - HORIBA. Available at: https://www.horiba.com/en_en/products/detail/action/show/Product/ultra-low-frequency-raman-module-1642/. (Accessed: 26th November 2018)
94. Panczer, G. Centre Commun de Microspectrométrie Optique. *Centre CECOMO - Commun de Microspectrométrie Optique* Available at: www.cecomo.univ-lyon1.fr. (Accessed: 28th November 2016)
95. Tzontonel. Advantages and disadvantages of Raman Spectroscopy. *Romanian Database of Raman Spectroscopy* (2017).

-
96. Raman spectroscopy. *UKEssays* (2015). Available at: <https://www.ukessays.com/essays/sciences/raman-spectroscopy.php>. (Accessed: 26th February 2018)
97. Eberhardt, K., Stiebing, C., Matthäus, C., Schmitt, M. & Popp, J. Advantages and limitations of Raman spectroscopy for molecular diagnostics: an update. *Expert Rev. Mol. Diagn.* 1–15 (2015). doi:10.1586/14737159.2015.1036744
98. Photoluminescence (PL) - HORIBA. Available at: <http://www.horiba.com/scientific/products/photoluminescence/>. (Accessed: 15th March 2018)
99. Photoluminescence. *Wikipedia* (2018).
100. Structural and photoluminescence properties of SnO₂ obtained by thermal oxidation of evaporated Sn thin films. *Curr. Appl. Phys.* **13**, 1971–1974 (2013).
101. Gilliland, G. D. Photoluminescence spectroscopy of crystalline semiconductors. *Mater. Sci. Eng. R Rep.* **18**, 99–399 (1997).
102. Bonu, V. *et al.* Influence of in-plane and bridging oxygen vacancies of SnO₂ nanostructures on CH₄ sensing at low operating temperatures. *Appl. Phys. Lett.* **105**, 243102 (2014).
103. Bonu, V., Das, A., Amirthapandian, S., Dhara, S. & Tyagi, A. K. Photoluminescence of oxygen vacancies and hydroxyl group surface functionalized SnO₂ nanoparticles. *Phys. Chem. Chem. Phys.* **17**, 9794–9801 (2015).
104. Summitt, R., Marley, J. A. & Borrelli, N. F. The ultraviolet absorption edge of stannic oxide (SnO₂). *J. Phys. Chem. Solids* **25**, 1465–1469 (1964).
105. Kohl, D. The role of noble metals in the chemistry of solid-state gas sensors. *Sens. Actuators B Chem.* **1**, 158–165 (1990).
106. Ohgaki, T. *et al.* Synthesizing SnO₂ thin films and characterizing sensing performances. *Sens. Actuators B Chem.* **150**, 99–104 (2010).
107. Matsui, T. *et al.* Electrochemical oxidation of CO over tin oxide supported platinum catalysts. *J. Power Sources* **155**, 152–156 (2006).
108. Olivi, P., Pereira, E. C., Longo, E., Varella, J. A. & Bulhões, L. O. de S. Preparation and Characterization of a Dip-Coated SnO₂ Film for Transparent Electrodes for Transmissive Electrochromic Devices. *J. Electrochem. Soc.* **140**, L81–L82 (1993).
109. Lian, P. *et al.* High reversible capacity of SnO₂/graphene nanocomposite as an anode material for lithium-ion batteries. *Electrochimica Acta* **56**, 4532–4539 (2011).
110. Katiyar, R. S., Dawson, P., Hargreave, M. M. & Wilkinson, G. R. Dynamics of the rutile structure. III. Lattice dynamics, infrared and Raman spectra of SnO₂. *J. Phys. C Solid State Phys.* **4**, 2421 (1971).
111. Jarzebski, Z. M. & Marton, J. P. Physical Properties of SnO₂ Materials I . Preparation and Defect Structure. *J. Electrochem. Soc.* **123**, 199C-205C (1976).

112. Traylor, J. G., Smith, H. G., Nicklow, R. M. & Wilkinson, M. K. Lattice Dynamics of Rutile. *Phys. Rev. B* **3**, 3457–3472 (1971).
113. Baur, W. H. Über die Verfeinerung der Kristallstrukturbestimmung einiger Vertreter des Rutiltyps: TiO₂, SnO₂, GeO₂ und MgF₂. *Acta Crystallogr.* **9**, 515–520 (1956).
114. Katiyar, R. S. Dynamics of the rutile structure. I. Space group representations and the normal mode analysis. *J. Phys. C Solid State Phys.* **3**, 1087 (1970).
115. Peercy, P. S. & Morosin, B. Pressure and Temperature Dependences of the Raman-Active Phonons in SnO₂. *Phys. Rev. B* **7**, 2779–2786 (1973).
116. Diéguez, A., Romano-Rodríguez, A., Vilà, A. & Morante, J. R. The complete Raman spectrum of nanometric SnO₂ particles. *J. Appl. Phys.* **90**, 1550–1557 (2001).
117. Beattie, I. R. & Gilson, T. R. Single Crystal Laser Raman Spectroscopy. *Proc. R. Soc. Math. Phys. Eng. Sci.* **307**, 407–429 (1968).
118. Zuo, J. *et al.* Study of the Raman spectrum of nanometer SnO₂. *J. Appl. Phys.* **75**, 1835–1836 (1994).
119. Diéguez, A., Romano-Rodríguez, A., Vilà, A. & Morante, J. R. The complete Raman spectrum of nanometric SnO₂ particles. *J. Appl. Phys.* **90**, 1550–1557 (2001).
120. Yu, K. N., Xiong, Y., Liu, Y. & Xiong, C. Microstructural change of nano- SnO₂ grain assemblages with the annealing temperature. *Phys. Rev. B* **55**, 2666–2671 (1997).
121. Haines, J. & Léger, J. M. X-ray diffraction study of the phase transitions and structural evolution of tin dioxide at high pressure: Relationships between structure types and implications for other rutile-type dioxides. *Phys. Rev. B* **55**, 11144–11154 (1997).
122. Hellwig, H., Goncharov, A. F., Gregoryanz, E., Mao, H. & Hemley, R. J. Brillouin and Raman spectroscopy of the ferroelastic rutile-to-CaC₂ transition in SnO₂ at high pressure. *Phys. Rev. B* **67**, 174110 (2003).
123. Shieh, S. R., Kubo, A., Duffy, T. S., Prakapenka, V. B. & Shen, G. High-pressure phases in SnO₂ to 117 GPa. *Phys. Rev. B* **73**, 14105 (2006).
124. Gracia, L., Beltrán, A. & Andrés, J. Characterization of the High-Pressure Structures and Phase Transformations in SnO₂. A Density Functional Theory Study. *J. Phys. Chem. B* **111**, 6479–6485 (2007).
125. Liu, L.-G. A Fluorite Isotype of SnO₂ and a New Modification of TiO₂: Implications for the Earth's Lower Mantle. *Science* **199**, 422–425 (1978).
126. Endo, S. *et al.* X-ray study of SnO₂ under high pressure and temperature generated with sintered diamond anvils. *High Press. Res.* **4**, 408–410 (1990).
127. He, Y. *et al.* High-pressure behavior of SnO₂ nanocrystals. *Phys. Rev. B* **72**, 212102 (2005).

128. Wang, Q. *et al.* Pressure transmitting medium-dependent structure stability of nanoanatase TiO₂ under high pressure. *High Press. Res.* **34**, 259–265 (2014).
129. Gupta, S. D., Gupta, S. K., Jha, P. K. & Ovsyuk, N. N. A first principles lattice dynamics and Raman spectra of the ferroelastic rutile to CaCl₂ phase transition in SnO₂ at high pressure: Ferroelastic rutile to CaCl₂ phase transition. *J. Raman Spectrosc.* **44**, 926–933 (2013).
130. Galazka, Z. *et al.* Growth, characterization, and properties of bulk SnO₂ single crystals. *Phys. Status Solidi A* **211**, 66–73 (2014).
131. Razeghizadeh, A. R., Zalaghi, L., Kazeminezhad, I. & Rafee, V. Growth and Optical Properties Investigation of Pure and Al-doped SnO₂ Nanostructures by Sol-Gel Method. *Iran. J. Chem. Chem. Eng. IJCCE* **36**, 1–8 (2017).
132. Bagheri Mohagheghi, M. M., Tabatabai Yazdi, S. & Mousavi, M. Transport, structural and optical properties of SnO₂ transparent semiconductor thin films alloyed with chromium: carrier type conversion. *J. Mater. Sci. Mater. Electron.* **28**, 13328–13335 (2017).
133. Chopra, K. L., Major, S. & Pandya, D. K. Transparent conductors—A status review. *Thin Solid Films* **102**, 1–46 (1983).
134. Feng, Y., Cui, Y.-H., Liu, J. & Logan, B. E. Factors affecting the electro-catalytic characteristics of Eu doped SnO₂/Sb electrode. *J. Hazard. Mater.* **178**, 29–34 (2010).
135. Hwang, S. H., Kim, C. & Jang, J. SnO₂ nanoparticle embedded TiO₂ nanofibers — Highly efficient photocatalyst for the degradation of rhodamine B. *Catal. Commun.* **12**, 1037–1041 (2011).
136. He, Y. *et al.* High-pressure behavior of SnO₂ nanocrystals. *Phys. Rev. B* **72**, 212102 (2005).
137. Grinblat, F. *et al.* Compressibility and structural behavior of pure and Fe-doped SnO₂ nanocrystals. *Solid State Sci.* **64**, 91–98 (2017).
138. Abello, L. *et al.* Structural Characterization of Nanocrystalline SnO₂ by X-Ray and Raman Spectroscopy. *J. Solid State Chem.* **135**, 78–85 (1998).
139. Xie, C., Zhang, L. & Mo, C. Characterization of Raman spectra in nano-SnO₂ solids. *Phys. Status Solidi A* **141**, K59–K61 (1994).
140. Zuo, J. *et al.* Study of the Raman spectrum of nanometer SnO₂. *J. Appl. Phys.* **75**, 1835–1836 (1994).
141. Jones, F. H., Dixon, R., Foord, J. S., Egdell, R. G. & Pethica, J. B. The surface structure of SnO₂(110)(4 × 1) revealed by scanning tunneling microscopy. *Surf. Sci.* **376**, 367–373 (1997).
142. Duval, E. Far-infrared and Raman vibrational transitions of a solid sphere: Selection rules. *Phys. Rev. B* **46**, 5795–5797 (1992).

143. Diéguez, A. *et al.* Nondestructive assessment of the grain size distribution of SnO₂ nanoparticles by low-frequency Raman spectroscopy. *Appl. Phys. Lett.* **71**, 1957–1959 (1997).
144. Rodríguez, J. A. & Fernández-García, M. *Synthesis, Properties, and Applications of Oxide Nanomaterials*. (John Wiley & Sons, 2007).
145. Wang, J. *et al.* Pressure-Induced Amorphization in BaF₂ Nanoparticles. *J. Phys. Chem. C* **120**, 12249–12253 (2016).
146. Curecheriu, L. *et al.* Grain Size-Dependent Properties of Dense Nanocrystalline Barium Titanate Ceramics. *J. Am. Ceram. Soc.* **95**, 3912–3921 (2012).
147. Xiao, F. *et al.* Morphology- and lattice stability-dependent performance of nanostructured Li₄Ti₅O₁₂ probed by in situ high-pressure Raman spectroscopy and synchrotron X-ray diffraction. *CrystEngComm* **18**, 736–743 (2016).
148. Kotmool, K., Bovornratanaraks, T., Chakraborty, S. & Ahuja, R. The effect of morphology and confinement on the high-pressure phase transition in ZnO nanostructure. *J. Appl. Phys.* **117**, 114309 (2015).
149. Rafiee, E., Joshaghani, M. & Ghaderi-Shekhi Abadi, P. Shape-dependent catalytic activity of Fe₃O₄ nanostructures under the influence of an external magnetic field for multicomponent reactions in aqueous media. *RSC Adv* **5**, 74091–74101 (2015).
150. Popescu, C. *et al.* Compressibility and Structural Stability of Nanocrystalline TiO₂ Anatase Synthesized from Freeze-Dried Precursors. *Inorg. Chem.* **53**, 11598–11603 (2014).
151. PAN, Y. *et al.* Pressure-Induced Structural Transitions of the Zinc Sulfide Nanoparticles with Different Sizes. *J. Mater. Sci. Technol.* **23**, (2007).
152. Jiang, J. Z. *et al.* Phase transformation and conductivity in nanocrystal PbS under pressure. *J. Appl. Phys.* **87**, 2658–2660 (2000).
153. Garg, A. B. Pressure-induced volume anomaly and structural phase transition in nanocrystalline SnO₂. *Phys. Status Solidi B* **251**, 1380–1385 (2014).
154. Jiang, J. Z., Gerward, L. & Olsen, J. S. Pressure induced phase transformation in nanocrystal SnO₂. *Scr. Mater.* **44**, 1983–1986 (2001).
155. Thangadurai, P., Bose, A. C., Ramasamy, S., Kesavamoorthy, R. & Ravindran, T. R. High Pressure effects on electrical resistivity and dielectric properties of nanocrystalline SnO₂. *J. Phys. Chem. Solids* **66**, 1621–1627 (2005).
156. Ono, S., Funakoshi, K., Nozawa, A. & Kikegawa, T. High-pressure phase transitions in SnO₂. *J. Appl. Phys.* **97**, 073523 (2005).
157. Keiji, K., Kiyoto, F. & Yasuhiko, S. Shock-induced phase transition in SnO₂, PbO₂ and FeTaO₄. *J. Phys. Chem. Solids* **52**, 845–851 (1991).

158. Casali, R. A. *et al.* Ab initio and shell model studies of structural, thermoelastic and vibrational properties of SnO₂ under pressure. *J. Phys. Condens. Matter* **25**, 135404 (2013).
159. Erdem, I., Kart, H. H. & Cagin, T. High pressure phase transitions in SnO₂ polymorphs by first-principles calculations. *J. Alloys Compd.* **587**, 638–645 (2014).
160. Girão, H. T. *et al.* Pressure-Induced Disorder in SnO₂ Nanoparticles. *J. Phys. Chem. C* **121**, 15463–15471 (2017).
161. Merle, P., Pascual, J., Camassel, J. & Mathieu, H. Uniaxial-stress dependence of the first-order Raman spectrum of rutile. I. Experiments. *Phys. Rev. B* **21**, 1617–1626 (1980).
162. Vera, R. & Jeanneau, E. Bruker D8 Advance diffractometer. *Centre de Diffractométrie Henri Longchambon* Available at: http://cdalpha.univ-lyon1.fr/img/album/d8_sheme.jpg. (Accessed: 12th December 2016)
163. Thompson, R. M. & Downs, R. T. Packing systematics of the silica polymorphs: The role played by O-O nonbonded interactions in the compression of quartz. *Am. Mineral.* **95**, 104–111 (2010).
164. Miller, D. R., Williams, R. E., Akbar, S. A., Morris, P. A. & McComb, D. W. STEM-Cathodoluminescence of SnO₂ nanowires and powders. *Sens. Actuators B Chem.* **240**, 193–203 (2017).
165. Bonu, V., Das, A., Sivadasan, A. K., K. Tyagi, A. & Dhara, S. Invoking forbidden modes in SnO₂ nanoparticles using tip enhanced Raman spectroscopy. *J. Raman Spectrosc.* **46**, (2015).
166. Jeong, J. *et al.* Photoluminescence properties of SnO₂ thin films grown by thermal CVD. *Solid State Commun.* **127**, 595–597 (2003).
167. Zhou, J. X., Zhang, M. S., Hong, J. M. & Yin, Z. Raman spectroscopic and photoluminescence study of single-crystalline SnO₂ nanowires. *Solid State Commun.* **138**, 242–246 (2006).
168. Chacko, S., Sajeeth Philip, N. & Vaidyan, V. K. Effect of substrate temperature on structural, optical and electrical properties of spray pyrolytically grown nanocrystalline SnO₂ thin films. *Phys. Status Solidi A* **204**, 3305–3315 (2007).
169. Hadia, N. M. A., Ryabtsev, S. V., Domashevskaya, E. P. & Seredin, P. V. Structure and photoluminescence properties of SnO₂ nanowires synthesized from SnO powder. *Eur. Phys. J. Appl. Phys.* **48**, 10603
170. Machon, D., Dmitriev, V. P., Sinitsyn, V. V & Lucazeau, G. Eu₂(MoO₄)₃ single crystal at high pressure: Structural phase transitions and amorphization probed by fluorescence spectroscopy. *Phys. Rev. B* **70**, (2004).
171. Otto, J. W., Vassiliou, J. K. & Frommeyer, G. Nonhydrostatic compression of elastically anisotropic polycrystals. I. Hydrostatic limits of 4:1 methanol-ethanol and paraffin oil. *Phys. Rev. B* **57**, 3253–3263 (1998).

172. Katiyar, R. S., Dawson, P., Hargreave, M. M. & Wilkinson, G. R. Dynamics of the rutile structure. III. Lattice dynamics, infrared and Raman spectra of SnO₂. *J. Phys. C Solid State Phys.* **4**, 2421 (1971).
173. Tolédano, P. & Machon, D. Structural mechanism leading to a ferroelastic glass state: Interpretation of amorphization under pressure. *Phys. Rev. B* **71**, 024210 (2005).
174. Machon, D. *et al.* Pseudoamorphization of Cs₂HgBr₄. *Phys. Rev. B* **68**, (2003).
175. Hemley, R. J. *et al.* Strain/order parameter coupling in the ferroelastic transition in dense SiO₂. *Solid State Commun.* **114**, 527–532 (2000).
176. Gonze, X. *et al.* ABINIT: First-principles approach to material and nanosystem properties. *Comput. Phys. Commun.* **180**, 2582–2615 (2009).
177. Perdew, J. P. & Wang, Y. Accurate and simple analytic representation of the electron-gas correlation energy. *Phys. Rev. B* **45**, 13244–13249 (1992).
178. Monkhorst, H. J. & Pack, J. D. Special points for Brillouin-zone integrations. *Phys. Rev. B* **13**, 5188–5192 (1976).
179. Gonze, X., Charlier, J.-C., Allan, D. C. & Teter, M. P. Interatomic force constants from first principles: The case of α -quartz. *Phys. Rev. B* **50**, 13035–13038 (1994).
180. Le Bacq, O., Machon, D., Testemale, D. & Pasturel, A. Pressure-induced amorphization mechanism in Eu₂(MoO₄)₃. *Phys. Rev. B* **83**, (2011).
181. Nguyen, J. H., Kruger, M. B. & Jeanloz, R. Evidence for “partial” (sublattice) amorphization in Co(OH)₂. *Phys. Rev. Lett.* **78**, 1936–1939 (1997).
182. Chaix-Pluchery, O., Pannetier, J., Bouillot, J. & Niepce, J. C. Structural prereactional transformations in Ca(OH)₂. *J. Solid State Chem.* **67**, 225–234 (1987).
183. Krivovichev, S. V. Structure description, interpretation and classification in mineralogical crystallography. *Crystallogr. Rev.* **23**, 2–71 (2017).
184. Machon, D. & Mélinon, P. Size-dependent pressure-induced amorphization: a thermodynamic panorama. *Phys Chem Chem Phys* **17**, 903–910 (2015).
185. Chandler, R., Koplik, J., Lerman, K. & Willemsen, J. F. Capillary displacement and percolation in porous media. *J. Fluid Mech.* **119**, 249 (1982).
186. Wilkinson, D. & Willemsen, J. F. Invasion percolation: a new form of percolation theory. *J. Phys. Math. Gen.* **16**, 3365–3376 (1983).
187. Mermin, N. D. & Wagner, H. Absence of Ferromagnetism or Antiferromagnetism in One- or Two-Dimensional Isotropic Heisenberg Models. *Phys. Rev. Lett.* **17**, 1133–1136 (1966).
188. C. Elton, D. Percolation Theory – the deep subject with the not-so-deep sounding name. (2013). Available at: <http://moreisdifferent.com/2013/11/16/percolation-theory-the-deep-subject-with-the-not-so-deep-sounding-name/>. (Accessed: 25th June 2018)

189. Porto, M., Havlin, S., Schwarzer, S. & Bunde, A. Optimal Path in Strong Disorder and Shortest Path in Invasion Percolation with Trapping. *Phys. Rev. Lett.* **79**, 4060–4062 (1997).
190. *Percolation structures and processes*. (A. Hilger; Israel Physical Society in association with The American Institute of Physics, New York, 1983).
191. When small amorphous domains appear, the fractal geometry of the high-pressure cluster (here the amorphous state) induces a power law behavior with the parameter μ given by the Hausdorff-Besicovitch space rather than the Euclidean one, and defined as $D_f = 3 - \mu$ where D_f is the Hausdorff fractal dimension of the Cantor set. For a discussion of Hausdorff Besicovitch versus fractal problem see Stewart, D.E. ANZIAM J.2001, 42, 451.
192. Quan, Z. *et al.* Pressure-Induced Switching between Amorphization and Crystallization in PbTe Nanoparticles. *Nano Lett.* **13**, 3729–3735 (2013).
193. Stauffer, D. & Aharony, A. *Introduction to percolation theory*. (Routledge, 2003).
194. Vegas, A. & Jansen, M. Structural relationships between cations and alloys; an equivalence between oxidation and pressure. *Acta Crystallogr. B* **58**, 38–51 (2002).
195. Vegas, Á. & Mattesini, M. Towards a generalized vision of oxides: disclosing the role of cations and anions in determining unit-cell dimensions. *Acta Crystallogr. B* **66**, 338–344 (2010).
196. Goutailler, G., Guillard, C., Daniele, S. & Hubert-Pfalzgraf, L. G. Low temperature and aqueous sol–gel deposit of photocatalytic active nanoparticulate TiO₂. *J. Mater. Chem.* **13**, 342–346 (2003).
197. Machon, D., Meersman, F., Wilding, M. C., Wilson, M. & McMillan, P. F. Pressure-induced amorphization and polyamorphism: Inorganic and biochemical systems. *Prog. Mater. Sci.* **61**, 216–282 (2014).
198. MET JEOL 2010F | CLYM. *CLYM - Consortium Lyon Saint-Etienne de Microscopie* Available at: <http://clym.fr/fr/node/26>. (Accessed: 13th December 2016)
199. Vera, R. & Jeanneau, E. Oxford Xcalibur Mova. *Centre de Diffractométrie Henri Longchambon* Available at: http://cdalpha.univ-lyon1.fr/img/album/CDHL_Mova.jpg.
200. Diéguez, A. *et al.* Nondestructive assessment of the grain size distribution of SnO₂ nanoparticles by low-frequency Raman spectroscopy. *Appl. Phys. Lett.* **71**, 1957–1959 (1997).
201. Mashl, R. J., Joseph, S., Aluru, N. R. & Jakobsson, E. Anomalous Immobilized Water: A New Water Phase Induced by Confinement in Nanotubes. *Nano Lett.* **3**, 589–592 (2003).
202. Birch, F. Elasticity and constitution of the Earth's interior. *J. Geophys. Res.* **57**, 227–286 (1952).
203. Saviot, L. *et al.* Quasi-Free Nanoparticle Vibrations in a Highly Compressed ZrO₂ Nanopowder. *J. Phys. Chem. C* **116**, 22043–22050 (2012).

-
204. Soler, J. M. *et al.* The SIESTA method for ab initio order-N materials simulation. *J. Phys. Condens. Matter* **14**, 2745–2779 (2002).
205. Ponce, C. A., Caravaca, M. A. & Casali, R. A. Ab Initio Studies of Structure, Electronic Properties, and Relative Stability of SnO₂ Nanoparticles as a Function of Stoichiometry, Temperature, and Oxygen Partial Pressure. *J. Phys. Chem. C* **119**, 15604–15617 (2015).
206. Parrinello, M. & Rahman, A. Crystal Structure and Pair Potentials: A Molecular-Dynamics Study. *Phys. Rev. Lett.* **45**, 1196–1199 (1980).
207. Parrinello, M. & Rahman, A. Polymorphic transitions in single crystals: A new molecular dynamics method. *J. Appl. Phys.* **52**, 7182–7190 (1981).
208. Pinna, N., Neri, G., Antonietti, M. & Niederberger, M. Nonaqueous Synthesis of Nanocrystalline Semiconducting Metal Oxides for Gas Sensing. *Angew. Chem. Int. Ed.* **43**, 4345–4349 (2004).
209. Liu, X. *et al.* High-rate amorphous SnO₂ nanomembrane anodes for Li-ion batteries with a long cycling life. *Nanoscale* **7**, 282–288 (2015).
210. Hamaya, N. *et al.* Amorphization and Molecular Dissociation of Sn I 4 at High Pressure. *Phys. Rev. Lett.* **79**, 4597–4600 (1997).
211. Girão, H. T. *et al.* Pressure-Induced Sublattice Disordering in SnO₂: Invasive Selective Percolation. *Phys. Rev. Lett.* **120**, 265702 (2018).
212. Richet, P. & Gillet, P. Pressure-induced amorphization of minerals: a review. *Eur. J. Mineral.* **9**, 907–934 (1997).
213. Machon, D., Meersman, F., Wilding, M. C., Wilson, M. & McMillan, P. F. Pressure-induced amorphization and polyamorphism: Inorganic and biochemical systems. *Prog. Mater. Sci.* **61**, 216–282 (2014).
214. Long, D. A. *Raman spectroscopy*. (McGraw-Hill, 1977).
215. Lamb, H. On the Vibrations of an Elastic Sphere. *Proc. Lond. Math. Soc.* **s1-13**, 189–212 (1881).
216. Saviot, L., Champagnon, B., Duval, E., Kudriavtsev, I. A. & Ekimov, A. I. Size dependence of acoustic and optical vibrational modes of CdSe nanocrystals in glasses. *J. Non-Cryst. Solids* **197**, 238–246 (1996).
217. Tanaka, A., Onari, S. & Arai, T. Low-frequency Raman scattering from CdS microcrystals embedded in a germanium dioxide glass matrix. *Phys. Rev. B* **47**, 1237–1243 (1993).
218. Duval, E., Boukenter, A. & Champagnon, B. Vibration Eigenmodes and Size of Microcrystallites in Glass: Observation by Very-Low-Frequency Raman Scattering. *Phys. Rev. Lett.* **56**, 2052–2055 (1986).